Cathode-Initiated Breakdown in Vacuum

A. A. Emel'yanov*, E. A. Emel'yanova, and I. O. Serikov

Orel State Technical University, Orel, Russia
* e-mail: emel@ostu.ru
Received November 24, 2003

Abstract—New methods and criteria are proposed for evaluating the cathode-initiated breakdown in vacuum. Using the optimum regimes of pulse conditioning, it is possible to significantly improve the state of the cathode surface and substantially increase the electric strength with respect to cathode initiation. The proposed methods have been experimentally verified in the range of pulse durations from 10 to 800 ns. © *2004 MAIK "Nauka/Interperiodica".*

Establishment of the technological regimes providing for high values of the electric strength requires the knowledge of mechanisms responsible for the possible impairment of this characteristic. In order to develop new methods for evaluation of the mechanisms of vacuum breakdown initiation, we have considered the process of cathode-initiated breakdown.

In a stationary regime, vacuum breakdown is initiated when the microscopic electric field strength at a cathode reaches the critical value [1]

$$E = \beta E_0 = E_{cr}, \qquad (1)$$

where β is the coefficient of electric field strength amplification on microinhomogeneities of the cathode surface and E_0 is the macroscopic field strength at the cathode. Relation (1) serves a criterion for the cathode-initiated vacuum breakdown in a stationary regime.

Any action x upon the cathode surface, accompanied by a change in the state of this surface, leads to the corresponding variation of the parameter β, which is one of the surface characteristics. Thus, the field amplification coefficient is a function of the action variable: $\beta = \beta(x)$. A change in the state of the cathode surface is manifested by changes in the electric strength and the breakdown voltage $E_0 \sim U \sim 1/\beta$. The voltage of the first breakdown after the action upon the surface is also a function of the variable x and is inversely proportional to the field amplification coefficient characterizing the state of the cathode surface: $U(x) \sim \beta^{-1}(x)$.

The efficiency of action x upon the cathode surface reflects the degree of modification of the state of this surface and can be evaluated by the relative quantity

$$K_\beta = \frac{\beta_0}{\beta_x}, \qquad (2)$$

where β_0 and β_x are the values of the field amplification coefficient before and after the given action upon the cathode surface. When $K_\beta > 1$, action x levels microinhomogeneities and increases the cathode surface qual-ity. The value $K_\beta < 1$ implies that cathode treatment leads to a growth of the surface microinhomogeneities and the surface quality is deteriorated. When $K_\beta = 1$, the action x has no influence on the cathode surface.

As was noted above, a change in the state of the cathode surface influences both the value of parameter β (characterizing the surface quality) and the voltage of the first breakdown after termination of the given action upon the cathode surface. For a cathode-initiated breakdown, the breakdown voltage is inversely proportional to the value of parameter β and, hence, the efficiency of action x upon the cathode surface and can be evaluated by another relative quantity,

$$K_U = \frac{U_x}{U_0}, \qquad (3)$$

where U_x is the voltage of the first breakdown after the termination of action x and U_0 is the established breakdown voltage before the onset of action x. When $K_U > 1$, action x levels microinhomogeneities and increases the first breakdown voltage; the value $K_U < 1$ implies that cathode treatment impairs the state of the cathode and reduces the electric strength; when $K_U = 1$, action x influences neither the cathode surface quality nor the electric strength of the insulation.

In the case of cathode-initiated breakdown, relative changes in the coefficient β and the first breakdown voltage in response to the same action x reflect the identical changes in the state of the cathode surface and, hence, are equal to each other. Therefore, criterion (1) of the cathode-initiated breakdown in a stationary regime can be alternatively presented as

$$\frac{K_\beta}{K_U} = 1. \qquad (4)$$

For $K_\beta \neq K_U$, the breakdown is initiated by a different (noncathode) mechanism.

K_β
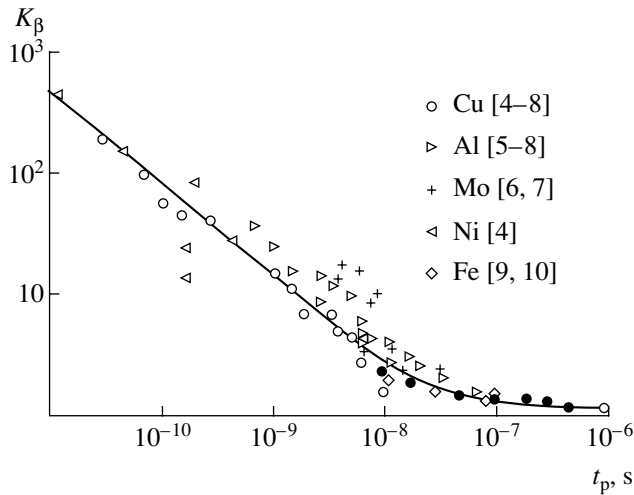
The efficiency K_β of the pulse action upon the cathode surface as a function of the optimum conditioning pulse duration $t_p \approx t_d$. Black circles represent the experimental results of this study.

In the case of small changes in the surface state and the corresponding small variations of the field amplification coefficient $\beta = \beta_0 + \Delta\beta$ ($\Delta\beta \ll \beta_0$), the mechanism of cathode-initiated breakdown implies small changes in the first breakdown voltage: $U = U_0 + \Delta U$ ($\Delta U \ll U_0$). In this case, cathode-initiated breakdown criterion (4) with neglect of the second-order terms can be expressed as

$$\frac{\Delta U}{U_0} = -\frac{\Delta\beta}{\beta_0}. \qquad (5)$$

Relation (5) is an alternative form of the criterion of cathode-initiated breakdown, which is valid for small changes in the state of the cathode surface. In this approximation, a relative decrease in the value of β ($\Delta\beta < 0$) has to be equal to a relative increase in the first breakdown voltage ($\Delta U > 0$) and vice versa: a relative decrease in the surface quality ($\Delta\beta > 0$) corresponds to a relative decrease in the electric strength ($\Delta U < 0$).

One possible method of action upon the cathode surface is based on treating the cathode with high-voltage pulses, which can eventually lead to the initiation of vacuum breakdown. For a pulse duration below 1 μs, the cathode initiation takes place when the following condition is satisfied [2]:

$$\int_0^{t_d} j^2 dt = \text{const}, \qquad (6)$$

where t_d is the breakdown delay time and j is the current density. According to this relation, breakdown initiation within the time t_d requires that the energy liberated during this period in a microemitter be equal to the energy of its destruction. Then, treatment of the cathode by pulses with the duration t_p equal to the breakdown

delay time ($t_p = t_d$) provides for the optimum regime of leveling microinhomogeneities on the cathode surface and increasing the electric strength of the insulation [3].

The efficiency of optimum regimes increases when the pulse duration is decreased with the corresponding increase in the power. The power is elevated by increasing the pulse amplitude so that the electric field strength at the cathode will obey the condition $t_p = t_d$. For subnanosecond pulses, the required field strength reaches $E_0 \sim 10^{10}$ V/m. This is achieved by reducing the gap width to a micron level [4]. Using pulse conditioning in the optimum regimes for the cathode treatment, it is possible to provide for a desired magnitude of the field amplification coefficient, up to a minimum possible value of $\beta = 1$.

For experimental determination of the delay time of vacuum breakdown, electrodes are preliminarily trained at a minimum overvoltage until obtaining a stable breakdown, which corresponds to attaining the optimum regime of pulse action upon the cathode. An analysis of experimental data on the breakdown delay time using the criterion of cathode initiation in a nonstationary regime (6) allowed relationships $\beta = f(t_p)$ between the field amplification coefficient and the high-voltage pulse duration corresponding to the optimum regime $t_p = t_d$ to be established for electrodes made of various materials [3]. Using the $\beta = f(t_p)$ curves characterizing the change in the state of the cathode surface in the course of a pulse action in the optimum regimes, one can readily evaluate the efficiency of such regimes.

By processing the available experimental data on the breakdown delay time (see figure) [4–10], we constructed the curve of $K_\beta(t_p)$ representing the efficiency of optimum regimes of the pulse action upon the cathode surface as a function of the optimum pulse duration $t_p = t_d$. As can be seen from this curve, it is expedient to treat the cathode surface by pulses with a duration of $t_p < 10^{-7}$ s. The efficiency of pulse conditioning increases with decreasing pulse duration and, at $t_p \sim 10^{-10}$ s, reaches a level more than two orders of magnitude higher than that possible with the optimum dc treatment regimes.

In the case of realization of the cathode mechanism of breakdown initiation in vacuum, the relative increase in the electric strength $K_U(t_p)$, evaluated as the first breakdown voltage in a stationary regime, as a function of the pulse duration must follow the $K_\beta(t_p)$ curve. In order to check this assumption, we measured the static breakdown voltage before and after treatment of the cathode with high-voltage pulses at $t_p = t_d$ in the range from 10 to 800 ns. The experiments were performed using vacuum capacitors with coaxial copper electrodes (diameter $d = 0.2$ mm; area $S = 2500$ mm^2; capacitance $C = 110$ pF) and vacuum gaps with stainless steel Rogovsky electrodes ($d = 0.12$ mm; $S \approx 100$ mm^2).

In the entire range studied (10 ns $\leq t_p \leq$ 800 ns), the experimental plot of $K_U(t_p)$ coincided exactly with the $K_\beta(t_p)$ curve calculated for the delay time. This result shows that criteria (4) and (6) are satisfied and confirms the validity of the mechanism of cathode-initiated breakdown in the dc regime. A pulse treatment of the cathode surface with $t_p = 10$ ns ($n = 50$) at an efficiency of $K_U = 1.8$ allowed the electric strength to be increased to $E_0 = 2.1 \times 10^8$ V/m, which is close to the limiting value achieved upon prolonged (~18 h) heating and a 1-h treatment by glow discharge in argon [11].

As can be seen from the above results, use of the pulse conditioning in the optimum regimes makes it possible to significantly improve the state of the cathode surface by decreasing the coefficient β. Under the conditions of cathode-initiated breakdown, this provides for a significant increase in the electric strength. It is expedient to use the proposed methods for studying the breakdown initiation mechanisms at limiting values of the electric strength. Such investigations determine the upper limit of applicability of the cathode mechanism at an ultimately high electric strength equal to the critical value ($E_0 = E_{cr}$) in the dc regime.

In conclusion, we have proposed new methods and criteria for evaluating the cathode-initiated breakdown in vacuum in the dc regime. Using the optimum regimes of pulse conditioning of the electrodes, it is possible to significantly improve the state of the cathode surface and reach limiting values of the electric strength of vacuum insulation. The proposed methods and criteria are recommended for evaluation of the mechanism of breakdown initiation at an ultimate electric strength in a stationary regime.

REFERENCES

1. D. Alpert, D. A. Lee, F. M. Lyman, *et al.*, J. Vac. Sci. Technol. **1**, 35 (1964).

2. A. A. Emel'yanov and G. M. Kassirov, Izv. Vyssh. Uchebn. Zaved., Fiz., No. 9, 105 (1976).

3. A. A. Emel'yanov, Prib. Tekh. Éksp., No. 5, 68 (1997).

4. B. Jüttner, W. Rohrbeck, and H. Wolff, in *Proceedings of the 9th International Conference on Phenomena in Ionized Gases (ICPIG), Bucharest, 1969*, p. 140.

5. G. M. Kassirov, Zh. Tekh. Fiz. **36**, 1883 (1966) [Sov. Phys. Tech. Phys. **11**, 1403 (1966)].

6. G. A. Mesyats, S. P. Bugaev, D. I. Proskurovskiĭ, *et al.*, Radiotekh. Élektron. (Moscow) **14**, 2222 (1969).

7. S. P. Vavilov and G. A. Mesyats, Izv. Vyssh. Uchebn. Zaved., Fiz., No. 8, 90 (1970).

8. I. I. Kalyatskiĭ, G. M. Kassirov, G. V. Smirnov, *et al.*, Zh. Tekh. Fiz. **45**, 1547 (1975) [Sov. Phys. Tech. Phys. **20**, 988 (1975)].

9. N. F. Olendzskaya and M. A. Sal'man, Zh. Tekh. Fiz. **40**, 333 (1970) [Sov. Phys. Tech. Phys. **15**, 242 (1970)].

10. I. D. Chalmers and B. D. Phukan, Vacuum **32**, 145 (1982).

11. P. N. Chistyakov, A. L. Radionovskiĭ, N. V. Tatarinova, *et al.*, Zh. Tekh. Fiz. **39**, 1075 (1969) [Sov. Phys. Tech. Phys. **14**, 807 (1969)].

Translated by P. Pozdeev

The Effect of Spatiotemporal Fluctuations on the Pulse Propagation

I. A. Khovanov and A. A. Akopov*

Saratov State University, Saratov, Russia
* e-mail: artem@chaos.ssu.runnet.ru
Received November 14, 2003

Abstract—We have studied the influence of uncorrelated Gaussian fluctuations on the propagation of pulses in an excitable medium modeled by the FitzHugh–Nagumo system under an external point action. Depending on the properties of this medium, one of the two possible scenarios is realized in the noise-induced suppression of propagating pulses. The first scenario can be classified as the noise-induced incoherence (breakage of the links) between adjacent elements of the medium. The second scenario is related to a spontaneous generation of pulses in the medium under the action of fluctuations. These models are applied to analysis of some recent biological experiments devoted to the dynamics of calcium waves. © 2004 MAIK "Nauka/Interperiodica".

As is known, active media can be characterized by a continuous energy supply from an external source and exhibit dissipation of this energy, whereby each element of the medium goes out of the state of thermal equilibrium and is capable of performing transitions to various states. Such media may feature the formation of various stationary and time-dependent spatial structures [1, 2]. These processes underlay the phenomena of self-organization in active media. Examples of such media are offered by nerve and muscle tissues, colonies of microorganisms, current-carrying magnetic superconductors, some solid state systems, etc. [2].

In this paper, we consider the process of pulse propagation through an excitable medium. When an external pulse action is applied at one end of the excitable medium, pulses propagate through this medium to the opposite end. Depending on the properties of a particular medium, the propagating pulses either retain their shape and intensity or decrease and vanish if the excitability of the medium is low [2, 3].

Mathematical modeling of the excitable media is based on the formalism of partial differential equations. Describing the behavior of macroscopic properties of the medium, these equations take into account diffusion processes involved in the interaction of elements constituting the medium. Therefore, noise effects are inherent in such mathematical models. However, sometimes, fluctuations not only arise as a result of interaction between a large number of elements of the medium but also are among the key properties of a base element. For example, this situation takes place in biological excitable media where the base element (cell) is characterized by the presence of an internal source of fluctuations related to processes in the ion channels and some other intracell processes. To study the general properties of such systems, it is necessary to introduce the sources of fluctuations into the mathematical model.

We will study the influence of uncorrelated Gaussian fluctuations on the dynamics of stationary propagating waves excited by an external pulse action. The system under consideration is a one-dimensional excitable (activator–inhibitor type) medium, whose evolution is described by the FitzHugh–Nagumo equations [4]

$$v_t = Dv_{xx} - v(v - a)(v - 1) - w,$$
$$w_t = b(v - dw) + A_x \sin 2\pi f_0 t + \xi(x, t). \tag{1}$$

Here, v and ω are variables depending on the spatial (x) and temporal (t) coordinates, characterizing the activator and inhibitor components, respectively; D, a, b, and d are the parameters determining the properties of the medium; v_{xx} is the second-order derivative of v with respect to the coordinate; v_t and w_t are the derivatives with respect to time; A_x is the amplitude of the external periodic force, which is nonzero at $x = 0$; f_0 is the frequency of the external force; and $\xi(x, t)$ is the source of a spatiotemporal white noise with intensity σ. The values of $d = 1$ and $b = 0.005$ were fixed, while the quantities a and D served as the variable (control) parameters.

We considered a distributed system of finite length l obeying boundary conditions of the second kind:

$$v_x(x, t)\big|_{x = 0; l} \equiv 0,$$

$$w_x(x, t)\big|_{x = 0; l} \equiv 0.$$

The initial state of the medium was selected randomly, and the system was allowed to evolve toward equilibrium (unexcited state), after which the external periodic action and noise were switched on. Equation (1) was numerically integrated according to an implicit scheme

using the direct and reverse trial procedures [5]. The external periodic action excited a pulse at $x = 0$, thus modeling the appearance of periodic pulses at a certain point of the medium [2, 3].

In the first stage of investigation, we considered the dynamics of system (1) in the absence of fluctuations and determined the amplitude and frequency of the external force producing a pulse in a unit element of the medium for various parameters. As a result, we determined the amplitude and frequency ensuring the generation of pulses at $x = 0$ for any values of parameters a and b; the time interval between adjacent pulses is greater than the time required for a pulse to travel through the medium.

Figure 1 introduces the plane of control parameters D versus a and shows the region of existence of nondecaying stationary propagating waves (NSPWs) induced by the point action upon the system. This region is bounded by a continuous curve (solid line *1*) from below and on the right. Outside this region, the excited pulses decayed and vanished before reaching the boundary of the medium. The pathlength of a decaying pulse depends on the proximity of parameters to the boundary of the region of existence of NSPWs. The investigation showed that the pathlength of a decaying pulse is affected by the noise, which can either increase or decrease this value (the latter is more probable).

The existence of fluctuations also influences the propagation of pulses inside the region of existence of NSPWs. It was found that, for a region in the vicinity of $a = 0.2$, fluctuations hinder the pulse propagation, which decays, not reaching the boundary $x = l$. The noise effectively decreases the diffusion coefficient (i.e., the interaction between adjacent elements of the medium), which leads to suppression of the wave front. This phenomenon can be considered as the noise-induced incoherence of the adjacent elements of the medium. This effect increases with the intensity of fluctuations. The number of pulses transmitted through the medium tends to zero as the noise intensity grows (Fig. 2, curve *1*). The growth of fluctuations also decreases the pathlength of decaying pulses. The most probable event is vanishing of the pulse in the vicinity of the source of excitation, that is, near $x = 0$.

For smaller values of a ($a < 0.12$), the fluctuations induce excitation of the medium at arbitrary points uniformly distributed along the medium. The appearance of such a random excitation source gives rise to two waves propagating in opposite directions from the source. The waves moving toward the regular source situated at $x = 0$ can annihilate with the waves outgoing from this periodic source. In this case, only waves from the random source reach the end point $x = l$ of the medium. This dynamics leads to an increase in the aver-
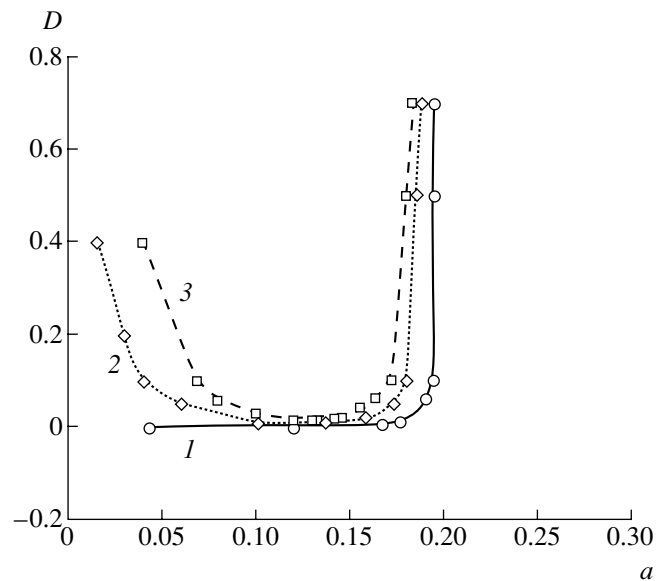

Fig. 1. The plane of control parameters showing the region of existence of nondecaying stationary propagating waves (NSPWs): outside curve *1*, excited pulses decay and vanish, not reaching the end $x = l$ of the medium; in the presence of white noise, NSPWs exist for fixed values of the noise intensity $\sigma = 5E{-}7$ (above curve *2*) and $\sigma = 1E{-}6$ (above curve *3*).
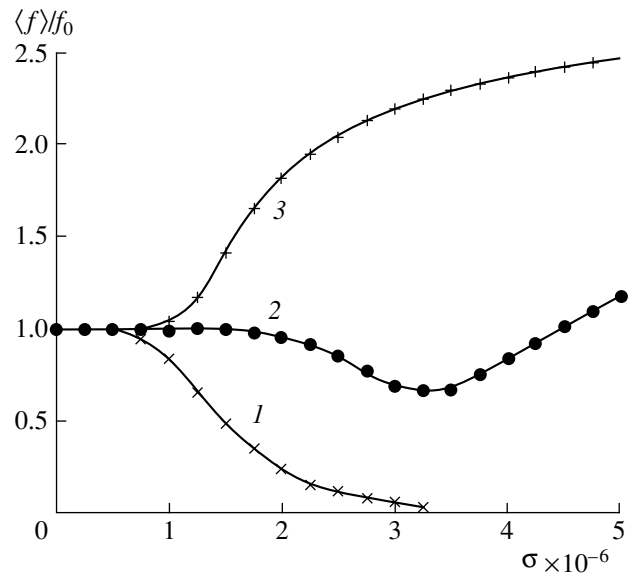

Fig. 2. Plots of the normalized average frequency of the arrival of pulses at the end point $x = l$ of the medium versus the white noise intensity σ for various values of the control parameters: (*1*) $a = 0.05$, $D = 0.1$; (*2*) $a = 0.14$, $D = 0.05$; (*3*) $a = 0.18$, $D = 0.4$.

age number of pulses coming to the point $x = l$ (Fig. 2, curve *3*); the arrival time of these pulses is random. Therefore, regular arrival of pulses to the point $x = l$ ceases and changes to a random process.

When the parameter a takes intermediate values, $a \in (0.12, 0.2)$, the system features a superposition of

the effects of pulse suppression and random source excitation (Fig. 2, curve *2*).

Thus, fluctuations break the periodic process of pulse propagation and arrival at the end point. Depending on the values of parameters, two different effects take place: (i) suppression of the propagating pulses and (ii) appearance of random excitation sources. These two effects may coexist in a certain interval of parameters.

By varying the parameters of the medium, in particular, by increasing the diffusion coefficient D at a fixed value of parameter a, it is possible to restore the regime of periodic propagation in the presence of noise. Figure 1 shows two regions in which the NSPWs do exist for fixed values of the noise intensity: $\sigma = 5E–7$ (above curve *2*) and $\sigma = 1E–6$ (above curve *3*). As can be seen, the region of existence of NSPWs exhibits contraction, which is especially pronounced in the region of small values of parameter a.

Recently, it was experimentally demonstrated [6, 7] that a change in the chemical composition of cells in an excitable medium is manifested by suppression of the excited waves and by the excitation of waves at random points of the medium. The results presented above show that these experimental data can be described within the framework of the base model of an excitable medium without recourse to cumbersome detailed equations describing cell dynamics in the medium [8]. A key mechanism is the fluctuation dynamics of individual cells, while the change in the chemical composition of a biological medium can be related to parameter a responsible for dissipation of the unit element of the medium.

Based on the results obtained, we can also formulate a strategy for suppression of the waves propagating in an excitable medium. The problem of such wave suppression is important for many applications [1, 2]. For a medium characterized by low excitability, the suppression is achieved by providing a specific additive external action. The shape and the site of application of this action can be determined by analysis of the prehistory of fluctuations breaking the propagating waves. In this case, determination of the specific control action is based on the method of determination of control forces using the analysis of the dynamics of large fluctuations [9, 10]. In a highly excitable medium, the suppression of a wave can be provided by generating an asymmetric counterwave directed only toward the propagating wave front. The possibility of generating such waves is the subject of our further research.

REFERENCES

1. Y. Kuramoto, *Chemical Oscillations Waves and Turbulence* (Springer, Berlin, 1984), p. 163.
2. M. G. Cross and P. C. Hohenberg, Rev. Mod. Phys. **65**, 851 (1993).
3. Y. Horicava, Phys. Rev. E **50**, 1708 (1994).
4. R. Fitzhugh, Biophys. J. **1**, 445 (1961).
5. A. A. Samarskiĭ and A. V. Gulin, *Numerical Methods* (Nauka, Moscow, 1989).
6. J. Marchant, N. Callamaras, and I. Parker, EMBO J. **18**, 5285 (1999).
7. I. Llano, J. Gonzlez, C. Caputo, *et al.*, Nat. Neurosci. **3**, 1256 (2000).
8. M. Falcke, Biophys. J. **84**, 42 (2003).
9. V. N. Smelyanskiy and M. I. Dykman, Phys. Rev. E **55**, 2516 (1997).
10. I. A. Khovanov, D. G. Luchinsky, R. Mannella, *et al.*, Phys. Rev. Lett. **85**, 2100 (2000).

Translated by P. Pozdeev

Photoemission from Gallium Nitride

M. R. Aĭnbund, E. G. Vil'kin, A. V. Pashuk, A. S. Petrov, and I. N. Surikov

"Electron" Central Research Institute, St. Petersburg, Russia
e-mail: eldy@mail.wplus.net
Received December 8, 2003

Abstract—We have studied the possibility of obtaining a high-response photocathode based on Mg-doped *p*-GaN layers grown by metalorganic vapor phase epitaxy. © *2004 MAIK "Nauka/Interperiodica".*

GaN and GaAlN are semiconductor materials widely used for obtaining negative-affinity photoemitters sensitive in the 0.2–0.35 and 0.2–0.3 μm wavelength intervals, respectively [1, 2].

We have studied the possibility of obtaining a high-response photocathode based on Mg-doped *p*-GaN layers grown at the Ioffe Physicotechnical Institute (St. Petersburg) by metalorganic vapor phase epitaxy (MOVPE) on (0001)-oriented sapphire substrates. The *p*-GaN layers were doped with Mg and had a hole concentration within $(1–5) \times 10^{18}$ cm^{-3}. The active GaN layer thickness was about 0.5 μm.

The photoemission from MOVPE-grown GaN layers was studied in a vacuum chamber at a residual pressure of 2×10^{-9} Torr. The samples were fixed on a tantalum substrate with two spring clamps also providing for the electric contact with the GaN layer surface. The contact resistance was on the order of 1 kΩ. Prior to measurements, the sample was cleaned by heating in vacuum at a rear side temperature of 700–900°C and then activated with cesium.

The measurements of photoemission were performed in the course of frontal illumination of the sample by an optical system using a deuterium–argon lamp (DNM-100) as a radiation source. The optical system allowed the photocathode in the vacuum chamber to be illuminated through a sapphire window by light with a wavelength above 200 nm. The absolute photosensitivity was measured at 275 ± 15 nm using a special UV interference filter ("Electron" Corporation) [3]. The calibration measurements of the radiation power at the output of the optical system and the UV filter were performed using a photodiode (KDF105A) and two photocells with Cs$_2$Te cathodes possessing known spectral characteristics.

The results of our measurements showed that an increase in the photocurrent was observed only in the samples activated with cesium. Activation with oxygen led to a decrease in the sensitivity of photocathodes. Multiply repeated cycles of heating and activation showed that the sensitivity gradually increases for the first seven cycles of treatment. The maximum spectral sensitivity $S(\lambda)$ achieved in our experiments was observed for λ =

275 nm and amounted to $S(275 \text{ nm}) = 25$ mA/W, which corresponds to a quantum yield of $Y(275 \text{ nm}) = 11\%$. This photosensitivity level is by no means the maximum possible for the GaN based photocathodes. We believe that a decrease in the residual pressure in the vacuum chamber to $10^{-10}–10^{-11}$ Torr will ensure an increase in the quantum yield up to 50% and above.

Since the edge of the absorption band of semiconductor GaN occurs approximately at λ = 350 nm, GaN photocathodes exhibit a significant decrease in sensitivity at longer wavelengths. For the investigation of sensitivity in the range of $\lambda > E_g$ (E_g is the bandgap width of the semiconductor), we used a light-emitting diode operating at λ = 591 ± 15 nm. The results of measurements using this source showed that the spectral sensitivity of our GaN photocathodes in this region is $S(591 \text{ nm}) = 1 \times 10^{-5}$ mA/W.

For comparison, the sensitivities of two photocells with Cs$_2$Te cathodes at this wavelength were $S(591 \text{ nm}) = 3 \times 10^{-6}$ and 1×10^{-4} mA/W. Apparently, the sensitivity GaN at λ = 591 nm is related to the impurity photoemission. Obtaining GaN layers with a lower content of residual impurities will probably provide for an increase in the sensitivity at 270 and 591 nm.

REFERENCES

1. J. Ma, B. Garni, N. Perkins, *et al.*, Appl. Phys. Lett. **69**, 3351 (1996).
2. C. I. Wu and A. Kahn, Appl. Surf. Sci. **250**, 162 (2000).
3. Z. M. Dvorkina, L. V. Lapushkina, I. N. Surikov, *et al.*, in *Proceedings of the 12th Scientific–Engineering Conference "The Directions of Development of Television Photoelectron Devices and Related Equipment," St. Petersburg, 2001*, pp. 195–196.

Translated by P. Pozdeev

Concentration Inhomogeneities and Phase Diagrams of Eutectic Systems

A. G. Ambrok[a],* and S. V. Nemna[b],**

[a] *Institute for Problems of Mechanical Engineering, Russian Academy of Sciences, St. Petersburg, Russia*
[b] *St. Petersburg State Technical University, St. Petersburg, Russia*
e-mail: * ambrok@ipme.ru; ** serguei_nemenat@yahoo.co.uk
Received November 18, 2003

Abstract—We show that it is possible to determine the regions of compositions with developed concentration inhomogeneities in the liquid phase by analysis of the phase diagrams of binary eutectic systems. © *2004 MAIK "Nauka/Interperiodica"*.

According to the commonly accepted physicochemical notions, a binary system at temperatures above the liquidus temperature (T_L) occurs in a homogeneous liquid state. However, the results of experimental investigations of eutectic systems [1–4] show evidence of a sharp increase in the magnitude of fluctuations in certain concentration intervals, which is manifested by anomalous behavior of some physical properties.

In order to characterize fluctuations of the concentration in a liquid system, it is convenient to use the concept of the structural factor in the long-wavelength limit as introduced by Bhatia and Thornton [5]. This structural factor is a correlator of the concentration fluctuations. This quantity is proportional to the second derivative of the thermodynamic potential with respect to concentration and, hence, determines the boundaries of the absolute thermodynamic instability of the inhomogeneous solution [5, 6]:

$$S_{XX}(0) = N\langle(\Delta X \Delta X)\rangle = \frac{RT}{\partial^2 G(X, T)/\partial X^2}, \quad (1)$$

where N is the particle number density in the system.

We consider eutectic systems for which the state of the liquid phase can be described within the framework of the theory of regular solutions (and modifications of this theory). The Gibbs energy of the solid phase is calculated as an additive value because the mutual solubility in the solid state for the system under consideration is small.

For optimization of the thermodynamic potential and reconstruction of the phase diagrams of eutectic systems, we use the following expansions of the excess thermodynamic potential with respect to the concentration and the temperature:

(i) for a regular solution,

$$G_{\text{ex}} = X(1 - X)\omega; \quad (2)$$

(ii) for a subregular solution with the temperature dependence,

$$G_{\text{ex}} = X(1 - X)[(\omega_{01} + \omega'_{01}T) + (\omega_{11} + \omega'_{11})(1 - 2X)]; \quad (3)$$

(iii) for a three-parameter model,

$$G_{\text{ex}} = X(1 - X)[(\omega_1 + \omega_2(1 - 2X)\omega_3(1 - 6X + 6X^2)]. \quad (4)$$

All these expansions are particular cases of the expansion of G_{ex} into Legendre polynomials proposed by Bale and Pelton [7, 8].

For determining the parameters in expansions (3) and (4), we used the method proposed in [9]. According to this, the thermodynamic quantities are represented in the matrix form. Then, the error equations are written and the coefficients in the expansion of the Gibbs energy with respect to the temperature and concentration are determined by solving the normal system of Gauss equations using the least squares method. The liquidus curve was calculated using the Newton–Raphson method.

The calculations were performed for Na–K, Na–Rb, and Na–Cs systems. The initial data for these calculations were taken from [10]. Figure 1 shows the results for the Na–Rb system. As can be seen, the three-parameter model provides for the best fit to experiment. Analogous behavior is observed for the Na–K and Na–Cs systems.

The boundaries of the region of absolute thermodynamic instability (spinodal) are determined from the condition that the second derivative of the thermodynamic potential is zero. For all three model systems studied, there are such regions of a characteristic dome shape under the liquidus curves (Fig. 1, curve *4*). For the Na–Rb system, the critical parameters are $T_{\text{cr}} = 327$ K and $X_{\text{cr}} = 0.72$. In experiment, the existence of such regions in melted metals is very difficult to detect. However, phase diagrams of this type are also observed for some other systems, such as protein solutions [11]
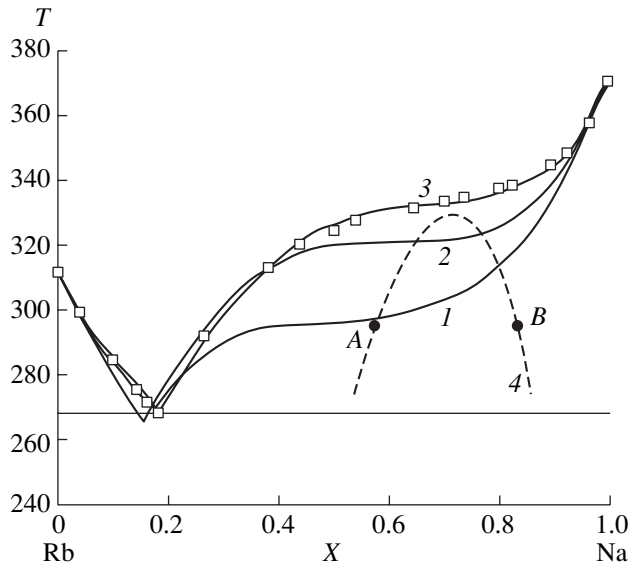
Fig. 1. Phase diagram of the Na–Rb system: (□) experiment; (1) regular solution model; (2) subregular solution with the temperature-dependent structural factor; (3) three-parameter model; (4) spinodal.
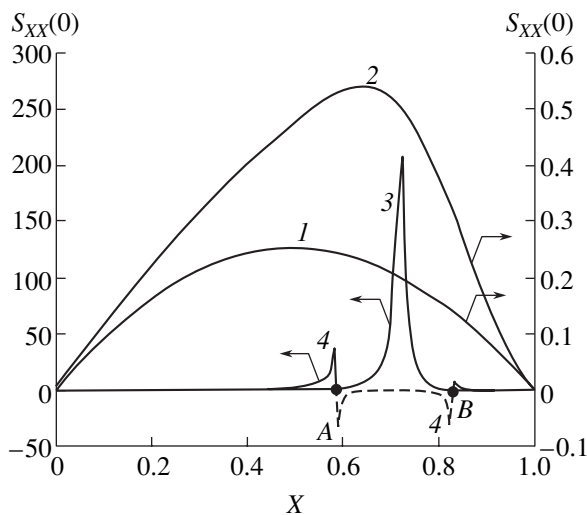

Fig. 2. Plots of $S_{XX}(0)$ versus composition of the liquid phase at various temperatures: (1) ideal solution; (2–4) $T = 550, 327$, and 296 K, respectively.

parameter model. Here, curve 1 is the temperature-independent structural factor $S_{XX}(0)$ of the ideal solution and curves 2–4 show this factor for 550 K ($T \gg T_{cr}$), 327.3 K ($T \simeq T_{cr}$), and 296 K ($T \ll T_{cr}$), respectively. At the critical points, the structural factor tends to infinity (i.e., the correlation radius of fluctuations becomes comparable with the size of the system) [15]. As the temperature increases, the structural factor drops sharply and, in the limit, tends to that of the ideal solution. At temperatures below T_{cr}, the structural factor becomes negative; this implies the absolute thermodynamic instability of a homogeneous solution, whereby the system separates into two phases (in Fig. 2, this region is indicated by the dashed line). The points where the structural factor at a given temperature is equal to zero correspond to points on the spinodal curve (in Figs. 1 and 2, these are points A and B).

Thus, we have demonstrated the possibility of obtaining information about fluctuations in the region above the liquidus line for systems with phase diagrams of the eutectic type.

REFERENCES

1. V. I. Danilov, *Crystallization and Structure of Fluids* (Naukova Dumka, Kiev, 1956).

2. H. Neumann, W. Hoger, W. Matz, *et al.*, Phys. Status Solidi A **92**, K19 (1985).

3. M.-C. Bellissent-Funel, M. Roth, and P. Desre, J. Phys. F: Met. Phys. **9**, 987 (1979).

4. Yu. S. Tver'yanovich, E. V. Kalashnikov, O. V. Il'chenko, *et al.*, Fiz. Khim. Stekla **22**, 291 (1996).

5. A. E. Bhatia and D. E. Thornton, Phys. Rev. B **2**, 3004 (1970).

6. V. M. Glazov and L. M. Pavlova, *Chemical Thermodynamics and Phase Equilibrium* (Metallurgiya, Moscow, 1988).

7. C. W. Bale and A. D. Pelton, Can. Metall. Q. **14**, 213 (1975).

8. A. D. Pelton and C. W. Bale, Metall. Trans. A **17**, 1057 (1986).

9. H. L. Lukas, E.-Th. Henig, and B. Zimmermann, CALPHAD **1**, 225 (1977).

10. P. I. Bystrov, D. N. Kagan, G. A. Krechetova, and É. É. Shpil'raĭn, *Liquid-Metal Coolants of Heat Pipes and Power Stations* (Nauka, Moscow, 1988).

11. O. Galkin and P. G. Vekilov, Proc. Natl. Acad. Sci. USA **97**, 6277 (2000).

12. N. Asherie, A. Lomakin, and G. B. Benedek, Phys. Rev. Lett. **77**, 4832 (1996).

13. M. G. Kim and S. V. Letcher, J. Chem. Phys. **55**, 1164 (1971).

14. J. E. Amaral and S. V. Letcher, J. Chem. Phys. **61**, 92 (1974).

15. A. Z. Patashinskiĭ and V. L. Pokrovskiĭ, *Fluctuation Theory of Phase Transitions*, 2nd ed. (Nauka, Moscow, 1982; Pergamon Press, Oxford, 1979).

Translated by P. Pozdeev

and colloidal solutions [12]. Indirect evidence for the existence of spinodals in Na–Cs and Na–Rb systems is offered by anomalies in the temperature and concentration dependences of the coefficient of ultrasound absorption [13, 14], where the position of maximum of this coefficient almost exactly coincides with X_{cr}.

Once the function $G''_{XX}(X, T)$ is known, the structural factor in the long-wavelength limit can be calculated using formula (1). Figure 2 shows the concentration dependence of $S_{XX}(0)$ for the Na–Rb system calculated for various temperatures using the expression for $G_{ex}(X, T)$ obtained within the framework of the three-

Effective HF(DF) Lasers
Pumped by Nonchain Chemical Reaction
Initiated by Self-Sustained Discharge

A. N. Panchenko* and V. F. Tarasenko

Institute of High-Current Electronics, Siberian Division, Russian Academy of Sciences, Tomsk, Russia
* e-mail: alexei@loi.hcei.tsc.ru
Received November 10, 2003

Abstract—We have studied the regimes of electric-discharge nonchain HF(DF) lasers using inductive and capacitive energy stores and determined optimum excitation conditions. On this basis, discharge-initiated HF and DF lasers have been created, which are characterized by a high specific energy output, high internal efficiency (~10 and ~7% of the electric input energy, respectively), and good technical efficiency (~6 and ~5% of the total stored energy, respectively). © 2004 MAIK "Nauka/Interperiodica".

Nonchain HF(DF) chemical lasers have been extensively studied in recent years [1–12]. One important task that still has to be solved is to increase the technical efficiency of the simplest and most practical HF and DF lasers pumped by self-sustained discharge, possessing a high specific output radiation power. The maximum technical efficiency (about 6%) of a discharge-initiated nonchain HF laser was obtained using a mixture of elegas with hydrogen pumped by short (20 ns) pulses from a strip line [1]. However, both specific and total output energies were relatively low: 0.7 J/l and 0.14 J, respectively. Increase in the pumping pulse duration [1] was accompanied by a rapid drop in the efficiency.

In the best discharge-initiated nonchain lasers with energy outputs exceeding 1 J, the technical efficiency was ~4% for the HF lasers [6, 8, 9, 12] and ~3% for a DF laser [8] at a specific energy of up to 7 J/l (50 J/(l bar)). Use of a more sophisticated system with an X-ray photoinitiated discharge in an SF_6–C_2H_6 mixture provided for an increase in the specific output energy up to 9 J/l at the technical efficiency of an HF laser up to 4.7% [7]. Baranov *et al.* [2] reported that a total output energy of 0.5 J (6 J/l) and an internal efficiency of up to 5% were achieved in an HF laser by adding a small amount of propane to an elegas–hydrogen mixture, the improved characteristics being provided by increased homogeneity of the electric discharge.

This study was aimed at determining optimum pumping conditions ensuring the maximum efficiency of discharge-initiated nonchain HF(DF) lasers along with high specific energy outputs.

The working gas mixtures were excited by self-sustained discharge of an inductive or capacitive *LC* oscillator with a capacitance of $C = 13$–70 nF. The gap width between 70-cm-long profiled electrodes generating a homogeneous electric field in the laser discharge was 3.8 cm. Preionization of the mixture was provided by radiation from spark gaps arranged along one of the electrodes (cathode or anode); some experiments were performed without preionization. The laser cavity was formed by a flat aluminum mirror and KRS-5 or KRS-6 crystal plates. The laser beam width at the cavity output varied within 0.4–1 cm, depending on the working mixture composition. The laser design and methods of measurements are described in detail elsewhere [12]. The parameters of discharge and lasing characteristics were studied for elegas mixtures with pentane, hydrogen, or deuterium in the range of pressures from 0.03 to 0.12 bar.

In the course of investigation, we have established the main factors influencing the stability of discharge, the energy parameters, and the efficiency of HF and DF lasers. These factors are considered below.

1. Electric field homogeneity in the laser discharge gap. This factor is especially important in the case of mixtures with hydrogen, for which the maximum laser efficiencies were obtained. For the same maximum energy of the capacitive store, replacing the profiled electrodes by those with cylindrical surfaces led to a severalfold decrease in the output energy even in the mixtures containing pentane. Under these conditions, the photographs of integral discharge emission displayed multiple spark channels. An additional criterion of the homogeneity of discharge was the character of current passage via the laser gap. In the case of a volume discharge formation in the working mixture (the regime was set by controlling the voltage on the store capacitor $C = 70$ nF), the discharge current ceased in approximately 100 ns and a rather high voltage drop across the laser gap was retained. In the case of channel formation, the discharge current increased, the voltage

drop across the gap decreased, and the discharge acquired an oscillatory character [11].

2. Preionization. The results of measurements showed that preionization provides for a 10–70% increase in the laser energy in hydrogen-containing mixtures. In the absence of preionization, the discharge was initiated in local regions and then filled the entire working surface of the electrode. At a low charging voltage, the discharge consisted of one or a few diffuse channels closed to bright cathode spots. In pentane-containing mixtures, the effect of preionization was observed only for small voltages on the store capacitor and accordingly low specific input energies (<20 J/l). When the electric input energy was increased by increasing the charging voltage on the store capacitor (as in [6, 8, 12]), the discharge remained homogeneous (even without preionization).

3. Working mixture composition and specific input energy. A comparison of the output energies observed for various gas mixtures showed that, as was pointed out previously, the maximum efficiency under optimum pumping conditions is obtained in SF_6–$H_2(D_2)$ mixtures. In cases of violated homogeneity of the electric field in the discharge gap, increased pumping pulse duration, or absent preionization, a certain gain in the output is provided by adding pentane.

Figure 1 shows a plot of the internal efficiency versus specific input energy for a HF laser with SF_6–H_2 (8 : 1) mixtures pumped from various LC oscillators. The gas pressure and charging voltage were selected so as to provide that the residual voltage on the store capacitance was close to zero. The maximum internal efficiency (9–10%) was obtained with a store capacitance of $C = 13$–39 nF at an input energy of 30–70 J/l (specific output energy, 3–7 J/l). The optimum with respect to the specific pumping energy in this region was previously observed for a laser with a 20-cm-long active region [4]. A high internal efficiency of HF(DF) lasers, amounting to ~10 (7)%, was also obtained in the case of pumping from a capacitive store with $C = 70$ nF, but at a low charging voltage. The technical efficiency in this regime did not exceed 1% because of incomplete discharge of the store capacitor. It should be noted that, similarly to [2], we also obtained an increase in the output energy for a ternary mixture of SF_6–H_2 with small pentane additives (~10%). The maximum output energy for SF_6–H_2–C_5H_{12} mixtures was $Q = 1.9$ J (~8 J/l). As was noted above, the additives of hydrocarbons provide for an increase in the stability of discharge with increasing input energy.

In the case of pumping from an inductive energy store (at an excitation pulse duration of 100 ns or below), the internal efficiency of HF lasers reached 10% at an output energy of $Q = 1.4$ J (and a specific output of up to 6.5 J/l). For a DF laser, the internal efficiency was up to 7% at $Q = 1.2$ J (and a specific output of ~5 J/l). Under these conditions, an increase in the pumping power allowed high internal efficiencies to be
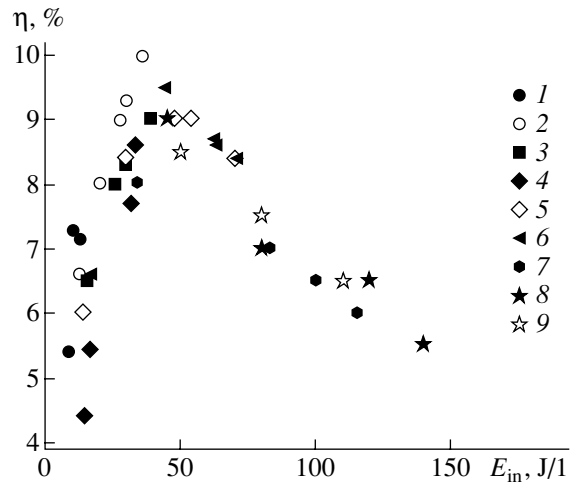

Fig. 1. A plot of the internal efficiency η versus specific input energy E_{in} for a discharge-initiated HF laser with SF_6–H_2 (8 : 1) working mixtures at various pressures p pumped from capacitive energy stores with capacitance C in the 13–70 nF range (C, p): (*1*) 13 nF, 13.5 Torr; (*2*) 13 nF, 27 Torr; (*3*) 13 nF, 40.5 Torr; (*4*) 26 nF, 27 Torr; (*5*) 26 nF, 40.5 Torr; (*6*) 39 nF, 40.5 Torr; (*7*) 70 nF, 40.5 Torr; (*8*) 70 nF, 54 Torr; (*9*) 70 nF, 67 Torr.

obtained for both low (~10 J/l) and maximum input energies (up to 50 J/l).

4. Pumping pulse duration. This parameter is known to significantly influence the working characteristics of discharge-initiated nonchain HF(DF) lasers. At a pulse duration of 100 ns and below, the maximum output energy and efficiency were obtained for the mixtures with hydrogen, while excitation pulses longer than 200 ns gave the best results in the working mixtures containing hydrocarbons. In our experiments with hydrogen-containing mixtures, an increase in the duration of discharge current pulses from 100 to 250 ns led to a twofold decrease in the output energy. In [1], a substantial decrease in the laser efficiency was observed for a pumping pulse duration above 20 ns; in wide-aperture lasers, a decrease in the stability of discharge was observed in the working mixtures with hydrocarbons [8] and deuterium [5] for pumping pulse durations above 200–300 ns.

Neither photographs of the integral discharge emission nor oscillograms of the laser discharge current and voltage showed evidence of violation of the homogeneity of discharge when the duration of pumping pulses was increased above 100 ns. It can be suggested that an increase in the duration of current pulses leads to a change in the character of discharge in SF_6 based mixtures, whereby a large number of thin channels appear in which the efficiency of atomic fluorine formation is low, but these channels are indistinguishable in the integral photographs. As is known, the production of atomic fluorine determines the parameters of nonchain chemical lasers. As is known, the formation of microchannels limits the output pulse duration in discharge-
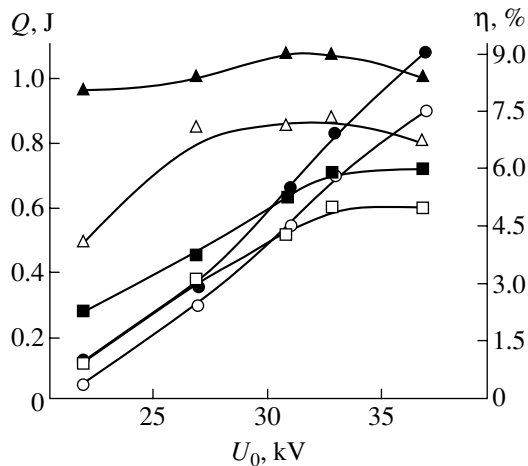
Fig. 2. Plots of the output energy Q (circles) and the technical (squares) and internal (triangles) efficiency η versus charging voltage of a capacitive energy store with $C = 26$ nF for nonchain HF (filled symbols) and DF (open symbols) lasers with SF_6–$H_2(D_2)$ (8 : 1) working mixtures at $p = 40.5$ Torr.

initiated exciplex lasers [13]. This is confirmed by the fact that the efficiency of HF lasers with electron beam pumping (which ensures a homogeneous energy input because of the absence of discharge contraction) is not decreased with increasing duration of the pumping pulses. Indeed, the same internal efficiency (~10%) was observed in electron-beam-pumped lasers using hydrogen-containing mixtures for a pumping pulse duration (FWHM) of 120 ns [3] and 300 ns [10].

The results of investigation of the optimum pumping regimes allowed us to achieve a significant increase in the internal efficiency of HF and DF lasers and improve the specific output at a high technical efficiency level. Figure 2 shows plots of the output energy and efficiency of nonchain HF and DF lasers versus the charging voltage of a capacitive energy store with $C = 26$ nF. The maximum technical efficiency was ~6 and 5%, and the maximum output energy was ~1.1 and ~0.9 J at a maximum specific output of ~6 J/l (~110 J/(l bar)) and ~5 J/l (~90 J/(l bar)) for the HF and DF lasers, respectively. For $C = 39$ nF, the output energy of the HF laser increased to 1.4 J, while the tech-

nical efficiency was retained at a level of ~6%. The output radiation spectrum of the HF(DF) lasers studied displayed 30–40 vibrational-rotational lines of HF(DF) molecules with intense cascade transitions [12].

In conclusion, we have determined the optimum parameters and pumping conditions for nonchain HF(DF) lasers, which provide for the maximum efficiency at high specific output energies. Based on these results, we have developed discharge-initiated nonchain HF and DF lasers with an output energy above 1 J, a specific output of up to 6 J/l (>100 J/(l bar)), and a technical efficiency of ~6 and ~5%, respectively.

REFERENCES

1. K. Midorikava, S. Sumida, Y. Sato, *et al.*, IEEE J. Quantum Electron. **15**, 190 (1979).
2. V. Yu. Baranov, F. I. Vysikaĭlo, A. V. Dem'yanov, *et al.*, Kvantovaya Élektron. (Moscow) **11**, 1173 (1984).
3. V. A. Abolentsev, G. L. Nedoseev, V. D. Rusanov, *et al.*, Kvantovaya Élektron. (Moscow) **16**, 218 (1989).
4. F. G. Goryunov, K. V. Gurkov, M. I. Lomaev, *et al.*, Kvantovaya Élektron. (Moscow) **21**, 1148 (1994).
5. N. Anderson, T. Bearpark, and S. J. Scott, Appl. Phys. B **63**, 565 (1996).
6. V. V. Apollonov, S. Yu. Kazantsev, V. F. Oreshkin, and K. N. Firsov, Kvantovaya Élektron. (Moscow) **25**, 123 (1998).
7. L. Richeboeuf, S. Pasquiers, F. Doussiet, *et al.*, Appl. Phys. B **68**, 45 (1999).
8. V. V. Apollonov, S. Yu. Kazantsev, V. F. Oreshkin, *et al.*, Izv. Ross. Akad. Nauk, Ser. Fiz. **64**, 1439 (2000).
9. V. P. Borisov, V. V. Burtsev, S. D. Velikanov, *et al.*, Kvantovaya Élektron. (Moscow) **30**, 225 (2000).
10. M. V. Erofeev, V. M. Orlovskiĭ, V. S. Skakun, *et al.*, Kvantovaya Élektron. (Moscow) **30**, 486 (2000).
11. V. F. Tarasenko, V. M. Orlovskiĭ, and A. N. Panchenko, Kvantovaya Élektron. (Moscow) **31**, 1035 (2001).
12. A. N. Panchenko, V. M. Orlovskiĭ, V. F. Tarasenko, and E. Kh. Baksht, Kvantovaya Élektron. (Moscow) **33**, 401 (2003).
13. M. R. Osborne and M. H. R. Hutchnson, J. Appl. Phys. **59**, 711 (1986).

Translated by P. Pozdeev

Depinning at the Initial Stage of the Resistive Transition in Superconductors with a Fractal Cluster Structure

Yu. I. Kuzmin

Ioffe Physicotechnical Institute, Russian Academy of Sciences, St. Petersburg, 194021 Russia
St. Petersburg State Electrotechnical University, St. Petersburg, 197376 Russia
e-mail: yurk@mail.ioffe.ru; iourk@yandex.ru
Received December 16, 2003

Abstract—The effects of the initial dissipation of the energy in a superconductor containing fractal clusters of a normal phase are considered. In the interval of currents preceding the resistive transition, an increase in the fractal dimension of clusters leads to an increase of the sample resistance and widening of the region of initial dissipation in the current–voltage characteristic. This is caused by an increase in the density of free vortices broken away from the pinning centers when the current flows. Dependences of the density of vortices on the fractal dimension of cluster boundaries are found for various values of the transport current. © *2004 MAIK "Nauka/Interperiodica".*

The dynamics of vortices in superconductors with fractal boundaries between the normal and superconducting phases has recently received much attention [1–3]. Nontrivial problems encountered in the description of this dynamics are of interest from the theoretical standpoint and of importance for the application of superconducting composites in electronics and power engineering, in particular, for the development of superconducting wires. It was shown [4, 5] that superconductors containing fractal clusters possess specific magnetic and transport properties. Of particular interest is the possibility of increasing the critical current by providing for enhanced pinning in the normal phase clusters with fractal boundaries [6, 7].

This paper is devoted to an analysis of the initial region of the current–voltage characteristic in the vicinity of a resistive transition in a superconductor with fractal clusters. This region reveals the voltage drop in the sample, thus evidencing the onset of the energy dissipation and breaking of the vortices away from the pinning centers, which eventually leads to the destruction of the superconducting state by the transport current as a result of the development of thermomagnetic instability.

Let us consider a superconductor containing inclusions of a normal phase with the characteristic size significantly exceeding both the coherence length and the penetration depth. A transport current in this material passes through a superconducting percolation cluster consisting of mesoscopic superconducting islands connected by weak links. Such links in high-temperature (high-T_c) superconductors are especially readily formed at various structural defects possessing small correlation lengths [8, 9]. When the transport current increases, the number of superconducting links in the cluster randomly decreases as soon as the local currents passing through these links begin to exceed the critical value and the paths become resistive. Thus, a transition of the superconductor into the resistive state corresponds to the breakdown of percolation through the superconducting cluster, whereby this infinite cluster separates into a large number of finite parts. According to these notions, the resistive transition and the accompanying energy dissipation can be considered as a current-induced critical phenomenon [10].

The dissipation of energy is determined by the vortex motion, which induces the electric field and leads to the appearance of resistance. The magnetic flux starts to move only when vortices begin to break away from the pinning centers: the flux is trapped in the normal phase clusters unless the Lorentz force caused by the transport current exceeds the pinning force. The transport current adds to persistent superconducting currents maintaining distribution of the trapped magnetic flux unchanged. The magnetic flux can be created both by an external source (e.g., during magnetization in the field cooling regime) and by the transport current (in the self-field regime). The superconducting currents circulate around the normal phase clusters through superconducting contours involving weak links. When the total current through such a link exceeds the critical value, the path becomes resistive and permeable for the magnetic flux. As a result, the current by-passes the resistive path and the Lorentz force drives vortices out through the resistive weak link.

This depinning process has a percolation character [11–13], whereby the vortices move through randomly arising transport channels. The weak links connecting normal phase clusters cross the superconducting space. This system features simultaneous percolation of the
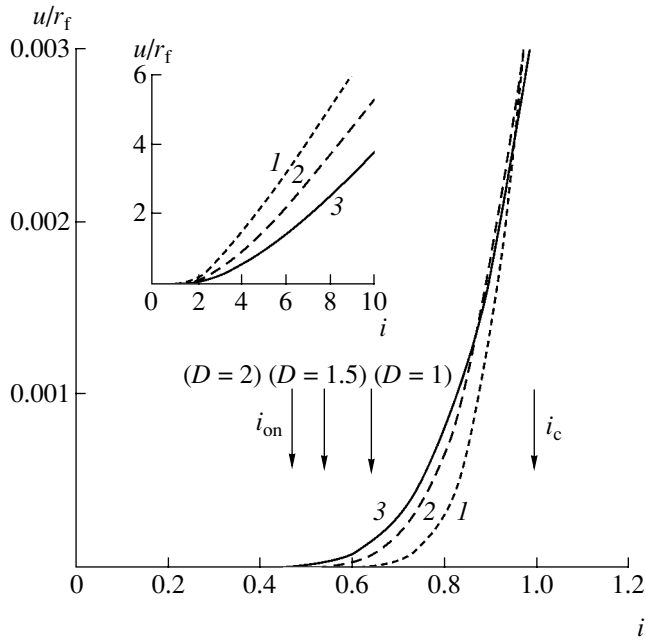
Fig. 1. The current–voltage characteristics of a superconductor with fractal clusters of various fractal dimensions $D = 1$ (*1*), 1.5 (*2*), and 2 (*3*). Arrows indicate the corresponding dissipation onset currents i_{on} determined at a level of $10^{-5}u/r_f$ and the critical current of the resistive transition.

electric current through a superconducting cluster and percolation of the magnetic flux through a system of weak links. Depending on the configuration of such channels, each normal phase cluster features its own depinning current contributing to the total critical distribution. The critical current of a cluster is proportional to the depinning force and equal to the current at which the normal phase cluster ceases to hold the magnetic flux.

In superconducting films, columnar clusters of the normal phase can be either created in the course of growth or induced by heavy ion bombardment [9, 14]. Superconducting wires are usually manufactured as threads or ribbons reinforced by a normal metal; a superconducting core always contains normal metal clusters [15, 16]. Such wires are made, for example, using bismuth-containing high-T_c superconductors of the $Bi_2Sr_2Ca_1Cu_2O_{10+y}$ (BSCCO-2212) and $Bi_2Sr_2Ca_2Cu_3O_{10+y}$ (BSCCO-2223) systems sheathed with silver [17–19]. These wires can be used in superconducting magnets, inductive energy storage devices, and electric power transmission lines. In the absence of external biasing, the magnetic flux in superconducting wires is created by the transport current. The flux concentrates along closed lines of irregular shape, deformed so as to provide for the maximum involvement of the normal phase clusters.

Of special interest are fractal clusters satisfying the scaling relationship $P^{1/D} \propto A^{1/2}$, where P is the perimeter, A is the area, and D is the fractal dimension of the cluster boundary in the cross section with a plane perpendicular to the plane of vortex motion. The boundaries of such clusters are fractal and possess fractional dimensions [20]. The influence of fractal clusters on the dynamics of a magnetic flux trapped in the normal phase was previously studied in [2–7]. The fractal character of the initial dissipation region has been experimentally established for BSCCO-2212 [21], BSCCO-2223 [21, 22], YBa$_2$Cu$_3$O$_{7-x}$, and GdBa$_2$Cu$_3$O$_{7-x}$ [10, 21] compounds.

After the onset of the vortex motion, the superconductor passes to a resistive state manifested by a finite voltage drop. In the case of an exponential-hyperbolic distribution of critical currents,

$$f(i) = \frac{2C}{D}i^{-2/D-1}\exp(-Ci^{-2/D}), \quad (1)$$

which corresponds to an exponential distribution of cluster areas [7], the current–voltage characteristic of a superconductor containing fractal clusters of the normal phase has the following form:

$$u = r_f\left[i\exp(-Ci^{-2/D}) - C^{D/2}\Gamma\left(1 - \frac{D}{2}, Ci^{-2/D}\right)\right]. \quad (2)$$

Here, $f(i)$ is the probability distribution density for the depinning currents, $i \equiv I/I_c$ is the dimensionless electric current normalized to the critical current I_c of the transition to the resistive state, $C \equiv ((2 + D)/2)^{2/(D+1)}$ is a constant factor depending on the fractal dimension D of the cluster boundary, u is the dimensionless voltage, r_f is the dimensionless flux flow resistance, and $\Gamma(\nu, z)$ is the complementary incomplete gamma function. The dimensionless voltage u and resistance r_f are related to the corresponding dimensional quantities as $U/R_f = I_c(u/r_f)$.

Figure 1 shows the current–voltage characteristics calculated using formula (2). In the range of currents $i > 1$ (presented in the inset), a growth in the fractal dimension of clusters leads to a decrease in the voltage caused by the magnetic flux motion. In the initial region corresponding to the onset of breaking of the vortices away from the pinning centers, the situation is different. As long as the transport current is below the critical value, $i < 1$, the voltage increases with the fractal dimension and the initial dissipation region extends toward smaller currents. For a quantitative description of this effect, it is convenient to introduce the current i_{on} corresponding to the onset of this regime. The value of i_{on} is determined at a level admitted by resolution of the voltage measurements. The arrows in Fig. 1 indicate the dissipation onset currents i_{on} determined at a level of $10^{-5}u/r_f$. The initial dissipation region under consideration corresponds to the interval of currents $i_{on} < i < i_c = 1$.

The significant difference in behavior of the current–voltage characteristics before and after the resistive transition is related to the dependence of the density of free vortices on the fractal dimension for various

transport currents. The resistance is determined by the density of free vortices, since the greater the number of free vortices, the stronger the electric field induced by the moving magnetic flux and, hence, the greater the voltage at a fixed transport current. The density of free vortices broken away from pinning centers by the transport current i is determined by the distribution of the depinning currents [3],

$$n = \frac{B}{\Phi_0}\int_0^i f(i')di' = \frac{B}{\Phi_0}F(i), \qquad (3)$$

where $F(i)$ is the cumulative probability function of the depinning currents, B is the magnetic induction, $\Phi_0 \equiv hc/(2e)$ is the magnetic flux quantum, h is Planck's constant, c is the speed of light, and e is the electron charge. The differential resistance of a superconductor (the slope of the current–voltage characteristic) is proportional to the density of free vortices: $R_\mathrm{d} = R_\mathrm{f}(\Phi_0/B)n$.

For the exponential-hyperbolic distribution of critical currents described by formula (1), the cumulative probability function has the form $F(i) = \exp(-Ci^{-2/D})$. Therefore, the dependence of the density of free vortices on the fractal dimension is described by the function

$$n(D) = \frac{B}{\Phi_0}\exp\left(-\left(\frac{2+D}{2}\right)^{2/D+1}i^{-2/D}\right). \qquad (4)$$

In the particular case of Euclidean clusters ($D = 1$), this formula reduces to

$$n(D = 1) = (B/\Phi_0)\exp(-3.375/i^2).$$

Figure 2 shows plots of the relative density of free vortices $n(D)/n(D = 1)$ versus the fractal dimension D for various transport currents. After the resistive transition, the density of free vortices in the interval of currents $i > 1$ decreases with increasing fractal dimension. This behavior is explained by the fact that, as the fractal dimension grows, the distribution of critical currents broadens and shifts toward greater values. In the distribution of depinning currents, the fraction of clusters most effectively trapping the magnetic flux increases and the number of vortices broken away decreases. Reduction in the density of mobile vortices leads to a decrease in the induced electric field strength and, hence, in the intensity of dissipation. The relative change in the vortex density depends on the transport current (see the inset in Fig. 2) and, in the limiting case of maximum fractal dimension $D = 2$, reaches a minimum for $i = 1.6875$ (curve 6 in Fig. 2 occurs below all other curves). This corresponds to the maximum enhancement of pinning and the minimum level of dissipation. As can be seen in the inset in Fig. 1, the voltage drop in the samples carrying the same transport current decreases with increasing fractal dimension.

In the region preceding the resistive transition ($i < 1$), the situation changes and the density of free vortices increases with the fractal dimension. Despite a
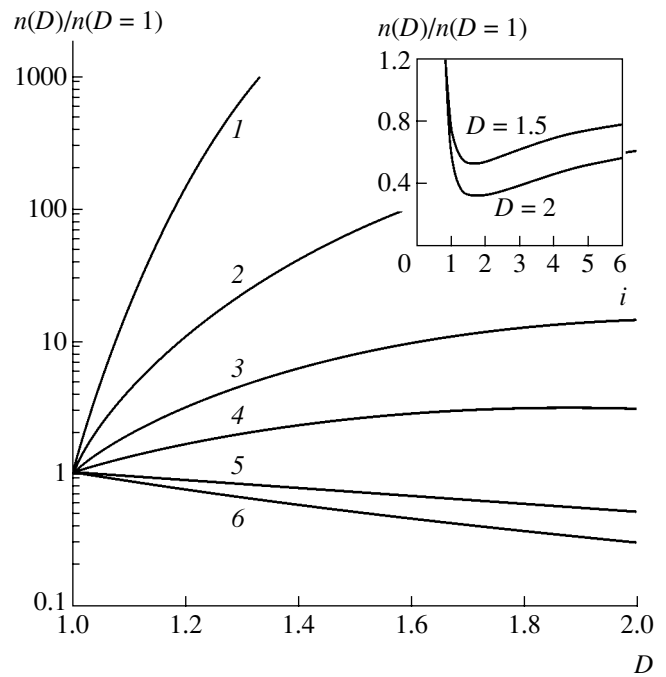

Fig. 2. Plots of the relative density of free vortices versus fractal dimension D of the normal phase clusters in superconductors for various values of the transport current i = 0.4 (1), 0.5 (2), 0.6 (3), 0.7 (4), 1 (5), 1.6875 (6). The inset shows plots of the vortex density versus current for superconductors with the fractal cluster dimensions $D = 1.5$ and 2.

sharp increase in the relative density of vortices (Fig. 2), the absolute density of free vortices in this region of the current–voltage characteristic remains small and their motion does not lead to the destruction of the superconducting state. The low density of vortices is related to the specific behavior of the exponential-hyperbolic distribution (1) at small currents: the cumulative probability function $F(i)$ has an extremely flat shape and all the derivatives $d^k F(0)/di^k = 0$ (for any k) vanish in the vicinity of the origin ($i = 0$). Even the expansion of $F(i)$ into Taylor's series at this point tends to zero, rather than to F. This behavior has a clear physical meaning. Indeed, small transport currents do not significantly affect the trapped magnetic flux, because the statistical distribution has a relatively small fraction of pinning centers with low critical currents and the vortices are virtually not broken away. Significant breaking of the vortices away begins only after the resistive transition, that is, for $i > 1$.

In any hard superconductor (of type II with pinning centers), the presence of dissipation in the resistive state does not imply the breaking of phase coherency. Some dissipation related to the motion of a small part of vortices always takes place in such superconductors at any transport current, even for very strong pinning. Therefore, in this case the critical current cannot be determined as the maximum current in the absence of dissipation. The superconducting state collapses only

when the dissipation exhibits an avalanche growth as a result of the development of a thermomagnetic instability.

Thus, the fractal properties of the normal phase clusters significantly influence the vortex dynamics in superconductors. The current–voltage characteristics of superconductors with a fractal cluster structure have two distinctive regions: the first one is before and the second one is after the resistive transition. These regions are characterized by different dependences of the density of free vortices on the fractal dimension of the normal phase cluster boundaries. After the resistive transition, the fractality of the cluster boundaries suppresses breaking of the vortices away, thus increasing the current-carrying capacity of the superconductor.

REFERENCES

1. R. Surdeanu, R. J. Wijngaarden, B. Dam, *et al.*, Phys. Rev. B **58**, 12467 (1998).
2. Yu. I. Kuzmin, Phys. Lett. A **267**, 66 (2000).
3. Yu. I. Kuzmin, Phys. Rev. B **64**, 094519 (2001).
4. Yu. I. Kuzmin, Phys. Lett. A **300**, 510 (2002).
5. Yu. I. Kuzmin, J. Low Temp. Phys. **130**, 261 (2003).
6. Yu. I. Kuzmin, Pis'ma Zh. Tekh. Fiz. **26** (17), 81 (2000) [Tech. Phys. Lett. **26**, 791 (2000)].
7. Yu. I. Kuzmin, Phys. Lett. A **281**, 39 (2001).
8. J. E. Sonier, R. F. Kiefl, J. H. Brewer, *et al.*, Phys. Rev. B **59**, R729 (1999).
9. E. Mezzetti, R. Gerbaldo, G. Ghigo, *et al.*, Phys. Rev. B **60**, 7623 (1999).
10. M. Prester, Phys. Rev. B **60**, 3100 (1999).
11. K. Yamafuji and T. Kiss, Physica C **258**, 197 (1996).
12. M. Ziese, Physica C **269**, 35 (1996).
13. M. Ziese, Phys. Rev. B **53**, 12422 (1996).
14. M. V. Indenbom, M. Konczykowski, C. J. van der Beek, and F. Holtzberg, Physica C **341**–**348**, 1251 (2000).
15. A. E. Pashitski, A. Polyanskii, A. Gurevich, *et al.*, Physica C **246**, 133 (1995).
16. I. Kováč, I. Hušek, W. Pachla, *et al.*, Supercond. Sci. Technol. **8**, 341 (1995).
17. Y. Fukumoto, Q. Li, Y. L. Wang, *et al.*, Appl. Phys. Lett. **66**, 1827 (1995).
18. M. Suenaga, Y. Fukumoto, P. Haldar, *et al.*, Appl. Phys. Lett. **67**, 3025 (1995).
19. M. Polak, W. Zhang, J. Parrell, *et al.*, Supercond. Sci. Technol. **10**, 769 (1997).
20. B. B. Mandelbrot, *The Fractal Geometry of Nature* (Freeman, San Francisco, 1982).
21. M. Prester, Supercond. Sci. Technol. **11**, 333 (1998).
22. M. Prester, P. Kováč, and I. Hušek, Proc. SPIE **3481**, 60 (1998).

Translated by P. Pozdeev

Experimental Study of the Concentration Dependence of Resistivity in Disordered Macrosystems of the Insulator–Semiconductor Type

V. A. Sotskov

Kabardino-Balkarian State University, Nalchik, Kabardino-Balkaria, Russia
e-mail: sozkov_va@rambler.ru
Received December 3, 2003

Abstract—The results of experimental investigation of the volume resistivity of a macrosystem of the insulator–semiconductor type are presented. Peculiarities in the conductivity of this system are revealed and a model is proposed which explains the observed behavior. © 2004 MAIK "Nauka/Interperiodica".

In recent years, percolation systems of the insulator–semiconductor type have been extensively studied using both experimental and theoretical methods [1–4]. However, macroscopic systems of this type are also worthy of attention [1, 2]. This Letter reports on the results of experimental investigation of the volume resistivity (ρ) of a macrosystem of the insulator–semiconductor type as a function of the bulk semiconductor content (x).

The experiments were performed for two systems with semiconductor components representing compounds of the A^8B^6 and A^1B^6 types. The former was Fe_2O_3 consisting of nearly spherical particles 25 μm in diameter, and the latter was CuO composed of particles of approximately the same size. Prior to sample melt preparation, Fe_2O_3 was demagnetized by a conventional method in an alternating magnetic field. The mixer and other equipment used for handling the samples were made of nonmagnetic materials. The insulator component in both systems was paraffin, selected due to good insulating and technological properties [4–6].

The preparation of samples was described in detail elsewhere [4]. Each sample had the form of a capacitor with solidified paraffin–semiconductor mixture of a certain concentration confined between the electrodes. The investigation was performed for flat and cylindrical capacitors with electrodes made of pure electrolytic copper. The resistance was measured by a conventional method using an E6-13A teraohmmeter. The measurements were made in the dark at a constant voltage and a temperature of 295 K.

The results of measurements are presented as $\log \rho = f(x)$ plots in the figure, in comparison with the data (curve *1*) obtained previously for an insulator–conductor (paraffin–graphite) composite [4]. As can be seen, the behavior of the insulator–semiconductor systems paraffin–CuO (curve *2*) and paraffin–Fe_2O_3

(curve *3*) exhibits certain features, which allows their curves (in contrast to curve *1*) to be subdivided into three characteristic regions. Since this behavior is identical for both insulator–semiconductor systems studied, the consideration below refers to curve *3*, containing

(i) region *AB*, where the resistivity of the composite is determined by that of the insulating matrix;

(ii) region *BC*, featuring a transition from the insulator (paraffin) to semiconductor (Fe_2O_3, CuO) proper-
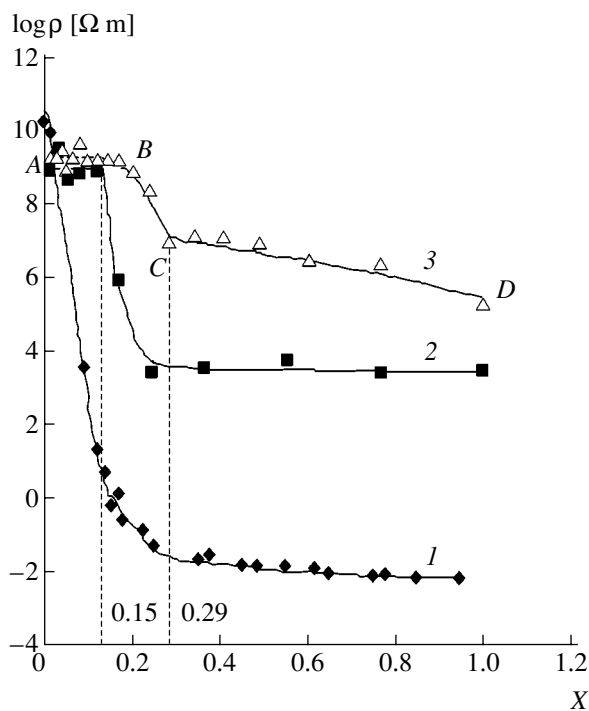
Plots of the resistivity versus composition for macrosystems (*1*) paraffin–graphite [4], (*2*) paraffin–CuO, and (*3*) paraffin–Fe_2O_3.

ties, which takes place approximately in the same concentration interval for both systems ($0.15 \le x \le 0.29$); and

(iii) region *CD*, where the resistivity is determined by that of the semiconductor component.

It should be noted that the first region is missing in the curve of the paraffin–graphite system (see curve *1* in the figure). This difference is related primarily to the large resistivity of the semiconductor materials, which is much greater than that of conductors (graphite). Assuming that the ability of Fe_2O_3 and CuO particles to form branched chains is the same as that of graphite [1, 2], we may conclude that region *AB* corresponds to the formation of a primary chain connecting (shorting) the electrodes. Indeed, according to the percolation theory, the formation of a continuous spectrum is possible for $x \ge 0.15$ [1]. However, no sharp transition to the resistivity of the semiconductor component is observed. This is explained by the contact phenomena and the relatively large resistance of the chain.

In region *BC*, the system features the formation of chains parallel to the first one, accompanied by a continuous decrease in the resistivity. This decrease ceases on approaching the value $x \approx 0.29$ (approximately the same for the two insulator–semiconductor systems studied). In other words, a kind of internal electrode is formed, which is capable of playing the role of a continuous semiconductor chain at point *B* ($x \ge 0.15$) [1, 2].

In region *CD*, the resistivity gradually decreases due to continuous formation of the internal electrode and stochastic solution of the problem of contact resistance

by means of increasing contact area. An interesting fact is that, although the bulk resistivities differ by two orders of magnitude, the transition from insulator to semiconductor properties takes place at nearly the same concentration of the semiconductor component ($0.15 \le x \le 0.29$).

In conclusion, it was shown that the curve of $\log \rho = f(x)$ for a macrosystem of the insulator–semiconductor type exhibits certain features not inherent in the insulator–conductor system.

REFERENCES

1. J. M. Ziman, *Models of Disorder: the Theoretical Physics of Homogeneously Disordered Systems* (Cambridge University Press, Cambridge, 1979; Mir, Moscow, 1982).

2. B. Sh. Shklovskiĭ and A. M. Efros, *Electronic Properties of Doped Semiconductors* (Nauka, Moscow, 1979; Springer-Verlag, New York, 1984).

3. I. A. Chmutin, S. V. Letyagin, V. G. Shevchenko, and A. T. Ponomarenko, Vysokomol. Soedin. **36**, 699 (1994).

4. V. A. Sotskov and S. V. Karpenko, Zh. Tekh. Fiz. **73** (1), 106 (2003) [Tech. Phys. **47**, 100 (2003)].

5. V. V. Pasynkov, *Materials of Electron Techniques* (Vysshaya Shkola, Moscow, 1980), pp. 155–160.

6. *Tables of Physical Data: Reference Book*, Ed. by I. K. Kikoin (Atomizdat, Moscow, 1976).

Translated by P. Pozdeev

Transformation of the Surface Structure of Bending-Strained Muscovite Crystals

S. A. Knyazev and V. E. Korsukov

Ioffe Physicotechnical Institute, Russian Academy of Sciences, St. Petersburg, 194021 Russia

Received December 16, 2003

Abstract—Transformation of the surface structure of mica (muscovite) crystals under the action of bending strain was studied by low energy electron diffraction (LEED). Anisotropic transformation was observed on the surface of thin pates cut along the crystallographic axes *a* and *b*. The results are indicative of a multistage character of the strain-induced quasi-reversible modification of the surface structure of mica on a nanometer scale. © 2004 MAIK "Nauka/Interperiodica".

Investigations of the surface structure of various substances on an atomic resolution level, performed by scanning tunneling microscopy and atomic force microscopy, are frequently carried out using objects grown on the surface of mica crystals of the muscovite type (see, e.g., [1–4]). This is related to the fact that muscovite crystals are characterized by perfect cleavage such that an atomic-smooth surface of a macroscopic area can be readily obtained by splitting along the plane of potassium ions. In most cases, the process of self-organization of the structure of substances applied onto the surface of mica is considered without taking into account the possible changes in the microrelief of the substrate surface, which may be caused by significant mechanical stresses at the boundary between mica and the deposited material. We believe that investigation of a transformation of the surface structure of mica under the action of mechanical factors is of considerable importance.

In this context, we have used low energy electron diffraction (LEED) to study changes in the surface structure of muscovite crystals strained by bending. The investigation was performed on thin (~0.04 mm thick) muscovite plates cut along the main crystallographic axes *a* and *b*. The scheme of loading is depicted in Fig. 1. The device used for bending a mica crystal was mounted on the flange of a crystal holder of a low-voltage electron diffractometer, so that it was possible to deform the sample *in situ* in the course of LEED measurements. The bending was controlled by displacing the edges of sample plate *1* held with clamps *3*, so that the central part of the sample deflected relative to the side surface of guiding cylinder *2*.

Bending of the mica crystals led to substantial changes in the shape of diffraction maxima without the appearance of new reflections. These changes were manifested simultaneously over the entire diffraction pattern, increased with the load, and exhibited a quasi-reversible character: the initial shape of LEED reflec-

tions restored almost completely upon unloading. In addition, the diffraction pattern on the luminescent screen exhibited a general shift as a whole in the direction of deformation. The observed LEED patterns did not exhibit variation with time under constant load, even for exposures up to several hours. The character of transformation of the LEED pattern was significantly different for the mica plates cut in various crystallographic directions.

Figure 2 shows evolution of the shape of one of the diffraction maxima depending on the deflection for the *a*- and *b*-cut samples. In the initial LEED patterns of the surface of an unloaded sample cut along the *a* axis (type A plate), reflections had a round shape slightly elongated toward the short edge of the plate (i.e., along the *b* axis). When the deflection reached $h = 0.5$ mm, reflections began to acquire a V-like shape: the diffraction maxima exhibited splitting with simultaneous broadening in the direction perpendicular to the axis of loading. An increase in the load to a level corresponding to $h = 1$ mm led to a growth in the separation between split reflections, the reflections again acquired a round shape, a halo appeared around each split reflection, and bands oriented in the direction of straining were formed
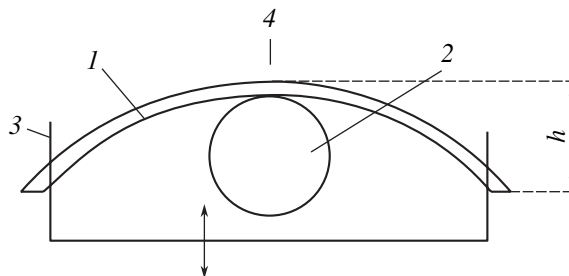
Fig. 1. The scheme of loading of a bent mica crystal in a LEED diffractometer: (*1*) mica plate; (*2*) guiding cylinder; (*3*) clamps; (*4*) probing electron beam.
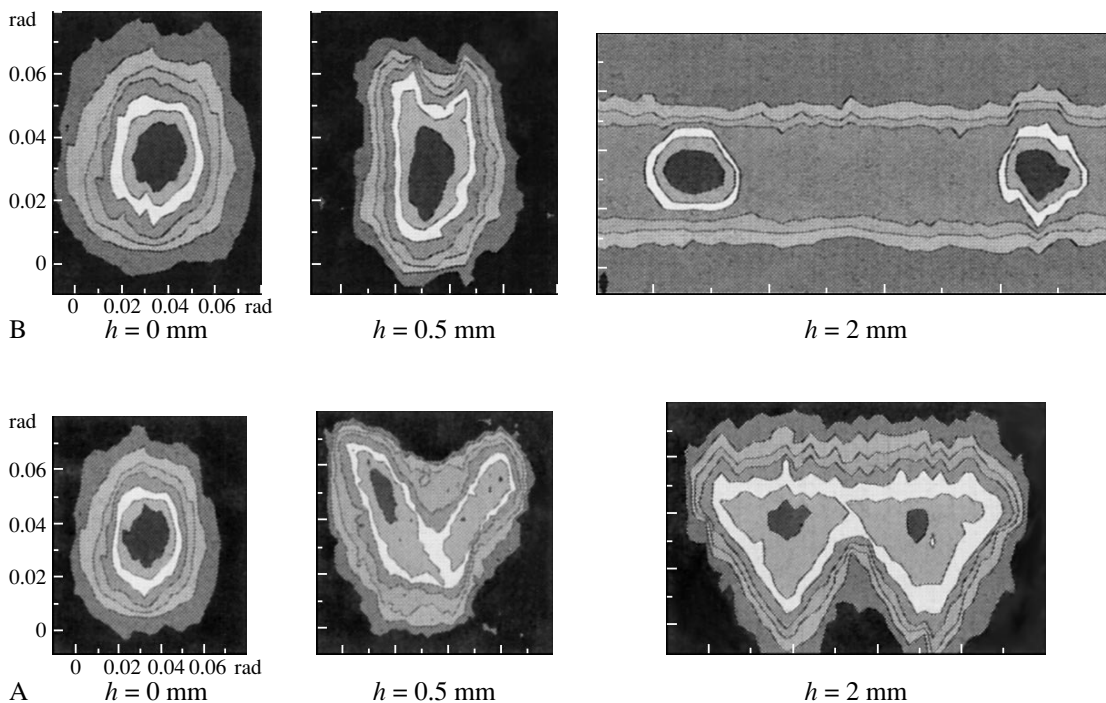
Fig. 2. Variation of the shape of a LEED diffraction maximum depending on the value of deflection of a bent mica crystal ($U = 117$ V; (02) reflection).

between reflections. This character of transformation was retained in the course of subsequent loading.

For a sample cut along the *b* axis (type B plate), the diffraction maxima exhibited splitting and acquired a V-like shape already in the first stage of bending ($h = 0.5$ mm). Subsequent deformation of the crystal was accompanied by the formation of split reflections of a triangular shape. In contrast to the previous case, the distance between split reflections was smaller (for the same deflection *h*) and bands in the direction of crystal deformation were virtually absent.

In order to evaluate the level of stresses σ developed on the surface of bending-strained mica crystal, we performed additional experiments and measured the value of deflection as dependent on the force applied to the central part of the sample plate. It was established that this dependence is linear. Based on this relation, we have determined the effective elastic modulus and calculated the stress σ according to the classical scheme. For a maximum deflection of $h = 2$ mm, the stress reached 90 N/mm².

As can be seen from the above results, the transformation of the surface structure of muscovite in the coarse of mechanical action exhibits a multistage character. The overall shift of the LEED pattern of a loaded sample is evidence of the formation of large-scale electric domains on the mica surface, with the domain size corresponding to the primary electron beam diameter (~0.7 mm). This large-scale electric structure was actually observed in the course of mica cleavage [5]. The

main changes in the LEED pattern observed in the course of mica bending are related to a transformation of the shape of diffraction maxima rather than to the appearance of new reflections and a change of distances between them. From this we conclude that these changes occur on a scale corresponding to the size of the region of coherence of electrons in the probing beam (i.e., on a level of several tens of nanometers).

As can be seen from our results presented above, the samples cut along different crystal axes exhibited both common features—generally the same character of the strain-induced changes in the surface structure (quasi-reversibility, absence of time variation at a constant load)—and significant differences in the character of transformation of the LEED pattern in the course of bending.

Caslavsky and Vedam [6] studied the surface structure of muscovite crystals by X-ray topography (the Lang method) and observed the formation of a periodic folded structure, which was attributed to anisotropic mechanical properties of mica in the (001) plane containing the crystallographic axes *a* and *b*. According to our calculations, the transition from smooth to periodic (cusped) structure leads to general splitting of the diffraction maxima in the LEED pattern in the entire range of electron beam energies. The magnitude of this splitting increases with the angle at the cusp vertex. Thus, the dynamics of reflection splitting observed in the LEED patterns of mica crystals in the course of bending can also be related to the formation of periodic structures of a nanometer size on the muscovite surface.

Previously, reflections of an "unusual" shape were observed in the LEED patterns of the surface of muscovite crystals cleaved in air, in vacuum, and in argon [8, 9]. In particular, Muller and Chang [8] reported on the appearance of triangular reflections, three-arm stars, and reflections elongated in one direction in the LEED patterns from muscovite crystals freshly cleaved in vacuum and not subjected to any mechanical action. The samples cleaved in air showed only reflections of a round shape. The conversion of V-like reflections into triplets under the action laser radiation was reported in [10]. In all these cases, the appearance of various unusual reflections was attributed to the appearance of electric dipoles making an angle of 120° relative to one another on the mica surface.

All these data indicate that the surface structure of muscovite crystals on a nanometer scale depends to a significant extent on the sample prehistory and the conditions of surface preparation, as well as on the way of rearrangement under the external action. As can be seen from Fig. 2, the formation of triangular reflections in the course of sample bending passed via the stage of V-like reflections. Moreover, the angle at the vertex of a triangular reflection also gradually changed with the load. The energy dependence of the angular size of diffraction maxima, like that observed biaxially loaded mica crystals [11], does not conform to the model of purely electrostatic influence of the field of electric domains on the LEED patterns. Therefore, the results presented in this paper cannot be reduced entirely to the formation of an electric domain structure on the surface of a strained mica crystal but rather show evidence of a multistage character of rearrangement of the muscovite crystal surface under the action of a mechanical load. This conclusion has to be taken into account in the investigation of films grown on the mica surface.

REFERENCES

1. H. Plank, R. Resel, and S. Purger, Phys. Rev. B **64**, 235423 (2001).

2. F. Balzer and H.-G. Rubahn, Appl. Phys. Lett. **79**, 3860 (2001).

3. J. Dong and G. Mao, Langmuir **16**, 6641 (2000).

4. M. Demand, M. Hehn, and R. L. Stamps, Eur. Phys. J. B **25**, 167 (2002).

5. B. V. Deryagin and M. S. Metsik, Fiz. Tverd. Tela (Leningrad) **1**, 1521 (1959) [Sov. Phys. Solid State **1**, 1393 (1959)].

6. J. L. Caslavsky and K. Vedam, J. Appl. Phys. **41**, 50 (1970).

7. S. A. Knyazev and V. E. Korsukov, Pis'ma Zh. Tekh. Fiz. **24** (13), 64 (1998) [Tech. Phys. Lett. **24**, 527 (1998)].

8. K. Muller and C. C. Chang, Surf. Sci. **14**, 39 (1969).

9. K. G. Bhattacharyya, Indian J. Chem. A **32**, 92 (1993).

10. R. Gerlach, G. Polanski, and H.-G. Rubahn, Surf. Sci. **352–354**, 485 (1996).

11. S. A. Knyazev, V. E. Korsukov, and B. A. Obidov, Fiz. Tverd. Tela (St. Petersburg) **36**, 1315 (1994) [Phys. Solid State **36**, 718 (1994)].

Translated by P. Pozdeev

Lateral Emitter as a Base Element of Integrated Emission Electronics

S. A. Gavrilov, É. A. Il'ichev, A. I. Kozlitin, É. A. Poltoratskiĭ*, G. S. Rychkov, N. N. Dzbanovskiĭ, V. V. Dvorkin, and N. V. Suetin

State Research Institute of Physical Problems, Zelenograd, Moscow, Russia
Research Institute of Nuclear Physics, Moscow State University, Moscow, Russia
* e-mail: polt@niifp.ru
Received December 22, 2003

Abstract—A field emitter is the principal element of emission electronics determining the performance of devices. We propose a lateral emitter based on carbon nanotubes for use in integrated emission electronics. The dependences of the emission current on the pulling and control fields have been studied. It is shown that the proposed lateral emitter can be used in all microelectronic analogues of vacuum tubes, from microwave devices to flat displays, the device technology being substantially integrated. © *2004 MAIK "Nauka/Interperiodica".*

Various types of vertical emitters based on carbon nanotubes (CNTs) have been described and their emission characteristics have been studied [1, 2]. The interest in these devices is related to the need for flat screens capable of replacing traditional CRT monitors, while being competitive to liquid crystal displays in the cost of production and exceeding them in the brightness characteristics. The excellent emission properties of CNTs not only offer a potential for creating the desired flat displays but also provide for the development of integrated emission devices of absolutely new types. These new devices require creating a lateral field emitter within the framework of integrated technology.

Recently, Teh *et al.* [3] proposed a method of obtaining a lateral emitter by selecting regions containing the elements of parallel nanotubes from an array of randomly oriented CNTs dispersed in a photoresist layer. The random arrangement of such regions hinders the use of photolithographic methods for the fabrication of integrations according to a preset topological pattern. Therefore, this method can only be used for obtaining separate lateral emitters. On the other hand, use of synthesized CNTs for the fabrication of lateral devices always involves a complicated process of forming, at least on one end of the nanotube, a reliable ohmic contact with a conductor, which usually has the form of a large (relative to the nanotube diameter) pad. Obviously, devices fabricated by such techniques serve only as prototypes of future integrated devices.

Previously [4, 5], we developed a technology of manufacturing lateral CNT emitters for integrated circuits with a high density of elements. A key point in the creation of an integrated emitter is the formation of a multilayer structure containing a layer of a catalytic material (iron, nickel, cobalt, etc.) ensuring the growth of carbon nanotubes. This catalytic layer is covered with a noncatalytic layer, which can be either conducting or insulating. Using lithographic techniques, a rectangular parallelepiped is formed from this structure with all side faces, except that facing the anode, also covered by a noncatalytic material. The uncovered side face exposes the edge of the catalytic layer having the shape of a narrow band with the width equal to the catalytic layer thickness (1–20 nm). Then, one of the standard methods [6] is used to grow short CNTs on the edge of the catalytic layer so as to obtain a thin "blade" with a thickness determined by that of the catalytic layer. The emission properties of CNT emitters obtained using this technology were studied in terms of the diode current-voltage characteristics [3]. It was found that the threshold field strength amounted to 1.5–2 V/μm and the current density (defined per unit length, since electrons are emitted from a linear array of CNTs) reached 5 μA/mm for a field of 5 V/μm. For using lateral CNT emitters in various devices, it is necessary to show that the emitted electron flux can be effectively controlled.

This Letter presents the results of investigation of the current of emitted electrons as a function of the strength E_G of the field generated by a control (gate) electrode (see the inset in Fig. 1). In this structure, the control electrode G is situated above the plane of the emitter E and collector C and partly hangs over both the emitter and collector pads. The emitter was grounded and a positive bias voltage V_C was applied to the collector, creating the field E_{EC} between the collector and emitter. A control voltage applied to electrode G created the field E_{GE} with a strength varying from zero to –5 V/μm.

Figure 1 shows plots of the emission current I_{EC} versus field strength E_{GE} for two values of the collector voltage, corresponding to $E_{EC} = 4.8$ and 3.6 V/μm. As can be seen, the collector current is completely blocked when E_{GE} amounts to about half of E_{EC}. Measurements of the gate current showed that it does not exceed 10^{-9} A/mm for $0 \leq E_{GE} \leq 5$ V/μm. These results show that, using the proposed emitter, it is possible to create a complete analogue of a vacuum tube on a microscopic and nanodimensional level, thus providing the base elements for integrated emission electronics.

Using this approach, the principles of construction developed for the entire spectrum of devices based on electron tubes can be automatically implemented in integrated circuits of emission electronics. However, it should be borne in mind that emission devices based on CNTs possess a high operation speed, which is explained primarily by the high current density. For example, one CNT with a diameter of 20–40 nm is capable of emitting a current in excess of 1 μA [4]. Simple estimates show that the switching time in such elements can be less than 10^{-12} s, which corresponds to a transmission frequency band of such "electron nanotubes" on the order of several terahertz.

It should be emphasized that electron nanotubes can provide for the possibility of using the range of frequencies between superhigh frequency (SHF) band and the lowest frequencies of the optical spectrum. In this case, it will also be necessary to develop the technology of resonators, waveguides, couplers, etc., with dimensions on the order of several tens of microns. These technologies are now extensively developed as a basis of micromechanics. Thus, use of lateral CNT emitters can provide for a breakthrough of emission electronics into the field of terahertz communications. Moreover, since the resonance frequencies of the molecules of many gases and solids also fall within the terahertz range, the development of integrated generators and detectors for this spectral range will provide for the development of miniature sensors detecting gases or substances by means of spectral analysis.

CNT-based vertical emitters of various design are now extensively studied by numerous research groups primarily with a view to the development of flat field-emission displays. Lateral emitters can also be used as base elements for such a display. Figure 2 shows plots of the currents via two collectors in a scheme with a common lateral emitter occurring at a voltage of −480 V. The first collector is situated in the same plane as the emitter, is spaced from it by 100 μm, and occurs at a zero potential. The second collector is situated 200 μm above the emitter plane and partly hangs over the emitter and the first collector. In Fig. 2, the currents are plotted versus the voltage V_{2C} applied to the second collector. As can be seen, the current via the second emitter is zero for $V_{2C} = 0$ and amounts to ~50% of the
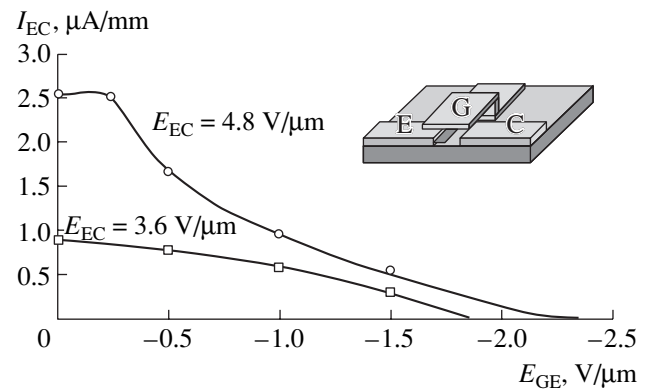

Fig. 1. Plots of the emitter–collector current I_{EC} versus control field strength E_{GE} for two values of the emitter–collector field strength in a gated cell with a lateral CNT emitter schematically depicted in the inset (see text for explanations).
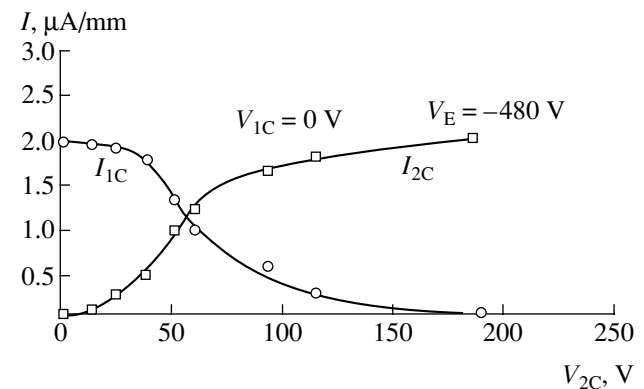

Fig. 2. Plots of the currents via the first and second collector versus voltage applied to the second collector in a cell with a common lateral CNT emitter ($V_{1C} = 0$ V; $V_E = -480$ V).

emitter current for $V_{2C} = 50$ V. It is important to note that electrons striking the second collector have an energy of ~500 eV. Therefore, if this collector is replaced by a transparent electrode coated with a phosphor and biased to 10–100 V, the phosphor will be bombarded by electrons with an energy of 500–1000 eV. This suggests a simple design of the flat color field-emission display. The device is based on two plates. One of these bears two arrays of elements, representing lateral emitters and first collectors. The other plate is transparent and bears three surface arrays, representing transparent electrodes coated with a phosphor of the appropriate luminescent color. The plates are parallel, the surfaces bearing arrays face each other, and the arrays are mutually perpendicular.

In conclusion, it was shown that the proposed lateral CNT emitter can perform the function of a vertical emitter. This circumstance provides for a high flexibility in the design of integrated circuits, solving the prob-

lem of intersections via electron emission from one plane to another.

REFERENCES

1. D. S. Y. Hsu, Appl. Phys. Lett. **80**, 2988 (2002).

2. D. Li and J. Zhang, J. Vac. Sci. Technol. **19**, 1820 (2001).

3. A. S. Teh, S.-B. Lee, and K. B. K. Teo, Microelectron. Eng. **67**–**68**, 789 (2003).

4. S. A. Gavrilov, N. N. Dzbanovsky, V. V. Dvorkin, *et al.*, in *Proceedings of the 11th International Symposium "Nanostructures: Physics and Technology," St. Petersburg, 2003*, pp. 234–236.

5. S. A. Gavrilov, N. N. Dzbanovsky, V. V. Dvorkin, *et al.*, in *Proceedings of the International Conference "Micro- and Nanoelectronics-2003," Moscow–Zvenigorod, 2003*, pp. 1–27.

6. A. Huczko, Appl. Phys. A **74**, 617 (2002).

Translated by P. Pozdeev

Jointing Fragments of a Speckle Diffuser

Yu. N. Denisyuk[a], E. B. Brui[a], N. M. Ganzherli[b], and V. V. Orlov[a,*]

[a] *Vavilov Optical Institute, State Scientific Center of the Russian Federation, St. Petersburg, 190164 Russia*
[b] *Ioffe Physicotechnical Institute, Russian Academy of Sciences, St. Petersburg, 194021 Russia*
* *e-mail: orlov@soi.spb.su*
Received December 4, 2003

Abstract—A method of matching adjacent fragments in a speckle diffuser is proposed which makes it possible to fabricate large area diffusers having the same scattering indicatrix over the entire device area. © *2004 MAIK "Nauka/Interperiodica".*

The formation of stereo images by the method proposed in [1] requires a speckle diffuser. This device can be manufactured by recording a pattern of speckles, arising during the scattering of a coherent radiation from a ground glass, in a photosensitive medium. Previously [2], we developed a method of obtaining such speckle diffusers via photochemical treatment of standard photographic plates of the PFG-03G type. A speckle diffuser of a large size cannot be recorded using one exposure. In this case, separate fragments of the photosensitive medium are sequentially exposed and there arises the problem of jointing these fragments so as to provide that the scattering indicatrix is the same at the boundaries and inside the fragments. In particular, zero-order diffraction at the joints of fragments has to be suppressed.

In this paper, we will consider different methods of jointing fragments in a speckle diffuser. The first method (superposition) consists in that the edges of adjacent exposed fragments are superimposed onto each other (Fig. 1). As a result, the value of exposure in the region of overlap is two times that outside. The second method (superposition with leveled exposure) provides for superimposition in a manner such that the exposure in the region of overlap is equal to that inside the fragments. For this purpose, the edge of a diaphragm masking the fragment is moved at a constant velocity during the exposure. During exposure of the first fragment, diaphragm $D1$ moves from position A to B (Fig. 2), and during the second exposure, diaphragm $D2$ moves from position B to A. As a result, the exposure in the region of overlap is the same as that inside each fragment.
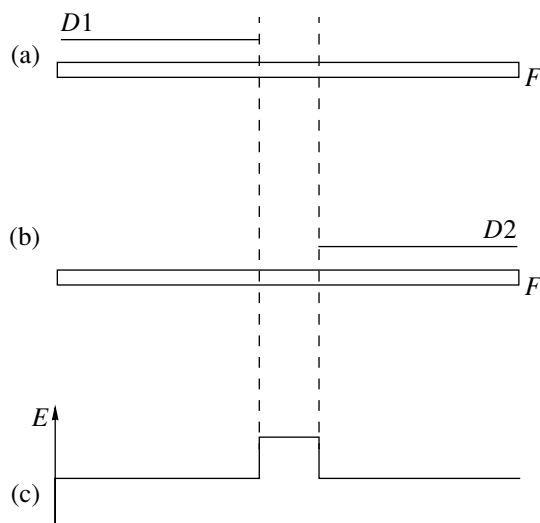

Fig. 1. Schematic diagrams illustrating the recording of a speckle diffuser by the method of superposition: ($D1$, $D2$) diaphragms; (F) photographic plate; (a) exposure of the first fragment; (b) exposure of the second fragment; (c) exposure profile over the plate surface.
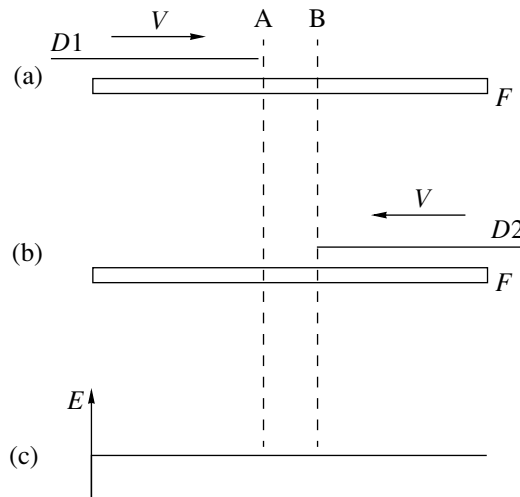

Fig. 2. Schematic diagrams illustrating the recording of a speckle diffuser by the method of superposition with leveled exposure: ($D1$, $D2$) diaphragms moved at velocity V during the exposure; (F) photographic plate; (a) exposure of the first fragment; (b) exposure of the second fragment; (c) exposure profile over the plate surface.
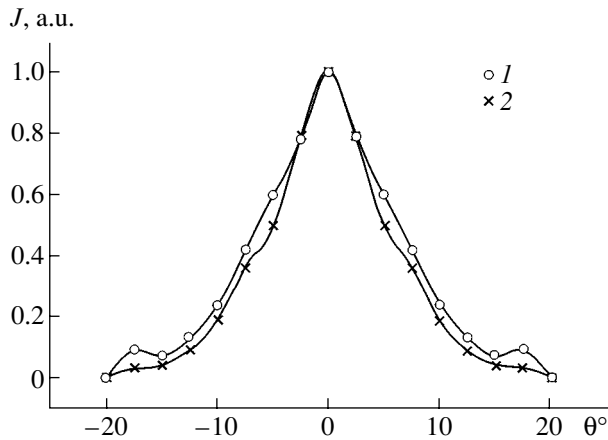
J, a.u.

Fig. 3. Scattering indicatrices of a speckle diffuser composed of two fragments recorded by the method of superposition with leveled exposure, measured (*1*) inside and (*2*) the region of overlap.

These methods were used for jointing the fragments of two speckle diffusers recorded in a PFG-03G plate. The plate was exposed to radiation of a He–Ne laser scattered from a 8×8-mm ground glass plate placed at a distance of 77 mm from the photographic plate. The dimensions of fragments were 15×15 mm, and the superimposition zone was 3 mm wide. The speckle pattern recorded in each fragment was not correlated with that recorded in the other fragment. In order to provide for this, the ground plate was given a small transverse shift between the two exposures. The exposed photographic plates were subjected to the following chemicophotographic treatment.

An image formed in the photoemulsion layer upon this treatment consists of three components: whitened silver grains, hardened gelatin, and surface relief. The amplitude of phase modulation of the light wave in each component significantly depends on the difference of optical densities in the exposed and unexposed

Table

Step no.	Operation
1	Development (PRG developer)
2	Washing in water
3	Enhancement (Ag$^+$-containing solution)
4	Washing in water
5	Fixation (F8 fixer)
6	Washing in water
7	Bleaching (modified R10 bleach)
8	Washing in water
9	Dehydration (50 and 100% isopropanol solutions)
10	Drying in air

regions of photoemulsion. In the absence of fogging, this difference is determined by the maximum degree of blackening achieved in the course of development.

The proposed chemicophotographic treatment upon an exposure of 0.5 mJ/cm^2 provided for the obtaining of each separate fragment of the speckle diffuser free of zero-order diffraction. By zero-order diffraction, we imply a radiation component passing without scattering through the diffuser illuminated with a collimated beam of radiation of a He–Ne laser. At the same time, the zones of superimposition showed evidence of zero-order diffraction in the joints obtained by both methods. The appearance of zero-order diffraction is related to a decrease in the image contrast in the region of overlap.

In order to improve the contrast, we reduced the degree of fogging in the photoemulsion layer by means of low-temperature development. This method ensures simultaneous and homogeneous development throughout the whole layer (at a sufficiently high degree of blackening) and strongly retards fogging. In this particular case, the temperature of a developing solution was reduced from 20 to 6°C, while the development duration was increased from 15 to 60 min. The enhancement step was also performed at a reduced temperature. As a result of these measures, the intensity of zero-order diffraction in the region of overlap between the two fragments jointed by the first method (superposition) decreased from 10 to 2% of the incident beam intensity. In the joint obtained by the second method (superposition with leveled exposure), the zero-order diffraction was completely absent. The percentage diffraction efficiency of a speckle diffuser, determined as the ratio of intensities of the scattered and incident radiation, amounted to 75%.

Figure 3 shows the scattering indicatrices of a speckle diffuser composed of two fragments jointed using the method of superposition with leveled exposure. One of these curves was measured outside the zone of superimposition, while the other refers to the region of overlap. As can be seen, the two curves virtually coincide.

Thus, using the method of superposition with leveled exposure, it is possible to solve the problem of jointing fragments of speckle diffusers and makes it possible to obtain large-area devices.

REFERENCES

1. Yu. N. Denisyuk, Pis'ma Zh. Tekh. Fiz. **22** (9), 92 (1996) [Tech. Phys. Lett. **22**, 385 (1996)].

2. Yu. N. Denisyuk, V. B. Markov, and N. M. Ganzherli, Opt. Spektrosk. **84**, 104 (1998) [Opt. Spectrosc. **84**, 94 (1998)].

3. E. B. Bruĭ and V. V. Orlov, Pis'ma Zh. Tekh. Fiz. **24** (5), 70 (1998) [Tech. Phys. Lett. **24**, 197 (1998)].

Translated by P. Pozdeev

The Long-Range Action of Light on the Microhardness of Metals in Stratified Heterogeneous Systems

D. I. Tetelbaum*, Yu. A. Mendeleva, and A. Yu. Azov

Physicotechnical Research Institute, Nizhni Novgorod State University, Nizhni Novgorod, Russia
* e-mail: Tetelbaum@phys.unn.runnet.ru
Received October 1, 2003

Abstract—The long-range action of light on the mechanical properties (microhardness) of metals (photomechanical memory effect) takes place both in a single foil and in a stack of foils made of the same or different materials. The result of irradiation depends not only on the materials of foils in a stack but also on the presence of native oxide layers on each foil. Etching of the oxide layers and growth of the new ones, as well as interruptions in the exposure, lead to an increase in the effect of irradiation under the conditions studied. The possible mechanisms of the observed effects are discussed. © *2004 MAIK "Nauka/Interperiodica"*.

Introduction. Recently, we discovered a new phenomenon whereby the exposure of a metal foil to light leads to a change in the microhardness H on the rear side of the foil, even when the regime of irradiation is such that the observed changes cannot be explained by thermal effects [1–7]. This phenomenon was called the photomechanical memory of metals, because the light-induced changes are retained upon irradiation. It was established that a necessary condition for the manifestation of this effect is the presence of a native oxide layer on the irradiated side of the foil. A metal foil with native oxide layers on its surfaces is a heterogeneous system comprising the metal proper and thin dielectric (oxide) films. A more complex heterogeneous system is offered by a stack of two or more foils, where various combinations of oxide layers present or absent on some foils are possible. The investigation of peculiarities of the photomechanical memory manifestations in various stratified compositions comprising metal and oxide layers would provide information about the interaction of components in such stratified systems and elucidate the mechanism of the photomechanical memory effect.

Previously [8], we reported on a long-range effect of irradiation on the microhardness of foils in a stack. In this paper, we present and discuss the results of experiments with stratified heterogeneous systems represented by single foils and stacks of two foils.

Experimental methods. The experiments were performed with rolled foils of two materials: permalloy 79 (20 μm thick) and a multicomponent nanocrystalline iron-based alloy 5BDSR (30 μm thick). These alloys were chosen because permalloy 79 is a model material for which most of the previous photomechanical memory investigations were performed, while 5BDSR alloy also exhibits significant changes in the microhardness on the rear side of an irradiated foil.

The radiation source was a 20-W incandescent lamp producing a light power of 10 W. The distance from the source to the foil surface was 5 cm, and the exposure time was 10 s. In permalloy 79 foils, this regime of irradiation corresponds to the first minimum (i.e., the maximum absolute value) in the plot of the relative change of the microhardness ($\Delta H/H_0$) versus the irradiation dose [4, 5].

The microhardness H of a foil was measured on a PMT-3 device before irradiation and then within 10 min after exposure. This limitation on the time after irradiation is related to the fact that the microhardness exhibits relaxation after termination of the exposure, which usually becomes significant in about 1 h. The experimental procedure and error evaluation were described in detail elsewhere [9]. The load P used for the measurement of H were selected on a plateau of the $P(H)$ curves and amounted to 20 g for permalloy 79 and 50 g for 5BDSR alloy. According to our previous data [9], changes in the H value exceeding 4% can be considered significant. The native oxide layers were removed by etching in hydrochloric acid (HCl) not interacting with base metals. All experiments were repeated so as to exclude artifacts and make the results sufficiently reliable.

Experimental results. Prior to the experiments with stacked foils, we studied the effect of repeated exposures (with and without removal of the native oxide layers) on a single foil of permalloy 79. Previously [4, 5], it was established that irradiation in the regime indicated above leads to a relative change in H on the unirradiated (rear) side amounting to $\Delta H/H_0 = -20\%$. In foils of 5BDSR alloy, the relative change in microhardness on the rear side was $\Delta H/H_0 = +20\%$. On the exposed surface, the relative change in H for the foils of both materials was insignificant. In both cases, removal of the native oxide layer from the exposed surface by etching eliminated the effect of irradiation on
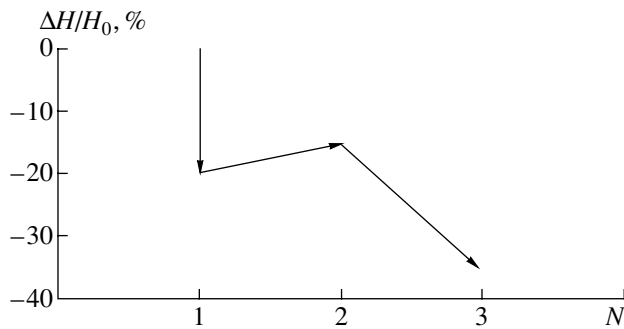
$\Delta H/H_0, \%$

Fig. 1. Diagram showing the relative changes in the microhardness in the course of experiment 1 including the sequential operations of (1) irradiation of a foil, (2) etching of the native oxide film and holding the foil in air, and (3) the second irradiation.
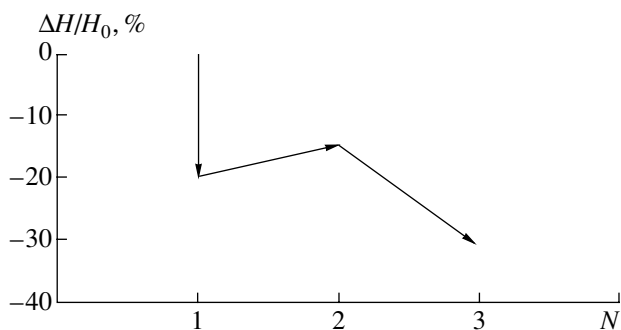
$\Delta H/H_0, \%$

Fig. 2. Same as in Fig. 1, but without etching of the native oxide in the second step.

the microhardness, provided that the period of time between etching and irradiation was not very long. The results of experiments with single and stacked foils were as follows.

Experiment 1: repeated irradiation of a single foil of permalloy 79. Sequence of operations: irradiation; measurement of H on the rear side; etching of the native oxide layer; 30-min exposure in air (growth of the new oxide layer); second irradiation; and microhardness measurement. The results are schematically presented in Fig. 1, showing that the second exposure leads to a greater change in H than a single irradiation of the same foil. Figure 2 shows the results of an experiment with the same sequence of operations except that the native oxide was not removed by etching prior to the second exposure. As can be seen, the second irradiation also increases the effect.

Experiment 2: irradiation of a stack of two permalloy 79 foils. Relative changes in the microhardness on the front and rear side of the second (lower) foil were $\Delta H/H_0 = -10$ and -35%, respectively. Thus, irradiation of the first (upper) foil leads to a change in microhardness of the second (screened) foil, which is even more pronounced than that observed in a single foil. Moreover, in contrast to the case of a single foil, a significant change in H is observed on the front surface of the

screened foil. Therefore, screening enhanced the effect of light rather than eliminating its action.

Experiment 3: same as experiment 2, but the upper foil material is 5BDSR alloy. Relative changes in the microhardness on the front and rear side of the second foil were $\Delta H/H_0 = -20$ and -26%, respectively. The absolute value of $\Delta H/H_0$ on the rear side of the second foil is still greater than that for a single foil of permalloy 79. The change in the microhardness of the front side of the second foil is more pronounced as compared to that observed in experiment 2. Therefore, the screening-enhanced effect takes also place for the stacked foils made of different materials.

Experiment 4: same as experiment 2, but the native oxide layer was removed from the exposed surface of the upper foil prior to irradiation. In this case, the exposure did not change the microhardness in either the first or second foil.

Experiment 5: same as experiment 2, but the native oxide was removed from both front and rear sides of the second foil. The change in the microhardness on the rear side of the first foil was the same as that observed for a single foil of permalloy 79, while the microhardness of the second foil remained unchanged. Thus, the presence of a native oxide layer is also a necessary condition for the manifestation of the effect under consideration in the screened foil.

Experiment 6: same as experiment 3, but the native oxide layer was removed from the exposed surface of the upper foil (5BDSR alloy) prior to irradiation. In this case, $\Delta H/H_0 = 0$ on both sides of the second foil. This result coincides with that observed for the irradiation of two foils made of the same material when the native oxide layer was removed from the exposed surface of the upper foil.

Discussion of results. The results of experiments described above show that the long-range effect of light on metals is also observed in stratified heterogeneous systems involving, besides metals, at least one dielectric layer (in this case, native oxide). These results provide additional information for constructing models of the phenomenon under consideration.

Krivelevich [10] proposed a theoretical explanation of the long-range effect based on the generation and propagation of a "switching wave" in the presence of an energy flux in a system possessing more than one local minimum of the free energy. This mechanism does not require that the energy flux produce significant heating. The existence of several minima of the free energy in the materials studied (rolled foils) can be ensured, for example, by the presence of a system of defects capable of occurring in various states. This theory also applies to a system of stacked foils of the same or different materials (experiments 2 and 3) and explains the identical character of microhardness variations under the action of various types of radiation, including ions, electrons [8], and photons.

However, our data presented above and those reported previously [6] on the role of the native oxide layer show that the presence of an energy flux alone (unless it is very powerful) is insufficient to provide for the photomechanical memory effect and requires additional stimulation of the system of defects in a metal. This stimulation can be provided by deformation waves arising in the native oxide and then penetrating into the metal. Previously [6, 7], we suggested that nonlinear deformation waves are generated by the Coulomb forces when photoelectrons are captured by traps in the dielectric native oxide. As different groups of traps are saturated in the course of irradiation, the character (amplitude and shape) of the deformation waves can change. It would be reasonable to assume that such a change in the character of deformation waves may be one of the factors accounting for the complicated non-monotonic dose dependence of the microhardness [4, 5]. After termination of the exposure, the traps may discharge ("rest"); the second irradiation (experiment 1) will change $\Delta H/H_0$ in the same direction as before the interruption, whereas in the absence of rest, the direction of microhardness variation (in the regime used for the irradiation of permalloy 79 foils) changes to the opposite [4, 5]. Analogous considerations explain the results of experiments with etching of the old (irradiated) and growth of the new oxide layer.

The results of our experiments with a stack of two foils show that, for the effect to be manifested in the second foil, it is necessary that the native oxide layer be present not only on the exposed foil but on the front side of the screened foil as well (see experiments 4–6). This fact can be explained as follows. We assume that the radiation-induced reconstruction of the system of defects in the first foil not only changes the microhardness of the rear side of this foil but also stimulates the emission (exoemission) of particles (electrons or ions) from this side. The emitted particles, trapped in the native oxide layer on the front surface of the second foil, generate deformation waves in this layer. At the same time, the deformation waves generated in the first foil are probably strongly absorbed or scattered at the interface and weakly (or not at all) penetrate into the second foil. This explains the absence of changes in the microhardness of the second foil with removed native oxide.

Another important result is the enhancement of the photomechanical memory effect in irradiated stacks (experiments 2 and 3). Previously, the long-range effects observed for the ion irradiation led to the conclusion [11] that the deformation waves can increase upon interaction with extended defects. In the case of the photomechanical memory effect, this amplification of the deformation waves can explain the paradoxical facts that H changes more significantly on the rear side of the first foil than on its exposed side, and on the rear side of the screened foil as compared with the rear side of the first foil.

Thus, in explaining the results of such experiments, it is important to take into account the active role of components in stratified systems. Within the framework of the proposed interpretation, this active role is manifested in (i) the generation of deformation waves (in the native oxide layer), (ii) exoemission (at the rear surface of the foil), (iii) the amplification of deformation waves due to their interaction with extended defects, and (iv) the absorption and scattering of deformation waves (at the interfaces). The existence of these processes is still a hypothesis. Their direct observation and theoretical explanation are the tasks of subsequent investigations.

REFERENCES

1. D. I. Tetelbaum, A. A. Trofimov, A. Yu. Azov, *et al.*, Pis'ma Zh. Tekh. Fiz. **24** (23), 9 (1998) [Tech. Phys. Lett. **24**, 910 (1998)].

2. D. I. Tetelbaum, V. A. Panteleev, A. Yu. Azov, *et al.*, Poverkhnost, No. 5, 87 (2000).

3. D. I. Tetelbaum, A. Yu. Azov, M. V. Gutkin, *et al.*, Vestn. NNGU, Ser. Fiz. Tverd. Tela **1**, 263 (2000).

4. D. I. Tetelbaum, A. Yu. Azov, E. V. Kuril'chik, *et al.*, Vacuum **70**, 169 (2003).

5. D. I. Tetelbaum, E. V. Kuril'chik, A. Yu. Azov, *et al.*, Poverkhnost, No. 4, 67 (2003).

6. D. I. Tetelbaum, A. Yu. Azov, and P. I. Golyakov, Pis'ma Zh. Tekh. Fiz. **29** (2), 35 (2003) [Tech. Phys. Lett. **29**, 57 (2003)].

7. D. I. Tetelbaum, Yu. A. Semin, V. V. Khabibulov, *et al.*, Proc. SPIE **3687**, 264 (1999).

8. D. I. Tetelbaum, E. V. Kuril'chik, and N. D. Latisheva, Nucl. Instrum. Methods Phys. Res. B **127–128**, 153 (1997).

9. D. I. Tetelbaum and A. Yu. Azov, Vestn. NNGU, Ser. Fiz. Tverd. Tela **2**, 120 (2001).

10. S. A. Krivelevich, Vestn. NNGU, Ser. Fiz. Tverd. Tela **2**, 71 (1998).

11. P. V. Pavlov, Yu. A. Semin, V. D. Skupov, *et al.*, Fiz. Tekh. Poluprovodn. (Leningrad) **20**, 503 (1986) [Sov. Phys. Semicond. **20**, 315 (1986)].

Translated by P. Pozdeev

Intermittency of Space Charge Waves

Yu. N. Zaiko

Volga Region Academy of State Service, Saratov, Russia
e-mail: zyrnick@lycos.com
Received December 30, 2003

Abstract—Intermittency of the nonlinear waves in one-dimensional flow of charged particles is studied. A two-mode solution is obtained in the frame moving with the space charge wave. The second mode corresponds to modulation of the fundamental (first) mode. A resonance interaction of the two modes can lead to a sharp change in the phase trajectory parameters, which is manifested by random variation of the wave amplitude. Calculations are simplified by using a method based on the formal quantization of the classical solution. The corresponding Schrödinger equation is obtained, the solution of which formally coincides with that of the well-known Coulomb problem. The probability of transitions between levels with different azimuthal quantum numbers corresponding to different amplitudes of the classical solution is calculated. The probability distribution function $W(\Delta\Phi)$, where $\Delta\Phi$ is the phase length of a regular (laminar) part of the trajectory, is determined using the "azimuthal number–angle" uncertainty relation. © *2004 MAIK "Nauka/Interperiodica"*.

Intermittency is one of the manifestations of turbulence, whereby sharp irregular perturbations appear on the background of a regular behavior of some quantity such as, for example, the velocity of a turbulent flow. Both the time of appearance and the magnitude of such perturbations exhibit a random character [1]. The physics of this phenomenon is related to the interaction of at least two waves, in particular, the fundamental harmonic and its subharmonic, involving the energy transfer from one of these waves to another. When the amplitude of the subharmonic becomes comparable with the initial amplitude of the fundamental harmonic, the former amplitude exhibits a sharp increase and establishes on a random level. The lower this level, the longer the so-called laminar period [1].

Let us consider a problem concerning the space charge waves in a one-dimensional flow of charged particles propagating along the z axis as described by the system of equations

$$\frac{\partial v}{\partial t} + v\frac{\partial v}{\partial z} = \frac{e}{m}\frac{\partial \varphi}{\partial z}, \quad \frac{\partial n}{\partial t} + \frac{\partial}{\partial z}(nv) = 0,$$

$$\frac{\partial^2 \varphi}{\partial z^2} = 4\pi e(n - n_0), \tag{1}$$

where $-e$ and m are the particle charge and mass, respectively; φ is the space charge potential; v is the particle velocity; n and n_0 are the current number density of particles and its equilibrium value, respectively; and t is the time. In a frame of reference where the wave is at rest ($u = 0$), stationary waves (i.e., the waves with unperturbed phase) depending on $z–ut$ are described by

a solution [2] used below as the unperturbed solution of Eqs. (1):

$$\frac{dv}{dz} = \pm\omega_p\frac{\sqrt{A^2 - (v - v_0)^2}}{v},$$

$$z - z_0 = \pm\frac{1}{\omega_p}\int\frac{v\,dv}{\sqrt{A^2 - (v - v_0)^2}}. \tag{2}$$

Here, A is the wave amplitude, $\omega_p = (4\pi e^2 n_0/m)^{1/2}$ is the plasma frequency, and v_0 is the average flow velocity. This solution offers an example of solutions depending on a single phase (called single-phase solutions). Below, we will consider the method of obtaining two-phase solutions [3] which, due to the presence of resonances, can lead to a complex dynamics and, hence, to a statistical behavior of the system under consideration [4].

In this paper, it is suggested to study the statistical properties of the system using a method based on the formal procedure of quantization of solution (2). Let us introduce the following Hamiltonian for this solution:

$$H(p_v, p_\chi, v) = \frac{p_v^2}{2} - \frac{p_\chi^2}{2v^2} - \frac{\omega_p^2 v_0}{v} + \frac{\omega_p^2}{2},$$

where $p_v = dv/dz$ and $p_\chi = v^2 d\chi/dz$ are the momenta, velocity v plays the role of a coordinate, and z plays the role of time. The cyclic coordinate χ is determined by the relation $d\chi/dz = \omega_p(v_0^2 - A^2)^{1/2}/v^2$; for $A \longrightarrow 0$, this coordinate coincides to within a constant with the phase of the stationary solution (2): $\Phi = \omega_p(z - z_0)/v_0$. The meaning of this constant is elucidated below. This form

of Hamiltonian reflects the symmetry of solution (2). Solution (2) can be obtained from the following Hamilton equations:

$$\frac{dv}{dz} = \frac{\partial H}{\partial p_v}, \quad \frac{d\chi}{dz} = \frac{\partial H}{\partial p_\chi}, \quad \frac{\partial p_v}{\partial z} = -\frac{\partial H}{\partial v},$$

$$\frac{\partial p_\chi}{dz} = -\frac{\partial H}{\partial \chi} = 0.$$

The last of these equations implies the existence of invariant

$$I_\chi = p_\chi = \omega_p (v_0^2 - A^2)^{1/2},$$

the second invariant being

$$I_v = \frac{1}{2\pi}\oint p_v dv = \omega_p [v_0 - (v_0^2 - A^2)^{1/2}].$$

Representing the velocity v by a vector on the "velocity–phase" plane with the polar coordinates (v, χ) and integrating the equation for χ using solution (2) (with plus sign), we obtain an equation for the trajectory of a point imaging the motion of the system on the "velocity–phase" plane. This trajectory has the form of an ellipse: $v = (v_0^2 - A^2)/(v_0 - A\sin\chi)$. This representation of solution (2) is more convenient than the well-known representation in terms of the implicit function, $v = v_0 + A\sin[\Phi - 1/v_0(A^2 - (v - v_0)^2)^{1/2}]$.

Now, let us derive the Schrödinger equation for the wave function $\psi(v, \tilde{t})$ proceeding from the principle of correspondence. Omitting intermediate algebra, we can write the final equation as

$$-i\hbar\frac{\partial\psi}{\partial\tilde{t}} = -\frac{\hbar^2}{2m}\Delta\psi + U\psi, \quad U = -\hbar\omega_p\frac{2v_0}{v},$$

$$\Delta = \frac{1}{r}\frac{\partial}{\partial r}\left(r\frac{\partial}{\partial r}\right) + \frac{1}{r^2}\frac{\partial^2}{\partial\chi^2}; \quad r = \frac{v}{\omega_p\sqrt{2}}; \quad \tilde{t} = \frac{z}{v_0}. \tag{3}$$

The classical stationary solution (2) obeys the relation $\psi \sim \exp(-i\omega_p t + il\chi)$, where l is an integer. Introducing the new variable $\rho = 2\omega_p v/\mu$ (where $\mu = (\hbar\omega_p/m)^{1/2}\omega_p$ and $\hbar$ is the Planck constant) and denoting $s = \omega_p v_0/\mu$ and $l'(l' + 1) = p_\chi^2/\mu^2 = (v_0^2 - A^2)\omega_p^2/\mu^2$, $l' = l - 1/2$, we obtain an equation for $R(\rho) = (\mu/2\omega_p)^{1/2}\rho^{-1/2}\psi$:

$$R'' + \frac{2R'}{\rho} + \left[-\frac{1}{4} + \frac{s}{\rho} - \frac{l'(l' + 1)}{\rho^2}\right]R = 0. \tag{4}$$

In terms of these variables, the amplitude A and the average flow velocity v_0 are given by the expressions $v_0 = (\hbar\omega_p/m)^{1/2}s$ and $A^2 = \hbar\omega_p/m[s^2 - l'(l' + 1)]$. In

quantum mechanics, Eq. (4) describes the atom of hydrogen [5]. Substituting $R(\rho) = \rho^{l'}e^{-\rho/2}w(\rho)$ ($l' \geq 0$), we obtain an expression for the square-normalized solutions of Eq. (4): $w = F(-s_r, 2l' + 2, \rho)$, where $s_r = s - l' - 1$ is the radial quantum number (nonnegative integer) and F is the degenerate hypergeometric function.

The perturbations of solution (2), which are represented by the terms $\sim\partial/\partial t$ of the initial Eqs. (1) omitted (under condition of their smallness) in the derivation of solution (2), lead to transitions between the quantum states with various l'. Since all these states correspond to the same energy $E = -\hbar\omega_p$, the probability of transitions between these states $W_{12} = |f_{12}|^2$ can be calculated in the approximation of sudden perturbations [5]. On the other hand, for $s \gg 1$, we can use the quasi-classical approximation in which the matrix element f_{12} of the transition between the states with l_1' and l_2' is (to within the exponential explicitness)

$$f_{12} \sim \exp\left(-\frac{1}{\hbar}\text{Im}\left[\int^{r*}\sqrt{2m(E - U_1^{\text{ef}})}dr - \int^{r*}\sqrt{2m(E - U_2^{\text{ef}})}dr\right]\right),$$

$$U^{\text{ef}}(v) = U(v) + \hbar\omega_p\frac{v_0^2 - A^2}{v^2}. \tag{5}$$

Here, $r*$ are the singular points of $U^{\text{ef}}(r)$ or the roots of equation $U_1^{\text{ef}}(r) = U_2^{\text{ef}}(r)$ [5]. Among the two competitive points, $r_1^* = 0$ and $r_2^* = \infty$, we select that ensuring the minimum (in absolute value) exponent. In the case under consideration, both points make approximately equal contributions. For this reason, the consideration can be restricted to the point $r_2^* = \infty$, which eventually yields
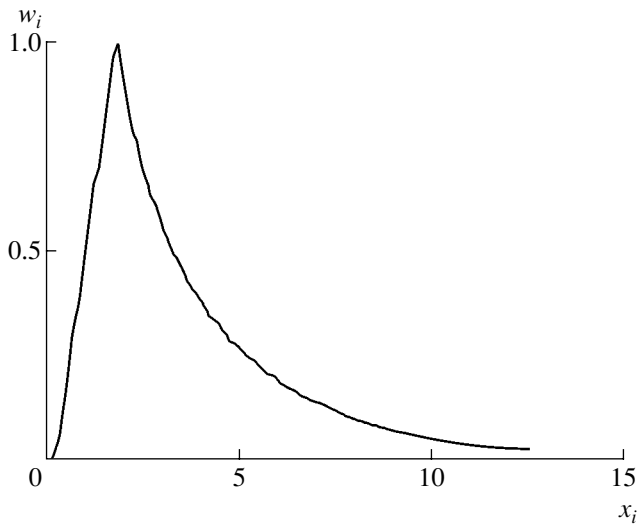
$$W_{12} \approx \exp\left(-\left|\frac{(l_1' + 1/2)^2 - (l_2' + 1/2)^2}{s}\right|\right)$$

$$= \exp\left(-\frac{|\Delta l'|(l_1' + l_2' + 1)}{s}\right), \tag{6}$$

where $\Delta l' = l_1' - l_2' = l_1 - l_2 = \Delta l$. Expression (6) was calculated using Langer's substitution $l'(l' + 1) \longrightarrow (l' + 1/2)^2$ [5].

Subsequent considerations employ the well-known uncertainty relation between Δl and $\Delta\chi$ [6]:

$$\frac{\Delta l\Delta\chi}{1 - \frac{3}{\pi^2}(\Delta\chi)^2} \geq \frac{1}{2}. \tag{7}$$

Since the unperturbed states are close to Gaussian wave packets, we can use this relation with a good approxi-

A plot of the relative probability $w(\Delta\Phi) = W/W_{max}$ versus length $\Delta\Phi$ of the laminar part of the unperturbed trajectory; $w_i = w(x_i)$, $x_i = \Delta\Phi$, and $1 \leq i \leq 200$.

mation as equality and set $\Delta l = [1/\Delta\chi - 3\Delta\chi/\pi^2]/2$. The final result depends on the relation between s and l. For small amplitudes of the classical solution ($l \sim s \gg 1$), we arrive at the following expression for $W_{12} = W(\Delta\Phi = \Delta\chi)$:

$$W(\Delta\Phi) \approx \exp\left(-\left|\frac{1}{\Delta\Phi} - \frac{3\Delta\Phi}{\pi^2}\right|\right). \qquad (8)$$

A curve of the relative (i.e., normalized to maximum) probability function $W(\Delta\Phi)$ is presented in the figure.

The phenomenon under consideration consists in a random change of the wave amplitude or, in terms of

the proposed model, of the parameter and eccentricity of the unperturbed trajectory (ellipse) on the "velocity–phase" plane (v, χ) under the action of a perturbation; $\Delta\chi$ is the length (in phase space) of the unperturbed (laminar) part of the trajectory. The fact that the Planck constant does not enter into Eq. (8) is indicative of the classical nature of this phenomenon. Coincidence with the well-known classical result [1] becomes even more evident if the trajectory is written as $s = s(\chi)$, where s is the distance measured from the perihelion along trajectory.

REFERENCES

1. P. Berge, Y. Pomeau, and C. Vidal, *Order Within Chaos: Towards a Deterministic Approach to Turbulence* (Wiley, New York, 1984; Mir, Moscow, 1991).

2. *Plasma Electrodynamics*, Ed. by A. I. Akhiezer (Nauka, Moscow, 1974; Pergamon, Oxford, 1975).

3. G. B. Whitham, *Linear and Nonlinear Waves* (Wiley, New York, 1974; Mir, Moscow, 1977).

4. R. Z. Sagdeev, D. A. Usikov, and G. M. Zaslavskiĭ, *Non-linear Physics: from the Pendulum to Turbulence and Chaos* (Nauka, Moscow, 1988; Harwood, Chur, 1988).

5. L. D. Landau and E. M. Lifshitz, *Course of Theoretical Physics*, Vol. 3: *Quantum Mechanics: Non-Relativistic Theory* (Nauka, Moscow, 1989, 4th ed.; Pergamon, New York, 1977, 3rd ed.).

6. A. I. Baz', Ya. B. Zel'dovich, and A. M. Perelomov, *Scattering, Reactions, and Decays in Nonrelativistic Quantum Mechanics* (Nauka, Moscow, 1971; Israel Program for Scientific Translations, Jerusalem, 1966).

7. L. D. Landau and E. M. Lifshitz, *Course of Theoretical Physics*, Vol. 1: *Mechanics* (Nauka, Moscow, 1982; Pergamon, New York, 1988).

Translated by P. Pozdeev

EPR Spectra and Relaxation Times
of Natural π-Conjugated Polymers Doped with Iodine

Yu. A. Lebedev*, L. A. Kosykh, A. N. Chuvyrov,
N. Ferrer-Anglada, and E. A. Mashkina

Institute of Molecular and Crystal Physics, Russian Academy of Sciences, Ufa, Bashkortostan, Russia
* e-mail: lebedev@anrb.ru
Received October 28, 2003; in final form, January 8, 2004

Abstract—The magnetic properties of natural π-conjugated polymers doped with iodine have been studied by EPR spectroscopy. It is established that an increase in the spin susceptibility upon doping is caused by the formation of π-electron radicals localized at the aromatic fragments of the polymer. Dependences of the spin–spin and spin–lattice relaxation times of these radicals on the doping level have been experimentally determined. © 2004 MAIK "Nauka/Interperiodica".

Natural π-conjugated polymers are usually obtained via high-temperature treatment of synthetic or natural organic compounds and resins, such as oils, coal tar, and some polymers [1]. Until recently, the products were mostly used for obtaining technical carbon, coke, and carbon fibers. However, there is ground for using π-conjugated polymers in electronics in view of their ability to generate and transfer electric charge [2, 3].

The main structural units of electrically active π-conjugated polymers are two-dimensional aromatic "molecules" having the form of clusters with dimensions on the order of 0.5–1.5 nm. The mechanism of charge carrier generation is related to the formation of donor–acceptor complexes. While many structural and molecular characteristics of these natural polymers are well known [1], their electron properties have not been studied in sufficient detail and the nature of charge carriers is not unambiguously established [2].

This study was aimed at elucidating the mechanisms of formation and determining the properties of charged centers in natural π-conjugated polymers doped with an electron acceptor—iodine. These goals were reached by using electron paramagnetic resonance (EPR) spectroscopy.

We have studied a polymer obtained from the most high-molecular asphaltene fraction of benzene pyrolysis tar [1], characterized by a high carbon content ([C] = 92.4%, [H] = 7.2%, C/H ≥ 1.25), a molecular weight of $M = 760$, and a softening temperature of 190°C. In the initial state, this substance appeared as a brown amorphous powder, possessing an electric resistivity of up to 10^{14} Ω cm. Iodine was introduced by means of cyclic doping from the vapor phase at a temperature of ~80°C [2].

The EPR spectra were measured on the standard X-band spectrometers RE-1306 (equipped with a low-temperature attachment for measurements in the 77–300 K range) and Varian 109 (equipped with an Oxford Instruments cryogenic attachment operating in the 5–300 K range). The integral intensities, line widths, and g values were referenced to the signal of 1,1'-diphenyl-2-picrylhydrazide (DPPH). The spin–spin and spin–lattice relaxation times of free radicals were determined by the saturation technique [4].

The EPR spectrum of the initial (undoped) polymer, like the spectra of most carbon-containing substances, displays a single symmetric line with an intensity corresponding to less than 1 spin per 10000 carbon atoms (Fig. 1). This singlet is situated at $g = 2.00275$ and has
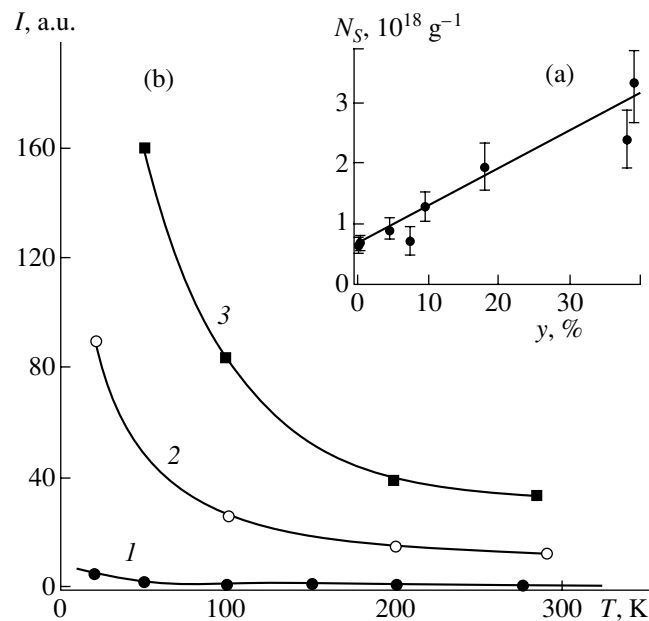

Fig. 1. Plots of (a) the concentration of paramagnetic centers N_S versus iodine doping level y and (b) the EPR signal intensity I versus temperature for a natural π-conjugated polymer with $y = 0$ (*1*), 9 (*2*), and (*3*) 39 mass %.

P = 0.25 mW

0.1

0.05

0.025

0.01

0.005

1

4

10

25

100 mW

(a)

I_{pp}, a.u.

(b)

H_1

100

1

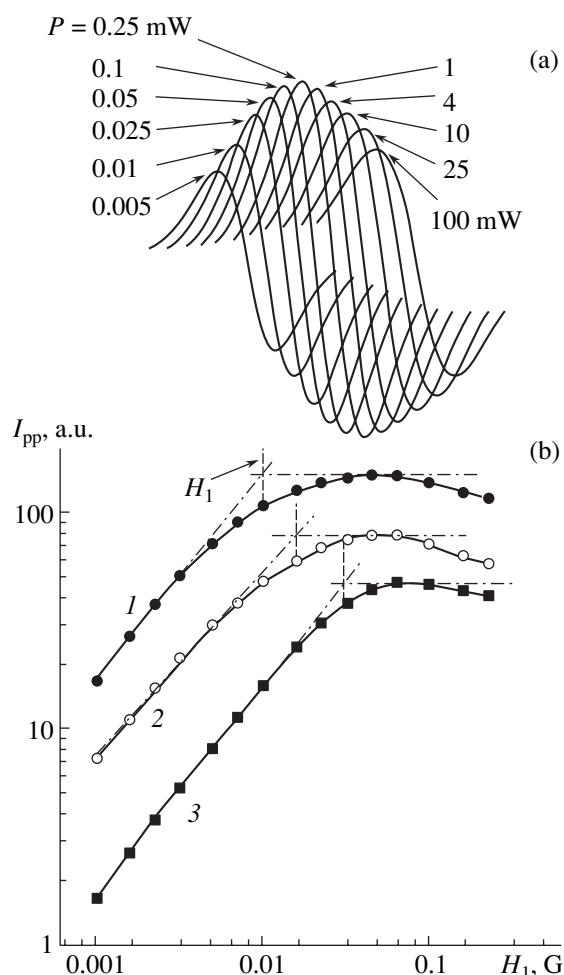*2*

10

3

1

0.001   0.01   0.1 H_1, G

Fig. 2. (a) Variation of the shape of the EPR spectrum depending on the microwave power P and (b) saturation of the EPR signal intensity I_{pp} with increasing microwave field strength $H_1 \sim \sqrt{P}$ for an iodine-doped natural π-conjugated polymer with $y = $ (*1*) 0, (*2*) 9, and (*3*) 39 mass %.

a peak-to-peak width of $\Delta H_{pp} = 9.5$ G. It should be noted that both width and intensity of the EPR signal of the initial polymer may significantly vary from one sample to another, depending on the method of synthesis and conditions of preparation. The values of ΔH_{pp}

EPR characteristics of ion-doped natural π-conjugated polymers

Iodine content y, mass %	Spin density N_S, spin/g	Line width ΔH_{pp}, G	T_2, s	T_1, s
0	6.4×10^{17}	9.56	7.0×10^{-7}	4.9×10^{-5}
9	1.3×10^{18}	8.82	3.6×10^{-7}	4.4×10^{-5}
18	1.9×10^{18}	8.19	3.5×10^{-7}	1.4×10^{-5}
39	3.4×10^{18}	8.13	1.7×10^{-7}	1.6×10^{-5}

are scattered within 7–10 G and the intensities may vary by a factor of two to three, but the behavior of these parameters as dependent on the temperature and the level of doping is identical in all samples.

Both the line width and the g value of the initial signal are virtually independent of the temperature in the range 77–300 K, while the temperature dependence of the EPR signal intensity in the first approximation obeys the Curie law: $I \sim C/T$ (Fig. 1a). The nature of this signal is commonly accepted as well established, being attributed to unpaired π electrons delocalized over polyaromatic fragments of the polymer with a small degree of condensation (C/H $\geq$ 1) [5]. These very π electrons account for the singlet line with a g value close to that of the free electron (2.0023) and the π radicals in the linear π-conjugated polymer *trans*-polyacetylene (2.00263). It is believed that the main mechanism responsible for the formation of these paramagnetic centers is inter- or intramolecular electron transfer at the sites of impurity localization or structural defects [6].

As the microwave power pumped to the spin system increases, the EPR signal from such π radicals exhibits saturation at a power of $P \sim 1$ mW. The line width and shape remain virtually unchanged, which is evidence of inhomogeneous line broadening. The typical behavior of the EPR signal in response to the microwave power variation is illustrated in Fig. 2.

Doping of the initial polymer with iodine leads to a significant modification of its physicochemical properties. The samples acquire metal luster and their conductivity increases by several orders of magnitude, while the density of unpaired electrons increases by only one order (Fig. 1a). The resonance line remains symmetric and its intensity varies with the temperature according to the Curie law (Fig. 1b). The g value also increases (up to 2.0033) with the iodine content, while the line width decreases to almost 8 G (see table). Apparently, the halogen atoms interacting with unpaired electrons are capable of more effectively transferring energy from the spin system to surrounding lattice. As a result, saturation of the EPR signal is more difficult to attain (Fig. 2b). The spin–lattice (T_1) and spin–spin (T_2) relaxation times determined from the saturation curves (Fig. 2b) for the initial and iodine-doped polymers are given in the table.

As can be seen from data in the table, the relaxation times are on the order of $T_1 \sim 10^{-5}$ s and $T_2 \sim 10^{-7}$ s, which is quite typical of such materials [6]. For comparison, T_2 values in the linear π-conjugated *trans*-polyacetylene and graphite amount to 0.78×10^{-7} and 0.20×10^{-7} s, respectively [7]. In these polymers, as well as in analogous strongly diluted paramagnets, $T_1 \gg T_2$ and T_2^{-1} is proportional to the density N_S of unpaired electrons. The characteristic time T_1 of the spin-lattice relaxation varies from 4.9×10^{-5} s in the initial polymer to $\sim 1.5 \times 10^{-5}$ s in iodine-doped samples. The latter value is determined by the change in vibra-

tional modes of the molecular cluster in the presence of an iodine-induced charge. This is related to an increase in the fraction of aromatic radical cations appearing upon the formation of charge-transfer complexes between the aromatic fragments (electron donors) and iodine atoms (electron acceptors).

Apparently, there are several mechanisms responsible for the observed behavior of T_1. The first is related to a decrease in the molecular mobility of aromatic clusters bound in a complex, which is caused by the heavy iodine atom. The second mechanism is related to the removal of degeneracy in the electron system of conjugated π bonds of the aromatic molecular clusters upon ionization. This leads to a change in the parameters of the electron–phonon interaction responsible for the spin–lattice relaxation and is manifested, for example, by amplification of the nonactive IR modes of C–C vibrations, which are rendered active due to asymmetry arising in the electron system [8].

Thus, the formation of charge transfer complexes between an electron acceptor (iodine) and the aromatic clusters of a natural π-conjugated polymer in the course of halogenation is accompanied by (i) an increase in the density of π electron radicals in proportion to the doping level and (ii) a decrease in the spin–spin and spin–lattice relaxation times of these radicals.

REFERENCES

1. A. S. Fialkov, *Carbon, Interface Connections and Composites on Their Basis* (Aspekt, Moscow, 1997).
2. A. N. Chuvyrov, Yu. A. Lebedev, and L. A. Kosykh, Pis'ma Zh. Tekh. Fiz. **20** (19), 45 (1994) [Tech. Phys. Lett. **20**, 785 (1994)].
3. S. Yata, Y. Hato, H. Kinoshita, *et al.*, Synth. Met. **73**, 273 (1995).
4. A. M. Portis, Phys. Rev. **91**, 1071 (1953); T. G. Castner, Phys. Rev. **115**, 1506 (1959).
5. I. C. Lewis, Carbon **20**, 519 (1982).
6. L. A. Blyumenfel'd, V. A. Benderskiĭ, L. S. Lyubchenko, and P. A. Stunzhas, Zh. Strukt. Khim. **8**, 829 (1967).
7. J. C. W. Chien, G. E. Wnek, F. E. Karasz, *et al.*, Macromolecules **15**, 614 (1982).
8. Yu. A. Lebedev, A. N. Chuvyrov, L. A. Kosykh, *et al.*, Khim. Tverd. Topliva **4**, 88 (2003).

Translated by P. Pozdeev

The Effect of Hydrogen on the Electric Conductivity of Tin Oxide Doped with Yttrium

I. V. Zolotukhin, Yu. E. Kalinin*, O. I. Samokhina, and A. V. Sitnikov

Voronezh State Technical University, Voronezh, Russia
* e-mail: kalinin@ns1.vstu.ac.ru
Received January 22, 2004

Abstract—Amorphous films of tin oxide doped with yttrium were obtained by ion beam sputter deposition. After crystallization, the films acquired a nanocrystalline structure. The introduction of yttrium leads to an increase in the crystallization temperature of tin oxide. The electric conductivity of films containing yttrium in excess of 1 at. % is highly sensitive to hydrogen. Nanocrystalline films of tin oxide doped with yttrium may serve as hydrogen-sensitive media. © *2004 MAIK "Nauka/Interperiodica".*

In recent years, in view of increasing interest in molecular hydrogen as an alternative organic fuel, there has been a search for the base materials for hydrogen sensors capable of operating both in vacuum and in the usual atmosphere. Hydrogen and other gases (CH_4, CO, CO_2, NH_3, etc.) are usually detected using palladium-activated tin oxides, the sensitivity of which increases if the material has a nanocrystalline structure [1–3]. The activation of oxides is related to an increase in the surface energy of grain boundaries, the fraction of which significantly increases for a grain size within 10–20 nm [4].

One of the main problems encountered in the use of such materials is instability of their properties caused by the growth of grains at elevated temperatures corresponding to the maximum sensitivity of gas sensors. In order to obtain structures with a small grain size and acceptable stability, films of tin oxide are doped with various elements capable of stabilizing the nanocrystalline structure [5].

This Letter presents data on the effect of molecular hydrogen on the resistivity ρ of nanocrystalline films of the Sn–O–Y system. Nanocrystalline films of tin oxide stabilized with yttrium were obtained by ion beam sputter deposition on glassceramic (sitall) substrates [6].

The composite targets comprised high-purity tin (99.98 at. % Sn) plates with dimensions 280 × 80 × 0.5 mm bearing 80 × 10 × 1-mm yttrium plates. The latter plates were arranged on tin surface at a variable step so as to obtain 1- to 1.5-μm-thick films with the indium content continuously varying from 0.4 to 5 at. % along the substrate. The ion beam sputtering process was carried out in an atmosphere comprising a mixture of 40% Ar and 60% O_2 at a total pressure of 7×10^{-4} Torr. The composition of a deposit was determined by electron-probe X-ray microanalysis at five sites in various regions of the film. The phase composition of the film could vary depending on the arrangement of yttrium plates in the composite target. Variation of the composition along the substrate was described using polynomial extrapolation. We have studied six samples differing by the content of yttrium (see table). The resistivity was determined potentiometrically with an error not exceeding 1–2%.

In the initial state, films of all compositions were amorphous and possessed very high room-temperature resistivities (ρ ≈ 10^{10} Ω cm) and very low sensitivity with respect to hydrogen. As the temperature was increased to the crystallization temperature, the resistivity decreased. The crystallization temperature T_c was determined by the onset of a sharp change in the sample resistivity in the course of the transition from amorphous to crystalline state. The lowest transition temperature (T_c ≈ 500°C) was observed for a film with the composition $Sn_{59.8}O_{39.8}Y_{0.4}$ (containing the minimum amount of yttrium). As the yttrium concentration c was increased from 0.4 to 2.2 at. %, the T_c value increased from 500 to 630°C (see table). Higher concentrations of yttrium ($c > 2.2$ at. %) did not lead to further increase in the crystallization temperature.

The effect of yttrium on the crystallization temperature of tin oxide films grown by ion beam sputter deposition

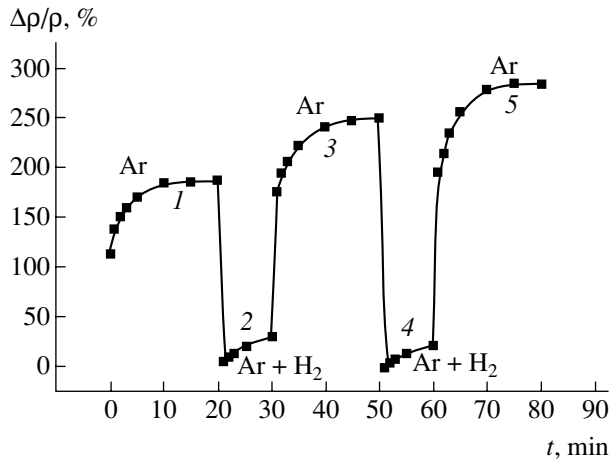| Sample no.	Film composition			Crystallization temperature, °C
	Sn, at. %	O, at. %	Y, at. %	
1	59.8	39.8	0.4	500
2	50.4	48.6	1.0	530
3	49.7	49.2	1.1	550
4	48.9	49.9	1.2	580
5	48.4	49.4	2.2	630
6	48.3	46.9	4.8	630

Fig. 1. Time variation of the resistivity of a $Sn_{48.4}O_{49.4}Y_{2.2}$ film in the course of isothermal annealing at $T = 350°C$: (*1*) admission of argon ($P = 380$ Torr); (*2, 4*) adding molecular hydrogen ($P = 7.6$ Torr) to argon at $P = 372.4$ Torr; (*3, 5*) repeated admission of argon ($P = 380$ Torr) after evacuation of the chamber.

Fig. 2. Time variation of the resistivity of a $Sn_{48.4}O_{49.4}Y_{2.2}$ film in the course of isothermal annealing at $T = 350°C$: (*1*) admission of air ($P = 380$ Torr); (*2, 4*) adding molecular hydrogen ($P = 7.6$ Torr) to air at $P = 372.4$ Torr; (*3, 5*) repeated admission of argon ($P = 380$ Torr) after evacuation of the chamber.

In order to reduce ρ and transform the structure from amorphous into nanocrystalline, the samples were heated at a rate of 4 K/min up to a temperature of $T_c + 20°C$. This was followed by a short annealing (not exceeding 5 min) at this temperature and cooling in argon at a pressure of $P = 380$ Torr. After this heat treatment, the samples were studied with respect to the effect of hydrogen on the electric properties of nanocrystalline tin oxide doped with yttrium.

Figure 1 shows the pattern of variation of the relative change in the resistivity ($\Delta\rho/\rho = (\rho - \rho_{min})/\rho_{min}$, where ρ_{min} is the minimum value of resistivity at a given temperature) of a $Sn_{48.4}O_{49.4}Y_{2.2}$ film in the course of isothermal annealing at $T = 350°C$ and cyclic admission of argon (regions *1*, *3*, and *5*) and hydrogen (regions *2* and *4*). The admission of argon into the vacuum chamber with a residual pressure of $P = 10^{-4}$ Torr leads to a 70–75% increase in ρ during the 20-min exposure (Fig. 1, regions *1*, *3*, and *5*). Adding hydrogen at a partial pressure of $P = 7.6$ Torr to the argon atmosphere leads to a sharp (150–175% within less than one minute) drop in the resistivity (Fig. 1, regions *2* and *4*). The evacuation of the chamber and admission of argon restores ρ in a jumplike manner approximately to the initial level before the drop. Multiply repeated (seven times or more), these cycles of gas admission and pumping reveal virtually completely reproduced variation of the sample resistivity under the action of hydrogen and argon.

Analogous features in the curve of $\Delta\rho/\rho$ were observed when molecular hydrogen was admitted on the background of air. As can be seen from Fig. 2, the isothermal annealing of a $Sn_{48.4}O_{49.4}Y_{2.2}$ film at $T = 350°C$ in air with cyclic admission of hydrogen is also accompanied by jumps in the relative resistivity incre-
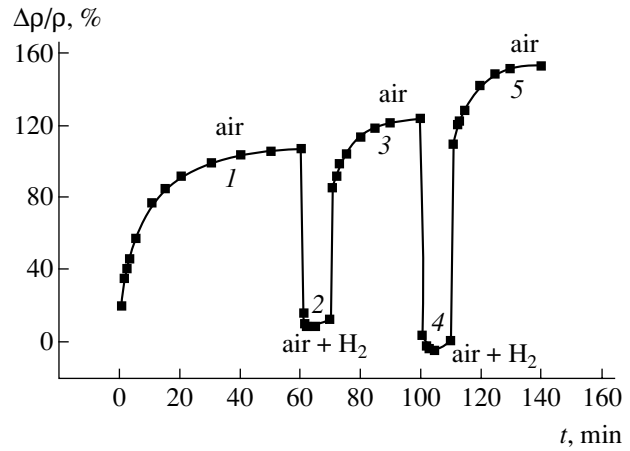
ment, although the jump amplitude is somewhat lower (95–100%) than in the case of argon.

The most striking sensitivity to hydrogen was observed for a film with the composition $Sn_{48.9}O_{49.9}Y_{1.2}$ in the course of annealing in air at $T = 350°C$ (Fig. 3). In this case, air almost completely stabilized the resistivity ρ, which varied only within 25–50% (see regions *1*, *3*, and *5* in Fig. 3). The admission of hydrogen at a partial pressure of $P = 7.6$ Torr leads to a very sharp (within several seconds) and large (700–800%) drop in the resistivity (Fig. 3, regions *2* and *4*), while the evac-
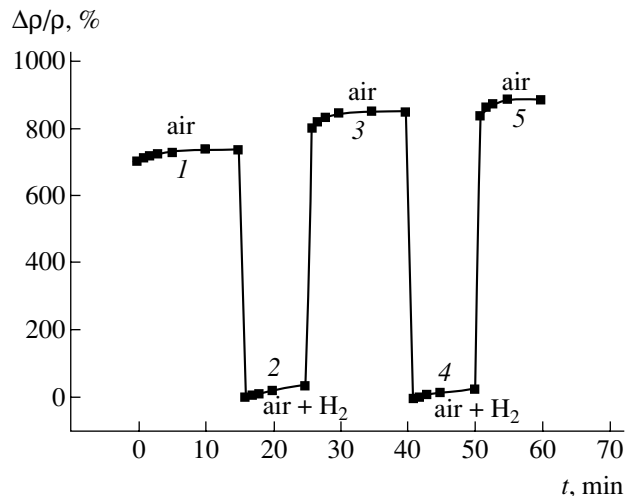

Fig. 3. Time variation of the resistivity of a $Sn_{48.9}O_{49.9}Y_{1.2}$ film in the course of isothermal annealing at $T = 350°C$: (*1*) admission of air ($P = 380$ Torr); (*2, 4*) adding molecular hydrogen ($P = 7.6$ Torr) to air at $P = 372.4$ Torr; (*3, 5*) repeated admission of air ($P = 380$ Torr) after evacuation of the chamber.

uation of hydrogen restores the sample resistivity to the initial level.

Let us consider the results. The electron-microscopic examination of the structure of samples upon crystallization showed that the films containing yttrium in excess of 1 at. % acquire a nanocrystalline structure with a grain size of 10–30 nm and, hence, are characterized by a developed surface of grain boundaries. According to [4], the relative volume of a grain-boundary phase is

$$\frac{\Delta V}{V} = \left[\frac{\pi}{6}d^3 - \frac{\pi}{6}(d - 2\delta)^3\right]\left(\frac{\pi}{6}d^3\right)^{-1} \cong \frac{6\delta}{d},$$

where d is the grain size and δ is the thickness of the grain-boundary layer (phase interface).

Taking into account that the crystal lattice parameters of most SnO modifications fall within 0.5–0.6 nm, it would be quite reasonable to suggest that the thicknesses of grain-boundary layers and phase interfaces are on the same order of magnitude. Let us evaluate the relative volume occupied by the grain-boundary phase in films with the maximum and minimum grain size. In the former case ($d = 30$ nm, $\delta = 0.5$ nm), we obtain $\Delta V/V = 10\%$, and in the latter case ($d = 10$ nm, $\delta = 0.5$ nm), $\Delta V/V = 30\%$. These estimates show that yttrium not only produces a catalytic action but also provides for the formation of a nanocrystalline structure (yttrium atoms play the role of crystallization centers).

In order to explain the observed variations in the electric conductivity of yttrium-doped tin oxide in contact with gas phases of various compositions, we proceed from the electron theory of chemisorption and catalysis based on the notion of surface electron states in semiconductors [7]. According to this, the gas molecules adsorbed on the oxide surface can either give their electrons to or take the electrons from the oxide, thus behaving as the electron donors or acceptors, respectively. Since yttrium-doped tin oxide is a semiconductor of the *n* type, the adsorption of acceptor molecules creates near-surface regions depleted of electrons and leads to a decrease in the electric conductivity. This is consistent with the effects of argon and air observed in our experiments. On the contrary, the adsorption of donor molecules on the *n*-type oxide leads to the formation of a subsurface region enriched with electrons. This leads to an increase in the electric conductivity, in agreement with the effect observed for hydrogen.

Thus, thin films of tin oxide doped with yttrium possess a nanocrystalline structure with a grain size of 10–30 nm. The introduction of yttrium in an amount of 1–4 at. % sharply increases the sensitivity of tin oxide with respect to hydrogen. Nanocrystalline films of yttrium-doped tin oxide can be used as sensitive media for hydrogen sensors operating in argon and air.

REFERENCES

1. A. M. Gas'kov and M. N. Rumyantseva, Neorg. Mater., No. 3, 369 (2000).
2. D. Kohl, J. Phys. D: Appl. Phys. **34**, R125 (2001).
3. L. A. Bashkirov, U. Barbi, Yu. K. Gun'ko, *et al.*, *Topical Problems of the Physics of Solids* (Belaruskaya Navuka, Minsk, 2003), pp. 146–162.
4. A. I. Gusev, Usp. Fiz. Nauk **168**, 55 (1998) [Phys. Usp. **41**, 49 (1998)].
5. N. P. Maksimova, Yu. G. Kataev, and E. V. Chernikov, Zh. Fiz. Khim. **71**, 1492 (1997).
6. Yu. N. Kalinin, A. T. Ponomarenko, A. V. Sitnikov, and O. V. Stogneĭ, Fiz. Khim. Obrab. Mater., No. 5, 14 (2001).
7. V. L. Bonch-Bruevich and S. G. Kalashnikov, *Physics of Semiconductors* (Nauka, Moscow, 1977).

Translated by P. Pozdeev

Acoustic Channels and Lenses in a Medium with Inhomogeneous Velocity Field

N. N. Rozanov*, [1] and G. B. Sochilin

Institute of Laser Physics, St. Petersburg, Russia
*e-mail: rosanov@ilph.spb.su
Received November 25, 2003

Abstract—A homogeneous moving medium can feature waveguide propagation of acoustic oscillations, provided that the velocity of medium is inhomogeneous. A waveguide of a finite length is equivalent to a lens. The waveguides and lenses are nonreciprocal, whereby their characteristics are significantly different for the acoustic waves propagating in opposite directions. Estimates are obtained and the possible applications are discussed. © 2004 MAIK "Nauka/Interperiodica".

In stratified water with the temperature and hydrostatic pressure varying in the vertical direction, a layer characterized by a minimum sound velocity may occur at a certain depth. This layer may serve as a waveguide or underwater channel for acoustic waves. Under natural conditions, sound may travel via such a channel through a distance of several hundred and thousand kilometers [1].

This Letter presents an alternative mechanism of the waveguide propagation and focusing of sound that can be operative even in a nonstratified medium, whereby the sound velocity is constant and independent of the coordinates. Instead, the medium (liquid) moves at a velocity exhibiting an extremum (maximum or minimum) at some axis. Then, the effective velocity of sound entrained by the moving medium [2] will also be maximum or minimum at this axis, thus providing conditions for the waveguide propagation. This phenomenon is an acoustic analogue of the variant of optical waveguides and lenses based on the Fresnel–Fizeau effect of the partial light entrainment in a transparent medium with inhomogeneous velocity proposed in our recent paper [3].

In a medium moving at a velocity **u**, the dispersion relation between the frequency ω and the wavevector **k** of a plane monochromatic wave has the following form [2]:

$$\omega = c_s k + \mathbf{u}\mathbf{k}. \quad (1)$$

Here, c_s is the velocity of sound (considered as constant) in a motionless medium. Assuming that the velocity of the medium is much smaller than the sound velocity ($|u| \ll c_s$) and the considering parallel (or antiparallel) motions of the medium and the acoustic wave,

---

[1] The author has also appeared under the alternate spelling N.N. Rosanov.

we obtain an expression for the wavenumber,

$$k = \frac{\omega}{c_s + u} \approx k_0\left(1 - \frac{u}{c_s}\right) = k_0 n_{\text{ef}}, \quad k_0 = \frac{\omega}{c_s}, \quad (2)$$

where the optical analogy is emphasized by introducing the effective refractive index

$$n_{\text{ef}} = 1 - \frac{u}{c_s}. \quad (3)$$

The velocity u is positive or negative when the medium and wave move in the same or opposite directions, respectively.

Let us consider a laminar horizontal motion of the liquid medium along the z axis with a maximum velocity at some axis of the stream (the case of minimum velocity is analogous). Near this axis, the velocity u is a quadratic function of the distance from the axis:

$$u = u_0\left(1 - \frac{x^2}{a_x^2} - \frac{y^2}{a_y^2}\right). \quad (4)$$

Here, u_0 is the velocity of liquid motion on the axis and $a_{x,y}$ are the characteristic stream widths in the transverse directions x and y (in the general case, these values are different). We consider a paraxial region in which the distance from the axis in Eq. (4) is relatively small:

$$x^2 \ll a_x^2, \quad y^2 \ll a_y^2. \quad (5)$$

In these terms, the effective refractive index can be represented as

$$n_{\text{ef}}(y) = n_0 - \frac{1}{2}n_x y^2 - \frac{1}{2}n_y y^2, \quad (6)$$

$$n_0 = 1 - \frac{u_0}{c_s}, \quad n_x = -2\frac{u_0}{c_s a_x^2}, \quad n_y = -2\frac{u_0}{c_s a_y^2}. \quad (7)$$

Relation (6) corresponds to the well-known case of quadratic optical medium (see, e.g., [4]). A necessary condition for the waveguide propagation of sound consists in that the liquid and sound should move in the opposite directions, so that $u_0 < 0$. If the stream widths $a_{x, y}$, are constant (independent of z), an astigmatic waveguide appears in the liquid. In the paraxial approximation (5), the waveguide modes are represented by the Gaussian acoustic beams. The lowest mode widths are

$$w_x^2 = \frac{2}{k_0 \sqrt{n_0 n_x}}, \quad w_y^2 = \frac{2}{k_0 \sqrt{n_0 n_y}}. \quad (8)$$

The condition of validity of this description, $w_{x, y}^2 \ll a_{x, y}^2$, implies the requirement that the stream width must be sufficiently large as compared to the sound wavelength $\Lambda = 2\pi/k_0$:

$$\frac{a_{x, y}}{\Lambda} \gg \frac{1}{2\pi} \sqrt{\frac{c_s}{|u_0|}}. \quad (9)$$

For $|u_0| = 1$m/s and $c_s = 1.5 \times 10^3$ m/s, the right-hand side of this inequality is approximately equal to six. Note that the waveguide under consideration is nonreciprocal: it holds only the acoustic pressure directed oppositely to the liquid flow, while the cocurrent acoustic waves exhibit scattering.

The waveguide effect is realized in the flow (stream) with a constant (or slowly varying) width over a length L exceeding the characteristic diffraction length of a beam with the halfwidth w:

$$L \gg L_d = k_0 w^2. \quad (10)$$

The reverse inequality implies that a short region of the stream is equivalent to an astigmatic lens with the focal distances

$$f_{x, y} = \frac{1}{n_{x, y} L}. \quad (11)$$

The lens is also nonreciprocal: the focus sign alters when the direction of the acoustic wave changes to opposite. The focal distance decreases with increasing flow velocity. However, the requirement of laminar (or the absence of developed turbulence) restricts the possibility of increasing the wave velocity, since the Reynolds number (in a liquid with the kinematic viscosity ν_m),

$$\text{Re} = \frac{|u_0| w_{x, y}}{\nu_m}, \quad (12)$$

must not exceed a certain critical value Re_{cr} [2].

Under natural conditions, the transverse flow dimensions in water may reach several hundred meters, while the distance of the acoustic beam propagation is limited by the absorption and scattering of sound in water, amounting to 15–20 km for frequencies within 500–2000 Hz. In the general case of a stream in a stratified liquid medium, the traditional [1] and proposed mechanisms of waveguide propagation and focusing may operate jointly. An important sign of the presence of a contribution due to the proposed mechanism related to inhomogeneity of the velocity of liquid is the difference in the conditions of sound propagation in the opposite directions. For artificial flows in round tubes, a quadratic dependence of the flow velocity on the transverse coordinates (3) corresponds to an exact solution of the equations of hydrodynamics [2]. In the experiments with thoroughly eliminated perturbations at the tube entrance, the motion remains laminar up to $\text{Re} \sim 10^5$ [2]. Nonreciprocal acoustic waveguides and lenses can be used, for example, for decoupling high-power sound and ultrasound radiators from the action of opposite (reflected) radiation.

REFERENCES

1. L. M. Brekhovskikh, *Waves in Layered Media* (Nauka, Moscow, 1973; Academic, New York, 1980).

2. L. D. Landau and E. M. Lifshitz, *Fluid Mechanics,* 2nd ed. (Nauka, Moscow, 1986; Pergamon Press, Oxford, 1987).

3. N. N. Rozanov, G. B. Sochilin, and O. B. Danilov, Opt. Spektrosk. **95**, 908 (2003) [Opt. Spectrosc. **95**, 849 (2003)].

4. D. Marcuse, *Light Transmission Optics* (Van Nostrand, New York, 1972; Mir, Moscow, 1974).

Translated by P. Pozdeev

Copper-Containing Nanocomposites: Synthesis and Phase Composition

K. V. Zapsis, A. S. Dzhumaliev, N. M. Ushakov*, and I. D. Kosobudskiĭ

Saratov State Technical University, Saratov, Russia

Saratov Branch, Institute of Radio Engineering and Electronics, Russian Academy of Sciences, Saratov, Russia

* e-mail: nmu@mail.saratov.ru

Received October 22, 2003; in final form, January 22, 2004

Abstract—Composites comprising copper nanoparticles dispersed in a low-density polyethylene matrix were obtained by thermal decomposition of copper diacetate. The powdered nanocomposite was studied by X-ray diffraction. The phase composition of nanoparticles depends on the metal content in the matrix. The average size of nanoparticles determined from the characteristic broadening of diffraction peaks falls within 10–25 nm. © 2004 MAIK "Nauka/Interperiodica".

The so-called ultradisperse media still receive much attention. Of special interest are new composite materials with elements possessing a nanostructural morphology. Possessing unique properties, such ultradisperse materials based on metal-containing polymers are finding increasing application in radio engineering and optoelectronics as magnetic [1–3], conducting [4, 5], and optical media [6–8]. Depending on the degree of filling of the dielectric matrix with metal (e.g., iron) nanoparticles, metal–polymer nanocomposites exhibit a broad spectrum of electrical and optical properties, in particular, with manifestations of quantum confinement effects [9, 10]. From the standpoint of electric conductivity, most interesting are copper-containing nanocomposites, the properties of which still remain almost unstudied.

This study was devoted to obtaining new composites based on low-density polyethylene (LDPE) containing dispersed nanoparticles of copper and to studying their chemical phase composition.

The copper-containing nanocomposites were synthesized by the well-known method [1–3]. Thermal decomposition of the initial copper diacetate monohydrate ($(CH_3COO)_2Cu \cdot H_2O$) was carried out at $T = 250 \pm 5°C$ in a polymer medium. The resulting LDPE–Cu nanocomposites were obtained in the form of powders with a copper content of 3, 10, 20, and 40 wt %.

The phase composition of the synthesized LDPE–Cu powders was studied by standard X-ray diffraction methods. The measurements were performed on a DRON-4 diffractometer using CoK_α radiation. The average particle size was determined using the Debye–Scherrer formula [11, 12]

$$D = 0.94\lambda/B\cos\theta,$$

where λ is the X-ray wavelength, θ is the Bragg diffraction angle, and B is the diffraction peak broadening. The B value was calculated using the Warren formula [11],

$$B^2 = B_s^2 - B_0^2,$$

where B_s is the peak half-width in the sample diffractogram and B_0 is that for a reference compound (pure Cu–Cu_2O powder without LDPE) with a particle size no smaller than 100 nm.

Published data [1–3, 13] on the phase composition of iron nanoparticles in polyethylene matrices (obtained using analogous methods) show that the pure metal phase is never formed in the polymer medium. At a small metal content (1–10 wt %), the metal phase is supplemented by an oxide phase, while the composites with large metal concentrations (20–50 wt %) contain an additional carbide phase. The content of the pure metal phase varies in the course of storage in air. This behavior is explained by a high chemical activity of iron-containing nanoparticles and the permeability of polyethylene for oxygen and other gases. As is known [11–13], most ultradisperse media possess X-ray amorphous structures. However, it was pointed out [14] that sharp peaks observed on the X-ray diffractograms allow the phase composition of samples to be determined, provided that the size of structural elements is greater than 10 nm.

The X-ray diffraction patterns of our samples with small copper content (LDPE–3 wt % Cu) exhibited strongly smeared diffraction lines without clear maxima. However, the positions of the two clear maxima at $2\theta = 42.55$ and $50.73°$ allows us to assign these peaks to copper(I) oxide (Cu_2O) and metallic copper (Cu). On the whole, the strongly broadened character of diffraction maxima is indicative that the material with such a small metal content is X-ray amorphous and the size of dispersed objects does not exceed 10 nm.

An increase in the metal content to 10 wt % leads to the appearance of all the diffraction peaks characteristic
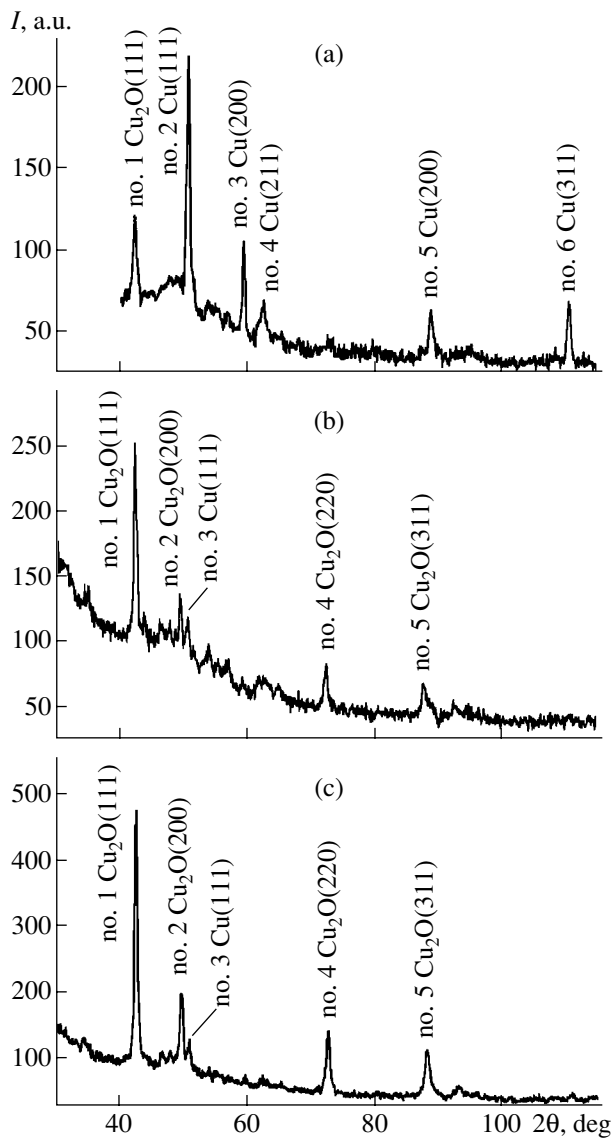
Fig. 1. X-ray diffractograms of copper-containing nano-composites: (a) LDPE–10 wt % Cu; (b) LDPE–20 wt % Cu; (c) LDPE–40 wt % Cu.

of copper. Figure 1a shows the diffractograms with the peaks assigned to metallic copper: no. 2, d_{hkl} = 2.085, (111); no. 3, d_{hkl} = 1.803, (200); no. 4, d_{hkl} = 1.735, (211); no. 5, d_{hkl} = 1.277, (220); and no. 6, d_{hkl} = 1.087, (311). Peak no. 1 (d_{hkl} = 2.484, (111)) can be assigned to Cu_2O because the surface of copper aggregates frequently contains Cu(I) oxide fragments. This is related to the formation of so-called peach structure [10], whereby the metal phase is concentrated inside an aggregate (particle) and is coated with the oxide shell.

Further increase in the metal content up 20 wt % (Fig. 1b) and 40 wt % (Fig. 1c) leads to the appearance of additional peaks characteristic of Cu_2O, while the peaks characteristic of copper disappear (except for a low-intensity peak at $2\theta = 50.80°$), which is consistent with the above considerations. The diffraction peaks

corresponded to the following interplanar spacings d_{hkl}. LDPE–20 wt % Cu: no. 1, d_{hkl} = 2.479, (111); no. 2, d_{hkl} = 2.144, (200); no. 4, d_{hkl} = 1.513, (220); no. 5, d_{hkl} = 1.290, (311); LDPE–40 wt % Cu: no. 1, d_{hkl} = 2.462, (111); no. 2, d_{hkl} = 2.131, (200); no. 4, d_{hkl} = 1.509, (220); no. 5, d_{hkl} = 1.285, (311).

The average particle size D calculated from data on the characteristic broadening of diffraction peaks for the samples containing 10, 20, and 40 wt % copper was $D_1 = 11 \pm 2$ nm (LDPE–10 wt % Cu), $D_2 = 14 \pm 2$ nm (LDPE–20 wt % Cu), and $D_3 = 24 \pm 2$ nm (LDPE–40 wt % Cu).

In conclusion, we have synthesized new copper-containing nanocomposites and studied their chemical phase composition. Based on the X-ray diffraction data, the average size of nanoparticles was determined for various metal concentrations in the polymer matrix. As the copper content increases from 3 to 40 wt %, the average size of nanoparticles reaches 24 ± 2 nm. The thickness of the copper(I) oxide layer also grows, so that no peaks of metallic copper are found in the diffractogram of LDPE–40 wt % Cu samples.

REFERENCES

1. S. P. Gubin, V. V. Odintsov, V. A. Shargatov, and V. I. Pepekin, Dokl. Akad. Nauk SSSR **260**, 655 (1981) [Sov. Phys. Dokl. **26**, 1069 (1981)].

2. I. D. Kosobudskiĭ, Vysokomol. Soedin., Ser. A **27**, 689 (1985).

3. A. V. Kozinkin *et al.*, Izv. Ross. Akad. Nauk, Neorg. Mater. **30**, 678 (1994).

4. V. V. Kislov, V. V. Kolesov, and I. V. Taranov, Radiotekh. Élektron. (Moscow) **47**, 1385 (2002).

5. L. I. Trakhtenberg, G. N. Gerasimov, V. K. Potapov, *et al.*, Vestn. Mosk. Univ., Ser. 2: Khim. **42**, 325 (2001).

6. S. Kummel, K. Andrae, and P.-G. Reinhard, Appl. Phys. B **73**, 293 (2001).

7. S. R. Sershen, S. L. Westcott, J. L. West, and N. J. Halas, Appl. Phys. B **73**, 379 (2001).

8. N. Del Fatti and F. Vallee, Appl. Phys. B **73**, 383 (2001).

9. N. M. Ushakov, K. V. Zapsis, and I. D. Kosobudskiĭ, Pis'ma Zh. Tekh. Fiz. **29** (22), 29 (2003) [Tech. Phys. Lett. **29**, 936 (2003)].

10. N. M. Ushakov, V. I. Kochubeĭ, K. V. Zapsis, and I. D. Kosobudskiĭ, Opt. Spektrosk. (2004) (in press).

11. I. D. Morokhov, L. I. Trusov, and V. N. Lapovok, *Physical Phenomena in Ultradisperse Media* (Énergoatomizdat, Moscow, 1984).

12. L. M. Kovba and V. K. Trunov, *X-ray Phase Analysis* (MGU, Moscow, 1976).

13. I. D. Kosobudskiĭ, V. P. Sevost'yanov, and G. Yu. Yurkov, Izv. Vyssh. Uchebn. Zaved., Khim. Khim. Tekhnol. **43** (1), 135 (2000).

14. G. Yu. Yurkov, A. V. Kozinkin, T. I. Nedoseĭkina, *et al.*, Izv. Ross. Akad. Nauk, Neorg. Mater., No. 11 (2001).

Translated by P. Pozdeev

Experimental Study of the Concentration Dependence of the Real Part of Permittivity in a Paraffin–Graphite Disordered Macrosystem

V. A. Sotskov

Kabardino-Balkarian State University, Nalchik, Kabardino-Balkaria, Russia
e-mail: sozkov_va@rambler.ru
Received October 16, 2003; in final form, January 8, 2004

Abstract—The experimentally determined real part of permittivity in a paraffin–graphite macrosystem exhibits a monotonic dependence on the concentration of the conducting component. © *2004 MAIK "Nauka/Interperiodica"*.

In recent years, much attention has been devoted to investigations of the electrical properties of nanocomposites, including macrosystems of the insulator–conductor type [1]. These materials exhibit sharp changes in the conductivity, temperature coefficient of resistance, and other electrical characteristics in the region of percolation transition. This makes it possible to obtain materials possessing substantially different properties even within the framework of the same technology [1–5], using small variations in the content of one of the system components. The anomalous behavior of the real part ε' of the complex permittivity can be of considerable significance for the development of new capacitors intended for micro- and nanoelectronic devices. However, experimental investigations of the dependence of ε' on concentration, $\varepsilon' = f(x)$, for model macroscopic insulator–conductor type systems with a view to analysis of the processes on a microscopic level are still very seldom [1–7].

This Letter reports on the results of experimental investigation of the real part of the dielectric permittivity of a paraffin–graphite macrosystem as a function of the bulk content of the conducting component.

The behavior of the real part of the permittivity was studied in a paraffin–graphite system modeling macroscopic disordered systems of the insulator–semiconductor type. The choice of this model system was exhaustively justified elsewhere [8]. Each sample had the form of a capacitor cell, comprising a solidified paraffin–graphite mixture of a certain concentration confined between electrodes made of electrolytic copper. The capacitance and Q values of the capacitor were determined by conventional methods at a frequency of 1 kHz. The measurements were performed with allowance of the capacitance of connecting leads and the edge capacitance [10].

The real part ε' of the sample permittivity was determined as the ratio [9, 11]

$$\varepsilon' = \frac{C_x}{C_0}, \qquad (1)$$

where C_0 is the capacitance of the empty (air-filled) cell [10] and C_x is the capacitance of the cell filled with a paraffin–graphite mixture with the concentration x of the conducting component. The typical semilogarithmic experimental plot of the real part of the permittivity versus concentration of the conducting phase, $\log \varepsilon' = f(x)$, is presented in the figure (curve *1*). As can be seen from this plot, $\log \varepsilon' = f(x)$ is a monotonically increasing function with a final ε' value of about 170×10^6. In the concentration range studied, the value of ε' increases by a factor of 4×10^7. Previously [8], we thoroughly studied the resistivity of paraffin–graphite composites with variable bulk concentration of the conducting phase and determined the percolation threshold and some other parameters of this system. Since the system under consideration in this study is the same, some data for the calculations were also taken from [8].

The theoretical curve of $\varepsilon' = f(x)$ (see figure, curve *2*) for $\omega = 0$ is described by the relation [3]

$$\varepsilon'(0, x) = \frac{\varepsilon'_0}{|x - x_c|^q}, \qquad (2)$$

where $\varepsilon'_0 = 2.1$ [12] and $q = t\left(\frac{1}{s} - 1\right)$; for $x_c = 0.16$ [8],

$s = \frac{1}{2}$ [3], and $t = 1.4$ [8], we obtain $q = 1.4$. As can be seen in the figure, curve *2* has two branches—left-hand ($x < x_c$) and right-hand ($x > x_c$)—and exhibits a singularity at $x = x_c$. If the frequency ω is nonzero, the theoretical curve differs from curve *2* (for $\omega = 0$) in the fig-
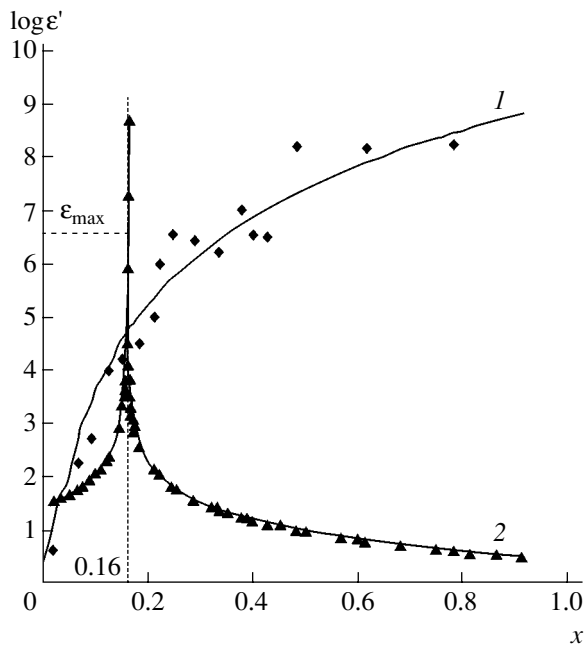
Semilogarithmic plots of the real part of the permittivity versus bulk content of the conducting phase in a paraffin–graphite macrosystem: (*1*) experiment; (*2*) theory [2].

However, we can still notice that the experimental curve in the range of $x > x_c$ differs from theoretical: the former exhibits a growth and is a logical continuation of the experimental behavior in the region of $x \leq x_c$. Thus, based on the experimental facts, we have to ascertain that the dependence $\log\varepsilon' = f(x)$ has a monotonically increasing character. No evidence of a singularity in the region of the percolation threshold was experimentally observed for the real part of the permittivity of a three-dimensional paraffin–graphite macrosystem. The increase in ε' in composites was interpreted [1] as reflecting the increase in the area of contact between conducting and dielectric phases in the course of decrease in the thickness of dielectric interlayers. However, this interpretation referred to the region of $x < x_c$. The author of this study believes that, in real systems, the growth has to continue for $x \geq x_c$ because the properties of the composite tend to those of the conductor. The experimental data reported in [6, 7] were obtained for the metal–dielectric junctions in *n*-type silicon [6] and for the island films [7]. The difference between the results obtained in the present study and the for substantially two-dimensional systems studied in [4, 6, 7] is probably explained by the spatial-dimensional effects [1].

ure in that the singularity is replaced by a maximum at $x = x_c$, while the behavior of the left- and right-hand branches remains the same. The magnitude of this maximum, ε'_{max}, for sufficiently low frequencies $(4\pi\sigma_D^0/\varepsilon_0' \gg \omega)$ can be estimated by the formula $\varepsilon'_{max} = \varepsilon_0'\left(\dfrac{\sigma_M}{\sigma_D}\right)^{1-S}$ [3] or $\varepsilon'_{max} = \varepsilon_0'\left(\dfrac{\rho_D}{\rho_M}\right)^{1-S}$. For the insulator (paraffin) and conductor (carbon) resistivities $\rho_D = 10^{10.5}$ Ω m and $\rho_M = 4.1 \times 10^{-2}$ Ω m [8], respectively, this formula yields $\varepsilon'_{max} = 3.25 \times 10^{6.25}$ (or $\log\varepsilon'_{max} \approx 6.8$).

Note that the theoretical curve *2* in the figure has a small interval between branches. For example, estimation using formula (2) on a level of $\log\varepsilon'_{max} \approx 6.8$ yields the peak width $\Delta x \approx 5 \times 10^{-5}$. In the region of intersection of the experimental and theoretical curves, $\log\varepsilon' \approx 4.5$ and $\Delta x \approx 1.2 \times 10^{-4}$. The sample mixture components were weighed with an accuracy within $\Delta x \approx 1.2 \times 10^{-4}$ at $x_c = 0.16$ (a total of 50 samples were prepared for $x = x_c$). Assuming that, by virtue of stochastic processes involved in the sample preparation (stirring, casting, cooling), no one sample fell within the interval corresponding to the above interval between the two branches on the level of $\log\varepsilon' \approx 4.5$, we can explain the absence of a peak in the experimental curve *1* and the difference by two orders of magnitude between the experimental and theoretical curves at $x = x_c$.

REFERENCES

1. E. V. Kharitonov, *Dielectric Materials with Heterogeneous Structure* (Radio i Svyaz', Moscow, 1983).

2. I. A. Chmutin, S. V. Letyagin, V. G. Shevchenko, and A. T. Ponomarenko, Vysokomol. Soedin. **36**, 699 (1994).

3. A. L. Efros and B. I. Shklovskii, Phys. Status Solidi B **76**, 475 (1976).

4. V. E. Dubrov, M. E. Levinshteĭn, and M. S. Shur, Zh. Éksp. Teor. Fiz. **5**, 2014 (1976) [Sov. Phys. JETP **43**, 1050 (1976)].

5. V. L. Bonch-Bruevich, Vestn. Mosk. Univ., No. 5, 550 (1975).

6. T. G. Gastner, N. K. Lee, G. S. Cieloszyk, and G. L. Salinger, Phys. Rev. Lett. **34**, 1627 (1975).

7. R. H. Ritchie, Surf. Sci. **1**, 34 (1973).

8. V. A. Sotskov and S. V. Karpenko, Zh. Tekh. Fiz. **73**, 107 (2003) [Tech. Phys. **48**, 100 (2003)].

9. V. V. Pasynkov, *Materials of Electronic Technology* (Vysshaya Shkola, Moscow, 1980), pp. 155–160.

10. *Dielectric Materials and Applications*, Ed. by A. R. von Hippel (Wiley, New York, 1954; Inostrannaya Literatura, Moscow, 1960).

11. V. P. Berzan *et al.*, *A Handbook: Electric Capacitors* (Shtiintsa, Kishinev, 1982), p. 27.

12. *Tables of Physical Data: Reference Book*, Ed. by I. K. Kikoin (Atomizdat, Moscow, 1976).

Translated by P. Pozdeev

Solution of the Inverse Problem of X-ray Diffraction on Periodic InGaN/GaN/Al$_2$O$_3$ Nanostructures

A. G. Krasil'nikov, V. I. Punegov*, and N. N. Faleev**

Syktyvkar State University, Syktyvkar, Komi Republic, Russia
** Present affiliation: Rigaku MSC, 9009 New Trails Drive, The Woodlands, TX 77381-5209, USA
* e-mail: punegov@syktsu.ru
Received January 8, 2004

Abstract—The inverse problem of X-ray diffraction on two samples of Al$_2$O$_3$(0001)–GaN–(In$_{0.03}$GaN–In$_{0.1}$GaN)$_{x5SL}$–AlGaN(20 nm) superlattices grown using close technological regimes was numerically solved with allowance for both coherent and diffuse scattering. Detailed profiles of the strain, composition, and defect density in depth of the multilayer structures were obtained, which makes it possible to analyze the process of epitaxial growth and defect formation in mismatched domain heterostructures. Peculiarities of the X-ray diffraction on such structures are considered. It is shown that, in the case of strongly mismatched solid solutions, similarity of the growth procedures does not ensure the formation of nanodimensional periodic systems with identical structural parameters. © *2004 MAIK "Nauka/Interperiodica".*

Beginning with pioneering investigations [1–6], the extraction of information about structural characteristics of the surface layers of crystals and heterostructures from the X-ray diffraction patterns is among the currently important problems in the physics of condensed state. Despite the large number of publications on this subject (see, e.g, [7] and references therein), there is no commonly accepted approach to solution of the inverse problem of the X-ray diffractometry.

Previously [8, 9], we originally used both coherent and diffuse components of diffracted radiation for determining the structural parameters of multilayer laser heterostructures and graded-index heteroepitaxial layers. The results of such analysis provided important additional information concerning the process of epitaxial growth and defect formation in matched heterostructures. However, there were no attempts at solving the inverse problem of X-ray diffraction with allowance for the diffuse scattering for multilayer mosaic heterostructures with superlattices. This paper reports on the results of solving such a problem for periodic InGaN/GaN/Al$_2$O$_3$ nanostructures.

Two samples of α-Al$_2$O$_3$(0001)–GaN–(In$_{0.03}$GaN–In$_{0.1}$GaN)$_{x5SL}$–AlGaN(20 nm) were grown by metalorganic chemical vapor deposition (MOCVD) under close conditions on sapphire substrates with a thick (2−4 μm) buffer GaN layer. The X-ray diffraction measurements were performed at the State University of Nagoya (Japan) on a high-resolution double-crystal Rigaku diffractometer with 18-kW rotating anode. The conventional X-ray rocking curves and two-dimensional reciprocal space maps (RSMs) were measured using Cu$K_{\alpha 1}$ radiation in the vicinity of GaN(0002) reflection. The coherent and diffuse components of the

scattering intensity were separated using narrow slits in front of the detector.

The numerical algorithm of solution of the inverse diffraction problem was based on expressions for the coherent and diffuse components of the scattering intensity in the kinematic approximation [11]. The incoherent (diffuse) component was calculated using the model of a mosaic crystal [11]. In contrast to [8, 9], where the inverse diffraction problem was solved using double- and triple-crystal spectra recorded in the ϑ–2ϑ scan mode, we extracted information from the X-ray rocking curves and isodiffuse lines. The rocking curves were measured with a significantly better resolution.

The computational procedure employed the method of minimization of the functional of variance for the coherent and diffuse components of the scattering intensity,

$$F[\varepsilon(z), f(z), r(z)] = \sum_i \left| \log\left(\frac{I_i^{\text{exp}}}{I^{\text{th}}}\right)^2 \right|, \qquad (1)$$

in terms of the criterion χ^2 [12]

$$\chi^2 = \frac{1}{n - n_P}\sum_{i=0}^{n} \frac{\log^2(I_i^{\text{exp}}/I_i^{\text{th}})}{s_i^2}. \qquad (2)$$

Here, I^{exp} and I^{th} are the experimental and theoretical angular distributions of the scattering intensity, respectively; $\varepsilon(z) = \Delta d/d$ is the relative strain of the crystal lattice with respect to the GaN lattice period; $f(z)$ is the effective scattering ability equal to the product of the static Debye–Waller factor and the normalized struc-
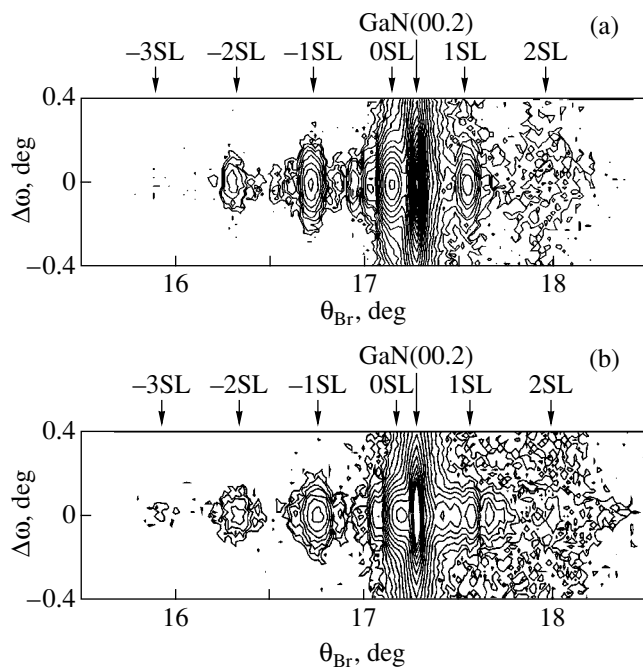
Fig. 1. RSMs showing the spatial distribution of radiation diffracted from samples (a) 1 and (b) 2 in the vicinity of GaN(0002) reflection (Cu$K_{\alpha 1}$ radiation).

tural factor of a sample; and $r(z)$ is the domain size profile in depth of the mosaic structure. In the expression for criterion χ^2, n is the number of points in the X-ray rocking curve or in the RSM, n_p is the number of parameters, and s_i is the normalization factor depending on the uncertainty of initial data. Minimization of functional (1) was performed using the method of sliding descent, which makes it possible to introduce variable conditions for the structural parameters [13].

In order to extract information about the strain profile, effective scattering ability, and the vertical (l_z) and lateral (l_x) dimensions of domains in the mosaic structure, the superlattices (SLs) were considered as N-layer planar systems. After solving the problem of minimization of functional (1) for the initial approximation ($N = 15$, $\varepsilon(z) = $ const, $f(z) = $ const), each layer was split into halves to obtain the initial approximation for the repeated solution of the minimization problem with a doubled number of layers ($N = 30$).

The angular distribution of intensity in the experimental RSMs uniquely corresponds to a mosaic structure of epitaxial layers (Fig. 1). The elongation of the superstructural bands in the direction of $\Delta\omega(q_x)$ is related to misorientation of the crystalline domains. For GaN layers, the average domain size in the direction of epitaxial growth, as estimated from the correlation length of the mosaic structure model, was ~165–175 nm. For SLs, this parameter was ~53–55 nm, which is close to the total thickness of these layers. The lateral dimensions of domains in the GaN layer and SLs, as esti-

mated from the full width at half maximum (FWHM) of the ω curves, was ~100–115 nm. The boundaries of domains were formed by the accumulations of threading dislocations, the density of which in the upper part of the GaN layer and SLs was estimated at $(7–10) \times 10^8$ cm^{-2}.

Despite the domain structure of epitaxial layers, the intensity of the diffuse-scattered X-ray radiation component was relatively small. For this reason, the RSMs reveal, together with superstructural diffraction peaks, clear reflections due to the thickness oscillations. The interference patterns extended in the 2θ–ω direction are indicative of a relatively high (for a mosaic heterostructure) flatness of the epitaxial layers (see [10]). Estimates showed that the roughness (smearing) of interfaces in SLs was ~2.0–2.2 nm.

Figures 2 and 3 show (a) the experimental and theoretical X-ray rocking curves, (b) the calculated depth profiles of relative strain of the crystal lattice, and (c) the depth profiles of effective scattering ability. Data on the structural characteristics were obtained for an SL model with $N = 30$. In the lattice strain and scattering ability profiles, the depth is measured from the interface between the upper protective cap layer (AlGaN) and SL. The presence of the protective layer was taken into account, but the adopted model did not allow for structural changes in this layer.

Apart from some local distinctions between the X-ray rocking curves, the profiles observed for two samples are very close (cf. Figs. 2a and 3a). The average superstructural period was determined using the distance between satellite peaks. In the cases under consideration, the SL periods are approximately equal and amount to 11 ± 1 nm. The average relative strain was $\bar{\varepsilon}_1 = 1.2 \times 10^{-3}$ for sample 1 and $\bar{\varepsilon}_2 = 0.6 \times 10^{-3}$ for sample 2. The difference is explained by a decrease in the content of In in the superlattice. This change led to a decrease in the level of elastic stresses in the epitaxial layers and, accordingly, in the degree of relaxation, and it eventually resulted in an increase in the Debye–Waller factor for the second sample.

A decrease in the strain as a result of the relaxation of elastic stresses might led to the formation of defects not taken into account in the numerical solution of the inverse problem. This circumstance may probably explain the local differences between experimental and theoretical rocking curves for the second sample.

In both samples, significant violations of the structural perfection are observed at interfaces between the buffer GaN layer and SLs and between the SLs and the upper 20-nm-thick protective AlGaN layer. In sample 1, partial relaxation of the elastic stresses led to the formation of extended defects at the center of the periodic structure. Nevertheless, the average values of the static Debye–Waller factor are 0.6 for both samples, which is slightly smaller that the value observed for a thin (0.3 μm) planar GaN layer grown on a SiC(0001) substrate [10].
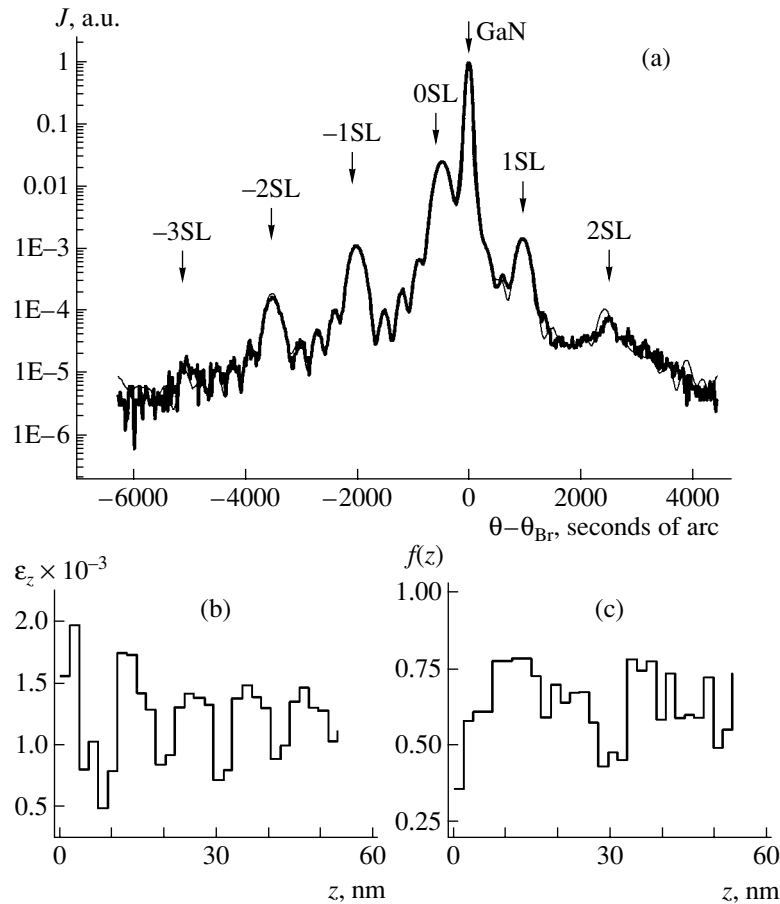
Fig. 2. Sample 1: (a) experimental (thick line) and theoretical (thin line) rocking curves in the vicinity of GaN(0002) reflection (Cu$K_{\alpha 1}$ radiation); (b) strain–depth profile (higher strain corresponds to a greater content of In in epitaxial layers); (c) static Debye–Waller factor profile.

The relatively high density of dislocations observed in the samples studied implies that the structures were grown under the conditions of significant deviations from stoichiometry, which is typical of the growth of III-N heterostructures. During the epitaxial growth of nitrides, nonstoichiometry is one of the main factors leading to structural imperfections and accounting for the appearance of a vast number of point defects on the growth surface with the subsequent transformation into extended defects.

Under normal conditions, the role of local concentrators of elastic stresses and point defects in heterostructures is played by nonplanar interfaces (planar defectless interfaces only slightly retain the diffusing point defects [14]). For this reason, nonplanar interfaces are the sites where the accumulated point defects transform into clusters, dislocations, and dislocation accumulations. In thick layers of nitrides (with thicknesses greater than the length of thermoactivated diffusion of the point defects), the role of such centers is played by the accumulations of threading dislocations (domain walls), at which the intrinsic strain fields are formed and the point defects are concentrated.

The introduction of additional interfaces (e.g., SLs) into heterostructures leads to the redistribution of point defects from the threading dislocations and dislocation walls toward these interfaces and, eventually, to the formation of misfit dislocations (MDs). Owing to their nature, MDs do not form accumulations (similar to domain walls formed by threading dislocations) and exhibit more or less uniform distribution at the interfaces and/or in the bulk of epitaxial layers. This leads to violation of the planar character of interfaces and the growth surface, which decreases the coherence length of diffracted radiation, gives rise to diffuse scattering, and eventually decreases the Debye–Waller factor of the given structure.

We believe that MDs are responsible for the imperfections observed at the interfaces and in the bulk of structures under consideration. However, the total number of MDs formed at the interfaces was insufficient for making the interfaces substantially nonplanar and producing effective extinction of the X-ray diffraction. Note that, in contrast to the formation of MDs, the trapping of excess point defects by threading dislocations and an increase in the density of such dislocations
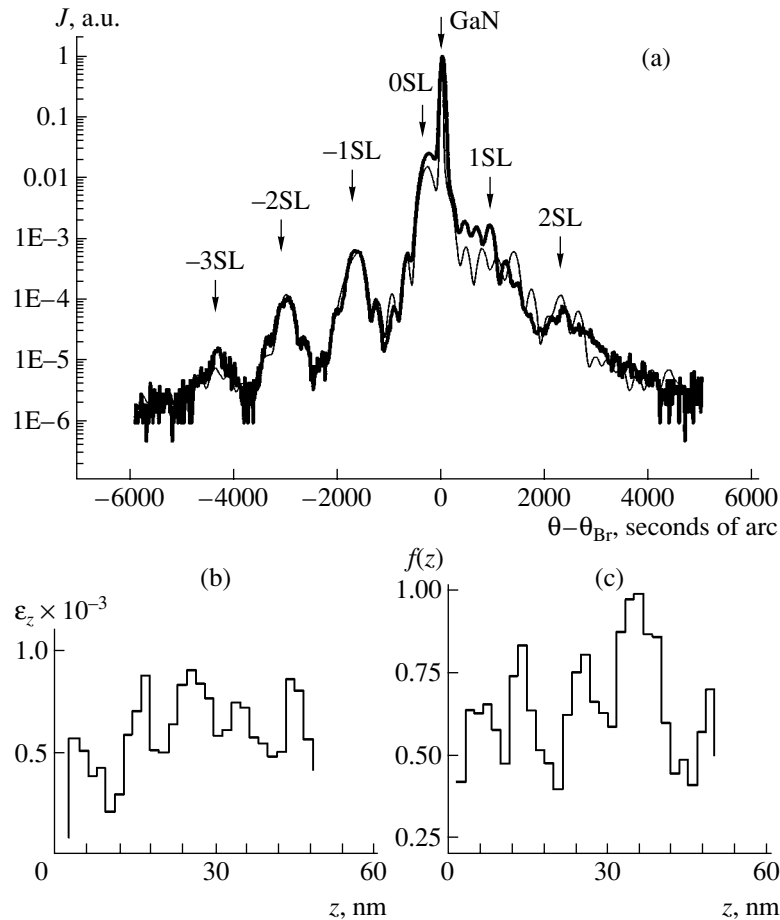
Fig. 3. Sample 2: (a) experimental (thick line) and theoretical (thin line) rocking curves in the vicinity of GaN(0002) reflection (Cu$K_{\alpha 1}$ radiation); (b) strain–depth profile (higher strain corresponds to a greater content of In in epitaxial layers); (c) static Debye–Waller factor profile.

improves the structural perfection of epitaxial layers and leads to an increase in the Debye–Waller factor [10].

Thus, we have demonstrated that solution of the inverse problem of X-ray diffraction with allowance for diffuse scattering in multilayer domain heterostructures makes it possible to obtain detailed depth profiles of the strain, composition, and defect density in such systems. Using these data, it is possible to analyze the process of epitaxial growth and defect formation in such structures characterized by a high density of crystalline defects. No such data can be provided by other, nondiffraction methods. The proposed method can reveal the differences in structural parameters even between the samples grown using close technological regimes. It was shown that, in the case of strongly mismatched solid solutions, similarity of the growth procedures does not ensure the formation of nanodimensional periodic systems with identical structural parameters.

The results of our investigation showed that the accumulations of threading dislocations (domain walls) do not significantly contribute to the diffuse X-ray scattering. It was confirmed that the main centers responsi-

ble for such scattering are the edge dislocations and related structural distortions rather than the point defects (primarily because of their small dimensions), as was suggested previously [10]. MDs account for violation of the planar character of interfaces and for excess roughness of the growth surface.

REFERENCES

1. J. Burget and D. Taupin, Acta Crystallogr., Sect. A **24**, 99 (1968).

2. J. Burget and R. Collela, J. Appl. Phys. **40**, 3505 (1969).

3. A. Fukuhara and Y. Takano, Acta Crystallogr., Sect. A **33**, 137 (1977).

4. A. M. Afanasev, M. V. Kovalchuk, E. K. Kovev, and V. G. Kohn, Phys. Status Solidi A **42**, 415 (1977).

5. R. N. Kyutt, P. V. Petrashen', and L. M. Sorokin, Phys. Status Solidi A **60**, 381 (1980).

6. B. C. Larson and J. F. Barhorst, J. Appl. Phys. **51**, 3181 (1980).

7. A. V. Goncharskiǐ, A. V. Kolpakov, and A. A. Stepanov, *Inverse Problems of X-ray Diffractometry* (Latv. Univ., Riga, 1992).

8. K. M. Pavlov, V. I. Punegov, and N. N. Faleev, Zh. Éksp. Teor. Fiz. **107**, 1967 (1995) [JETP **80**, 1090 (1995)].

9. V. I. Punegov, K. M. Pavlov, S. G. Podorov, and N. N. Faleev, Fiz. Tverd. Tela (St. Petersburg) **38**, 264 (1996) [Phys. Solid State **38**, 148 (1996)].

10. A. Kazimirov, N. Faleev, H. Temkin, *et al.*, J. Appl. Phys. **89**, 6092 (2001).

11. Ya. I. Nesterets and V. I. Punegov, Acta Crystallogr., Sect. A **56**, 540 (2000).

12. A. M. Afanas'ev, M. A. Chuev, R. M. Imamov, *et al.*, Kristallografiya **42**, 514 (1997) [Crystallogr. Rep. **42**, 467 (1997)].

13. D. M. Himmelblau, *Applied Nonlinear Programming* (McGraw-Hill, New York, 1972; Mir, Moscow, 1975).

14. N. N. Faleev, L. I. Flaks, S. V. Batashova, *et al.*, in *Proceedings of the All-Union Conference on Physical Processes in Heterostructures, Kaluga, 1990*, Vol. 1, p. 241.

Translated by P. Pozdeev

Electrical Properties
of Metal–Dysprosium Oxide–Gadolinium Oxide–Silicon Structures

V. A. Rozhkov* and M. A. Rodionov

Samara State University, Samara, Russia
* *e-mail: rozhkov@ssu.samara.ru*
Received November 3, 2003; in final form, December 28, 2003

Abstract—We have studied the electrical properties of aluminum–dysprosium oxide–gadolinium oxide–silicon (Al–Dy_2O_3–Gd_2O_3–Si) structures. The conductivity of these metal–insulator–semiconductor (MIS) structures is satisfactorily described by the Poole–Frenkel mechanism. The density of surface states determined by the method of capacitance–voltage characteristics is 5.6×10^{11} cm^{-2}. The surface generation rate and lifetime of the minority charge carriers determined using the Zerbst method fall within 47–67 cm/s and 0.3–0.6 μs, respectively. The structures studied are promising materials for MIS varactors with a high capacity variation coefficient. © *2004 MAIK "Nauka/Interperiodica".*

The development of modern microelectronics stimulates continuous search for the new insulating materials. Promising dielectric materials suitable for the formation of insulating layers are offered by rare earth element (REE) oxides. These compounds are characterized by high chemical and thermal stability, large permittivities ($\varepsilon = 8$–20) and resistivities ($\rho = 10^{13}$–10^{16} Ω cm), and good adhesion to the silicon surface. Metal–insulator–semiconductor (MIS) structures employing REE oxides were used for the development of varactors and photovaractors [1], MIS transistors [2], electrical and thermal switches [3], and effective thermostable antireflection and passivating coatings for photoelectric devices [4].

Despite a large number of publications, the properties of REE oxide films and related MIS structures are still insufficiently studied. There are many questions related to the mechanisms of processes occurring on the surface and in the space charge region of a semiconductor and there are problems in the search for and development of new insulator–semiconductor systems. In this context, we have studied the electrical properties of silicon-based MIS structures with two-layer insulating films made of REE oxides. Using two-layer insulating films (in particular, REE oxide–SiO_2 and Si_3N_4–SiO_2), it is possible to increase the electrical stability of MIS devices.

The substrates were cut from (111)- and (100)-oriented single crystal silicon wafers of the KEF-5 and KDB-4.5 grades, respectively. The films of rare earth metals on the silicon substrates were formed by thermal deposition in vacuum. The metals were evaporated from molybdenum crucibles in a residual vacuum of

$(2$–3$) \times 10^{-5}$ Torr (VUP-5 vacuum system). Each substrate surface was sequentially coated with gadolinium and dysprosium. Then, the two-layer films were oxidized in a tubular muffle furnace (SUOL-0.4.4) in air for 40 min at 500–520°C. The thickness of each REE oxide layer in the structures studied was 350–400 Å. The ohmic contacts on the insulator surface were formed by vacuum deposition of aluminum pads via masks. The electrode area was 2.7×10^{-3} cm^2. The opposite surface of the silicon substrate was coated with a continuous aluminum film.

The dc current–voltage characteristics of the sample MIS structures are virtually symmetric and the conductivity of samples is satisfactorily described by the Poole–Frenkel mechanism implying field-assisted thermoactivated electron injection from the bulk traps to the conduction band. The rectification coefficients of various samples fall within 1.1–2. The resistivities of the two-layer REE oxide films determined from the dc current–voltage characteristics amount to 10^{12}–10^{14} Ω cm.

The properties of semiconductor–insulator interfaces in the MIS structures were studied by measuring their high-frequency capacitance–voltage (C–U) characteristics. Figure 1 shows the typical C–U curves of the Al–Dy_2O_3–Gd_2O_3–Si system (normalized to the insulator capacitance) in comparison with the theoretical characteristics calculated for the ideal structures [5]. As can be seen, the experimental curves are shifted relative to the ideal characteristics toward negative voltages. This is evidence of the presence of a positive built-in charge in the insulator and at the semiconductor–insulator interface, which is typical of thermally grown oxide films [6]. The surface density Q_{ss} of the

built-in charge in the insulator determined assuming flat bands on the semiconductor surface was 8.9×10^{-8} C/cm². The density of surface states in the samples studied amounted to 5.6×10^{11} cm⁻², and the capacity variation coefficient $K = C_{max}/C_{min}$ varied within 8–12 (C_{max} and C_{min} are the maximum and minimum values of the insulator capacitance).

The results of measurements of the dielectric loss tangent $\tan \delta$ as a function of the applied high-frequency (1 MHz) voltage U showed that these curves exhibit a maximum at the flat-band voltage and show a tendency to saturation in the region of voltage amplitudes corresponding to the accumulation and inversion layer at the semiconductor surface. The active conductivity component G smoothly increases on the passage from depletion to enrichment voltages and exhibits saturation in the region of voltage amplitudes corresponding to the accumulation and inversion. The values of conductivity and loss tangent in the region of voltages corresponding to accumulation were greater than in the region corresponding to inversion.

In the case of accumulation, the semiconductor surface exhibits a certain decrease in the loss tangent as compared to that for the state of flat bands. This behavior is related to the fact that, on the passage from flatband to accumulation voltage, the reactive component of the conductivity decreases faster than the active component. No such decrease is observed in the dependence of G on U. This is evidence of the relatively low density of fast surface states at the semiconductor–insulator interface. The values of conductivity of the sample structures determined for various applied voltages vary from 0.0028 to 0.72 mS. The dielectric loss tangent varies within 0.018–0.381.

For determining the rate of surface generation and the lifetime of minority carriers, we measured the kinetics curves $C(t)$ for the semiconductor surface depleted of the majority carriers. The state of depletion was induced by application of rectangular voltage pulses [7]. Figure 2 shows the typical $C(t)$ oscillograms measured at room temperature in the dark for the MIS structure Al–Dy₂O₃–Gd₂O₃–n-Si biased by various voltages. The application of a pulsed voltage corresponding to depletion led to a rapid decrease in the capacitance of the MIS structure (related to an increase in thickness of the space charge region), followed by an increase to the equilibrium value. The increase in the capacitance with time is explained by the thermal generation of electron–hole pairs in the space charge region and at the semiconductor surface, followed by their separation in the electric field. As a result, the minority carriers accumulate at the surface to form the inversion layer, while the majority carriers drift to the boundary of the depleted region and neutralize the ionized impurity centers. This leads to a decrease in the
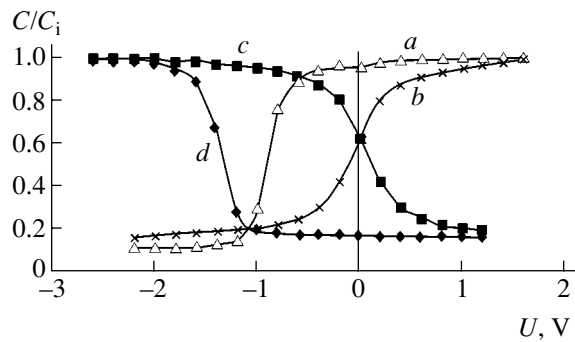

Fig. 1. Typical capacitance–voltage characteristics (normalized to the insulator capacitance C_i) of the (a, b) Al–Dy₂O₃–Gd₂O₃–n-Si and (c, d) Al–Dy₂O₃–Gd₂O₃–p-Si structures: (a, d) experiment; (b, c) theoretical characteristics calculated for the ideal systems.
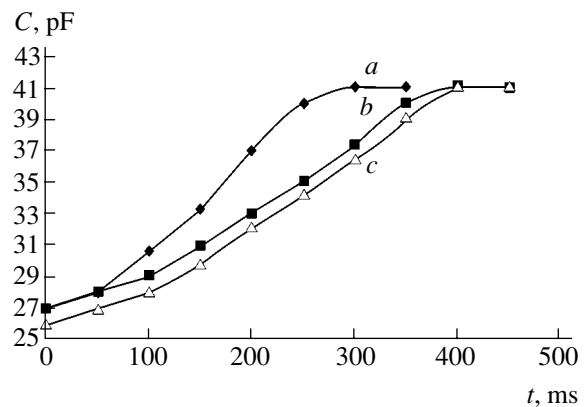
Fig. 2. Room-temperature kinetics of the capacitance of the Al–Dy₂O₃–Gd₂O₃–n-Si structure measured using 3-V rectangular pulses in the dark at various bias voltages (V): (a) 2; (b) 4; (c) 6.

thickness of the depleted region and an increase in the capacitance.

The bulk lifetime τ and the surface generation rate S of the minority charge carriers were calculated using the Zerbst method [7]. According to this, the $C(t)$ curve is replotted in the Zerbst coordinates to acquire the form of straight lines. The slope of this line determines the bulk lifetime of minority carriers, while the intercept with the ordinate axis determines their surface generation rate. For the MIS structures studied, the S and τ values fell within 47–67 cm/s and 0.3–0.6 µs, respectively.

Thus, the results of our investigation indicate that the MIS structures studied are characterized by high capacity variation coefficients and good insulating properties, thus showing good prospects for use in MIS varactors. High quality of the semiconductor–insulator interface in these structures suggests that the REE oxides studied can be used as passivating layers in

semiconductor devices, in particular, as the gate insulators in MISFET transistors.

REFERENCES

1. V. A. Rozhkov, A. Yu. Trusova, I. G. Berezhnoĭ, and V. G. Goncharov, Zh. Tekh. Fiz. **65** (8), 183 (1995) [Tech. Phys. **40**, 849 (1995)].

2. U. Guttierets, Zarubezhn. Radioélektron., No. 1, 86 (1966).

3. V. A. Rozhkov and A. I. Petrov, Pis'ma Zh. Tekh. Fiz. **11** (1), 49 (1985) [Sov. Tech. Phys. Lett. **11**, 21 (1985)].

4. Yu. A. Anoshin, A. I. Petrov, V. A. Rozhkov, *et al.*, Pis'ma Zh. Tekh. Fiz. **18** (10), 54 (1992) [Sov. Tech. Phys. Lett. **18**, 321 (1992)].

5. A. Goetzberger, Bell Syst. Tech. J. **45**, 1097 (1966).

6. O. S. Vdovin, Z. I. Kir'yashkina, V. N. Kotelkov, V. V. Novichkov, and V. A. Rozhkov, *Films of Rare-Earth Element Oxides in MIM- and MIS-Structures* (Saratovsk. Univ., Saratov, 1983).

7. M. Zerbst, Z. Angew. Phys. **22**, 30 (1966).

Translated by P. Pozdeev

Molecular-Dynamics Study of Dynamic Vortex Defects as the Mechanism of Relaxation in Loaded Solids

A. I. Dmitriev* and S. G. Psakhie

Institute of Strength Physics and Materials Science, Siberian Division, Russian Academy of Sciences, Tomsk, 634055 Russia
* e-mail: dmitr@usgroups.com
Received December 2, 2003

Abstract—Processes in a loaded solid have been studied by the method of molecular dynamics. It is established that dynamic vortex structures can form both in the stage of active loading and in the stress relaxation stage. In the latter case, atomic displacements can result in the formation of a periodic system of correlated vortex threads. The lifetime of such dynamic defects may reach tens of nanoseconds, while their characteristic dimensions are on the nanometer scale. It is demonstrated that the system of vortex threads can change the sign of the angular velocity so that atomic displacements taking place within different time intervals virtually compensate each other. The formation of analogous dynamic vortexlike structures in the active stage of loading does not exhibit a periodic character. © *2004 MAIK "Nauka/Interperiodica"*.

It is well known that the inhomogeneous distribution of displacements in a mechanically loaded real material may give rise to irreversible local structural transformations considered as defects mediating in the irreversible or plastic deformation of the given material [1]. The formation of such defects is essentially a means of retaining continuity of the material when a correlated motion of atoms is no longer possible [2]. At the same time, it was demonstrated [3–5] that so-called dynamic vortex defects may also exist, being formed in materials subjected to high-rate loading. The latter defects, involving a correlated vortex motion of a rather large number of atoms and ensuring a collective character of atomic displacements, can exist only in certain stages of loading.

Direct observation of the dynamic vortex defects is practically impossible, because they exist on a very small spatial and temporal scale. Nevertheless, the influence of these defects on the entire sample deformation process may have a mesoscopic or even macroscopic character. In particular, it was shown [3, 4] that dynamic vortex defects may account for the anomalously high velocity of grain boundary migration under the conditions of high-energy external action. The dynamic vortex defects are formed, as a rule, at the interfaces or near the free surface. This is explained by the requirement of a certain free volume for realization of the collective vortex behavior of the atomic subsystem.

It is commonly accepted that the dynamic defects exist only in the active stage of loading, where the induced displacement velocities are significantly higher than the characteristic rates of formation of the traditional defects. At the same time, the role of a rota-tional deformation mode as an important mechanism of internal stress release was emphasized within the framework of the physical mesomechanics [6]. In this context, we studied the possibility of dynamic vortex defect formation in the stage of internal material structure relaxation, that is, after termination of active loading. For this purpose, we used the molecular dynamics method to simulate the process of relaxation in a copper crystal with a free surface, which was preliminarily loaded in the compressive mode up to a level of deformation corresponding to plastic flow.

The model crystal is schematically depicted in Fig. 1a, where region I represents a freely strained part of the crystal, while regions II realized the so-called string boundary conditions [7] used for the simulation of external action. In the case under consideration, the projections of atomic velocities onto the [001] direction in regions II were fixed, while the projections onto other directions were determined by the corresponding atomic environment. In order to take into account the extension of the model fragment, we used periodic boundary conditions in the [010] direction and simulated free boundaries in the [100] direction. The interatomic interactions were described within the framework of the method of embedded atom [8].

In order to avoid the induced effects related to the symmetry of the ideal crystal lattice, the model copper crystal was heated to 20 K. The final temperature in the crystal was set based on the Maxwell distribution of atomic velocities. In the first stage, the model crystal was subjected to compression by displacing regions II at the velocities –50 and 50 m/s, respectively. The loading was continued until reaching the degree of deformation corresponding to plastic flow, after which the
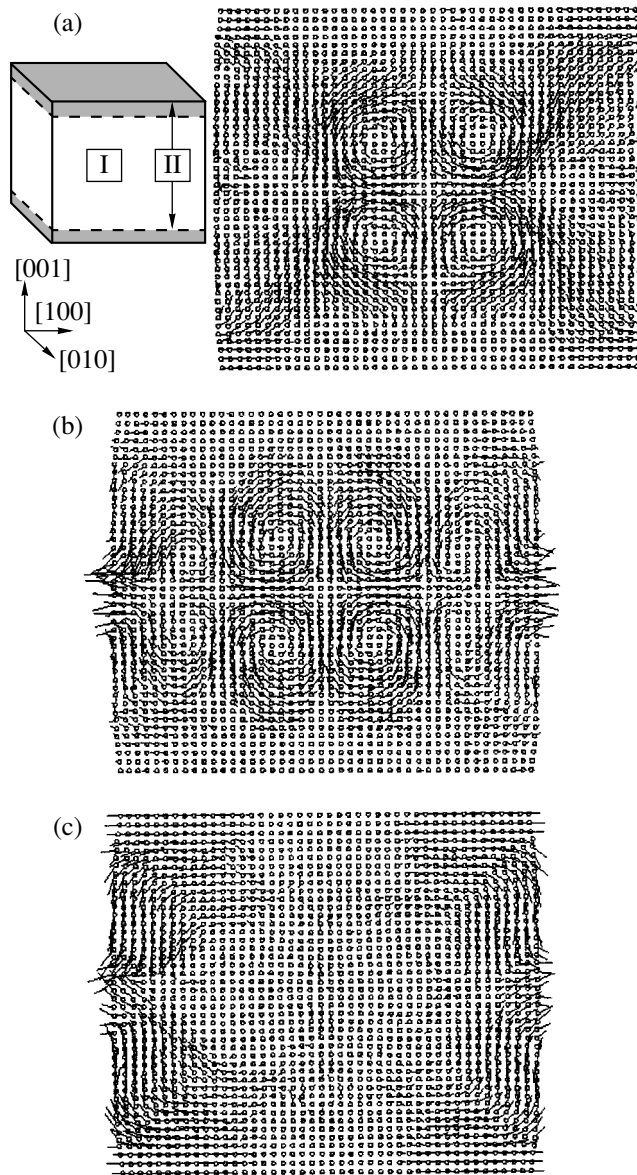
Fig. 1. Atomic displacements in the model crystal in various time intervals (in atomic units equal to 2.4189×10^{-17} s): (a) $(50-125) \times 10^3$; (b) $(125-150) \times 10^3$; (c) $(50-150) \times 10^3$.

crystal was allowed to relax. Detailed investigation of the relaxation process was performed by studying the time evolution of atomic configurations and atomic displacements.

The results of our investigation showed that relaxation of the model crystal is accompanied by the correlated vortexlike displacements of atoms. Figure 1 shows the pattern of atomic displacements in the model crystal in various time intervals in the plane parallel to the (010) crystal plane. For the sake of better illustration, the length of bars representing atomic displacements is increased by a factor of 10. As can be seen

from Fig. 1a, four vortex threads are formed in the central part of the crystal where atoms move around the axes parallel to [010], the diameter of vortices reaching 12 interplanar spacings. Note that the directions of rotation in the vortices are correlated so that the neighboring pairs have opposite signs of the angular velocities. As a result, the atomic displacements at the vortex boundaries are matched without breakage of the material continuity. Calculations showed that, in the course of relaxation, the system of four vortices (Fig. 1a) periodically changes the signs of angular velocities, whereby all the four vortices begin to rotate in the opposite direction. This is illustrated in Fig. 1b, which shows the pattern of atomic displacements in the subsequent time interval. It is clearly seen that atoms in the vortex threads move in the direction opposite to that for the same vortices in Fig. 1a.

It should be noted that the pattern of resulting displacements obtained by summing the displacements over a period of time equal to the sum of intervals corresponding to Figs. 1a and 1b (featuring vortex motions in the opposite directions) shows (see Fig. 1c) that the overall positions of atoms remain virtually unchanged. In other words, the atomic displacements observed during the time intervals corresponding to Figs 1a and 1b practically compensated each other so that atoms in the region under consideration, having performed correlated oscillations, returned to their initial positions. At the same time, the resulting atomic displacements in some other parts of the crystal (in particular, at the free surface) are far from being zero. Analysis of these results showed that alternation of the direction of rotation in the vortex threads can be considered as a mechanism of releasing internal stresses and overcoming potential barriers during evolution the system toward equilibrium.

Thus, the trajectory of the system under consideration in the phase space in the stage of atomic structure relaxation features involved atomic motions which can be considered as dynamic vortex defects. The results of model calculations showed that the lifetime of such dynamic defects may reach tens of picoseconds and their characteristic dimensions are on the nanometer scale. In our case, as well as in the papers cited above, the formation of dynamic vortex structures was also observed in the stage of active loading (where the vortex orientation also coincided with the [010] directions).

REFERENCES

1. R. De Wit, J. Res. Natl. Bur. Stand., Sect. A **77**, 49, 359, 607 (1973); *The Continuum Theory of Disclinations* (Mir, Moscow, 1977).

2. V. A. Likhachev, A. E. Volkov, and V. E. Shudegov, *The Continuous Theory of Defects* (Leningr. Univ., Leningrad, 1986).

3. S. G. Psakhie, S. Yu. Korostelev, S. I. Negreskul, *et al.*, Phys. Status Solidi B **176**, K41 (1993).

4. S. G. Psakh'e and K. P. Zol'nikov, Fiz. Goreniya Vzryva **34**, 126 (1998).

5. S. G. Psakh'e and A. I. Dmitriev, Zh. Tekh. Fiz. **64** (8), 186 (1994) [Tech. Phys. **39**, 850 (1994)].

6. *Physical Mesomechanics and Computer Design of Materials*, Ed. by V. E. Panin (Nauka, Novosibirsk, 1995).

7. A. I. Mel'ker, A. I. Mikhaĭlin, and E. Ya. Baĭguzin, Fiz. Met. Metalloved. **64**, 1066 (1987).

8. M. S. Daw and M. I. Baskes, Phys. Rev. B **29**, 6443 (1984).

Translated by P. Pozdeev

Measurement of High-Power Microwave Pulses by Resistive Hot-Electron Sensors

M. B. Goykhman, N. F. Kovalev*, N. G. Kolganov, and A. V. Palitsin

Institute of Applied Physics, Russian Academy of Sciences, Nizhni Novgorod, Russia
* e-mail: kovalev@appl.sci-nnov.ru
Received January 8, 2004

Abstract—Use of hot-electron semiconductor detectors for the measurement of high-power microwave pulses may lead to anomalously large errors. Methods of separation of the error signal and determination of the measurement error are considered. © *2004 MAIK "Nauka/Interperiodica"*.

Hot-electron semiconductor detectors [1] have proved to be a very convenient means of diagnostics in microwave electronics [2–4], especially for the measurement of short high-power pulses at a low repetition rate. The typical experimental arrangement for such measurements depicted in Fig. 1 is simple, convenient, and flexible. Unfortunately, use of this technique for the diagnostics of microwave oscillators with diffraction energy outputs, whereby the output signal contains higher harmonics, may lead to additional distortions of the shape of measured pulses [1].

Figure 2 shows several oscillograms of the output pulses of a hot-electron sensor. These patterns were observed in the experiments with a relativistic X-band backward wave oscillator (BWO) with an output power not exceeding 300 MW and a second-harmonic radiation fraction below 10^{-3}. The oscillograms were measured for a BWO operating in a constant regime, a fixed position of antennas, and a variable length of the waveguide. Determination of the oscillator output power of the pulses using the conventional calibration curve yields (a) 300, (b) 600, (c) 230, and (d) 150 MW.

This Letter is devoted to the elucidation of the origin of such a considerable scatter in the observed pulse shapes and to the determination of the corresponding errors.

The electric properties of a semiconductor material are described by the operator of electric conductivity,

$$j = \hat{j}[E], \qquad (1)$$

where j is the current density and E is the electric field. The latter two quantities are alternating functions of time, which are considered codirectional. The operator $\hat{j}[E]$ is nonlinear, antisymmetric ($\hat{j}[-E] = -\hat{j}[E]$), and (in the general case) integro-differential. In a limited interval of frequencies, this operator can be presented

as serially connected nonlinear resistor (ρ) and internal inductance (l). In what follows, the nonlinear properties of l will be ignored. For a correct limitation of the fre-
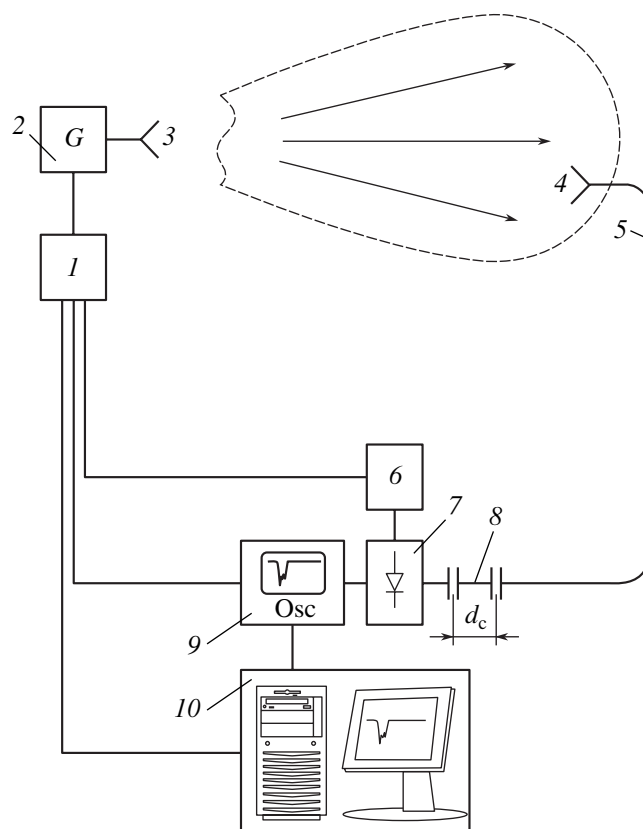

Fig. 1. A simplified scheme of measurements of the output radiation of a high-power relativistic microwave BWO: (*1*) control unit; (*2*) BWO; (*3*) radiator (dashed contour shows the directivity pattern); (*4*) receiving antenna; (*5*) waveguide; (*6*) controlled detector power supply; (*7*) hot-electron semiconductor sensor; (*8*) replaceable waveguide section of length d_c; (*9*) oscillograph; (*10*) data acquisition and storage system.

quency range, this inductance is represented as

$$l = \rho_0 \tau, \qquad (2)$$

where ρ_0 is the low-frequency resistivity of the semiconductor in a weak field and τ is the phenomenological relaxation time of the conductivity in a weak field. For example, high-ohmic n-type silicon at room temperature has $\tau \approx 10^{-12}$–10^{-10} s, which makes this material one of the most promising materials for resistive microwave sensors [1]. According to [1], the electric conductivity of silicon in a broad range of electric fields can be approximated by the following current–voltage characteristic:

$$j_v = \arctan E_v, \qquad (3)$$

where $j_v = \rho_0 j/E$ and $E_v = E/E_c$ are the normalized current density and field, respectively, and E_c is the critical field; the critical field, together with ρ_0 and τ, are the main characteristics of a given semiconductor material.

In order to elucidate the main laws of the hot-electron semiconductor detector operation, it is convenient to assume that the total field consists of only three parts,

$$E_v = E_0 + E_1 \cos \omega t + E_2 \cos(2\omega t + \phi), \qquad (4)$$

and the output signal is proportional to the slowly varying current density,

$$j_{v0} = E_0 - \frac{1}{3}E_0^3 - \frac{1}{2}E_0E_1^2 - \frac{1}{2}E_0E_2^2 - \frac{1}{4}E_1^2E_2\cos\phi. \qquad (5)$$

In Eqs. (4) and (5), E_0 is the constant field component, while E_1, E_2, and ϕ are the given functions of time, which can slowly vary on a $2\pi/\omega$ scale. In writing relation (5), the current density (3) was replaced by the truncated characteristic $j_v = E_v - 1/3\,E_v^3$.

In the regime of measurement of high-power microwave pulses of short duration, the constant field is usually selected small ($E_0 \ll E_1 \simeq 1$) [1] and, in the case of $E_2 = 0$, the detected signal

$$j_{vd} = -\frac{1}{2}E_0E_1^2 \qquad (6)$$

is proportional to the power flux density of the incident radiation ($P_1 \simeq E_1^2$) and the small constant background amplitude ($E_r = E_0 - 1/3E_0^3 \simeq E_0$). In the adopted model, signal and background have opposite polarities.

If the incident radiation contains a small second harmonic component (with the double frequency 2ω) such that $E_1^2 \gg E_2^2 \neq 0$, the detected signal is a sum of two signals,

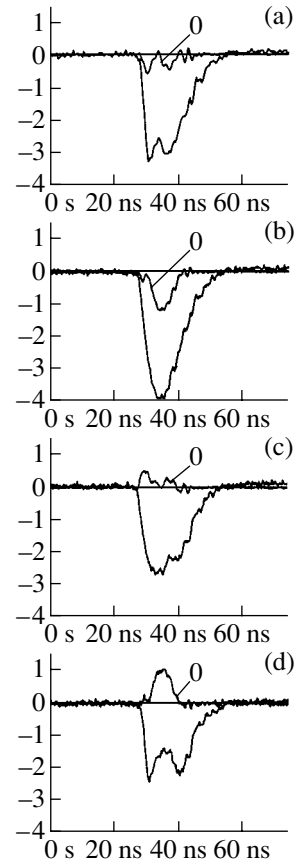$$j_{vd} = -\frac{1}{2}E_0E_1^2 - \frac{1}{4}E_1^2E_2\cos\phi. \qquad (7)$$

Fig. 2. Oscillograms of the output pulses of a hot-electron semiconductor sensor measured for various lengths d_c of the replaceable waveguide section (see the scheme in Fig. 1): (a) 0; (b) 2; (c) 4; (d) 6 cm; the corresponding error signals measured with the detector power supply switched off are designated "0."

Equation (7) differs from (6) by the additional term on the right-hand side which, being also proportional to P_1, may have any polarity, depending on the phase difference ϕ between the harmonics. In the calibration stage, this additional component practically cannot be taken into account and should be considered as an error. For $E_2 \geq 2E_0$, this error may reach a level comparable with the main signal (6). For example, in the case of $\rho \approx 10\ \Omega$ cm, $E_0 \approx 10$ V/cm, and $P_2 \approx 1$ W, the error signal amplitude reaches 0.2 of the main signal amplitude (for $P_1 \simeq 10^4$, $P_2/P_1 \simeq 10^{-4}$).

The error signal, being independent of E_0, still exists when the detector power supply is switched off ($E_0 = 0$). This characteristic property can be used for determining the measurement error and, sometimes, for restoration of the main signal amplitude (6). For the sake of illustration, Fig. 2 shows (together with the output signals measured at $E_0 \neq 0$) the corresponding error signals (designated (0)) having, in accordance with (7), a shorter duration and alternating polarity (depending on the phase ϕ). The phase ϕ was changed by varying the

waveguide length (d_c): an increase in d_c by 4 cm changed the phase ϕ by π.

The additional signal is proportional to the second harmonic field (more precisely, to $\simeq E_2 \cos\phi$), which can be excited both by the incident radiation and by the second harmonic current

$$ j_{v2} \approx E_2\left(1 - \frac{1}{2}E_1^2\right)\cos(2\omega t + \phi) - \frac{1}{2}E_0 E_1^2 \cos 2\omega t \quad (8) $$

passing via the internal (and external) circuit of the detector, in particular, via the internal inductance (l). As a result, the shape of the error signal becomes dependent on the frequency properties of elements entering into the high-frequency ($\approx 2\omega$) equivalent detector scheme, which may introduce additional distortions in the output signal (7).

It is necessary to make some additional qualitative comments. The current–voltage characteristic of a semiconductor material is antisymmetric. Upon application of a small constant field (E_0), the working point exhibits a shift leading to the appearance of a quadratic nonlinearity ($j_v \simeq \ldots -E_0 E_v^2$) responsible for the detection effect, that is, for the main signal (6). For small shifts ($E_0 \ll 1$), the characteristic (3) retains a large cubic nonlinearity ($j_v \simeq \ldots -1/3\, E_v^3$) on which the second harmonic field generates errors (together with the first harmonic field). Since the cubic nonlinearity predominates, even a small second harmonic field ($E_0 \simeq E_2 \ll 1$) makes the error signal comparable with the main signal. As was noted above, the second harmonic field also arises due to the passage of the second harmonic current via elements of the detector scheme. This current component is generated on a small quadratic

nonlinearity by the first harmonic field (which is maximum in the regime under consideration). Both processes affect the shape of the output pulse and have to be taken into account in solving the inverse problem of restoration of the high-frequency pulse envelope from the output pulse.

Conclusion. The phenomena considered above are not unique and accompany the operation of any detector employing nonlinear current–voltage characteristics. These phenomena are known both in the theory of oscillations and in the theory of resistive microwave sensors [1]. Our aim was only to attract the attention of researchers to the danger of encountering large errors in the measurement of high-power microwave pulses of short durations by widely used resistive hot-electron semiconductor sensors. Under typical conditions of such measurements, this factor can lead to severalfold overstated values of the peak power and the efficiency.

REFERENCES

1. V. Dienys, A. Pauza, J. Pozela, *et al.*, in *Electrons in Semiconductors* (Mokslas, Vil'nyus, 1980), Vol. 2, pp. 9–72.

2. V. I. Belousov, V. I. Zelentsov, M. M. Ofitserov, *et al.*, in *Relativistic Microwave Electronics* (Inst. Prikl. Fiz. Akad. Nauk SSSR, Gorky, 1979), pp. 275–292.

3. A. I. Klimov, Prib. Tekh. Éksp., No. 6, 86 (1999).

4. M. Dagys, Z. Kancleris, R. Simniskis, *et al.*, IEEE Antennas Propag. Mag. **43** (5), 64 (2001).

Translated by P. Pozdeev

The Parameters of Phase Separation in NT-50 Alloy Calculated from the Internal Friction Kinetics

V. M. Arzhavitin

Kharkov Physicotechnical Institute, National Scientific Center, Kharkov, Ukraine
e-mail: vasil@kipt.kharkov.ua (TO: AR)
Received December 22, 2003

Abstract—An analytical expression for the internal friction kinetics $Q^{-1}(t)$ in the course of isothermal aging is obtained for a Nb–(48.5 ± 1.5%)Ti alloy. The numerical analysis of anomalies of the $Q^{-1}(t)$ function showed that, during the first three hours of annealing at 300 and 375°C, the α-Ti phase is separated in a single stage without the formation of intermediate α', α", or ω phases. Using the experimental curves of $Q^{-1}(t)$, the values of parameters (K and n) are determined for the Avrami equation describing the kinetics of α-Ti phase separation. © *2004 MAIK "Nauka/Interperiodica".*

Niobium–titanium (NB–Ti) alloys containing 48.5 ± 1.5% Ti (technical grade NT-50) possess a sufficiently high plasticity for making wires. This material is most frequently used for manufacturing superconducting solenoids. In some countries, alloys of the NT-50 type are produced on a commercial scale. In such Nb–Ti alloys, the current-carrying structure is formed as a result of the diffusion-controlled decomposition of a supersaturated solid solution. It is commonly accepted that the critical current density in Nb–Ti alloys is determined primarily by the α-Ti phase precipitated in the course of heat treatments.

The kinetics of α-Ti phase formation in NT-50 alloy was thoroughly studied using electron microscopy and other methods for the samples upon practically significant annealing times (≥10 h). In this stage, new particles of the α-Ti phase are not formed and the existing precipitates grow by means of diffusion [1]. In contrast, the kinetics of the α-Ti phase formation during isothermal annealing for a short time (~1 h) is still insufficiently studied. This is related to the fact that particles formed in NT-50 alloy during the first several hours are extremely small and their identification encounters considerable difficulties.

It was found that the problem of "first hours" for NT-50 alloy is most expediently solved using the method of internal friction [2], which is highly sensitive with respect to incoherent and semicoherent precipitates. In the case of completely coherent precipitates, the sensitivity of this method is low. It was established [2] that the internal friction $Q^{-1}(t)$ measured by method of decaying torsional oscillations for the cast NT-50 alloy monotonically decreases in the course of isothermal annealing at 375°C and exhibits a drop at $t \approx 90$ min (Fig. 1, experimental curve *1*). Using the same method, an analogous "jump" in the internal friction was previously observed by Dijkstra (see [3]) for a supersatu-

rated solution of nitrogen in α-Fe isothermally annealed below 250°C. The results of metallographic analysis showed that the separation of a stable nitride Fe_4N during decomposition of an iron–nitrogen alloy proceeds in two sequential stages with the formation of a less stable intermediate nitride Fe_8N.

By analogy with the data for iron nitrides, it was suggested [2] that a two-stage separation of α-Ti takes place in the bulk of isothermally aged NT-50 alloy with the formation of some intermediate (metastable) compounds, probably titanium-rich α', α", or ω phases. These phases (absent in the equilibrium phase diagram of the NB–Ti system) were revealed by X-ray emission spectroscopy in Nb–Ti binary alloys (containing <32 wt % Nb) quenched from 1000°C [4].
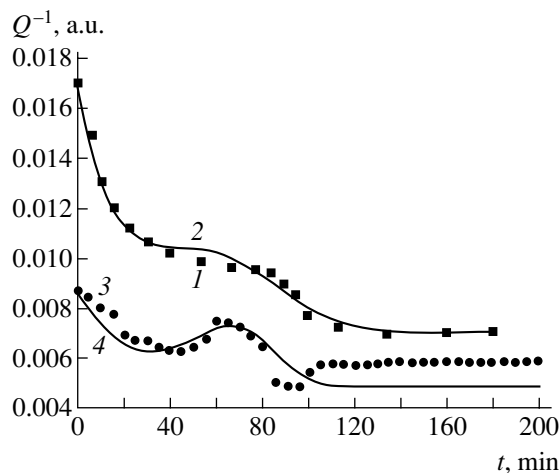

Fig. 1. Internal friction kinetics in (*1, 2*) cast and (*3, 4*) cold-deformed NT-50 alloy isothermally annealed at (*1, 2*) 375°C and (*3, 4*) 300°C: (*1, 3*) experiment; (*2, 4*) calculations by Eqs. (7) and (8).

This paper addresses the mechanism of time-dependent internal friction $Q^{-1}(t)$ without assuming the necessary formation of nonequilibrium intermediate phases in isothermally aged NT-50 alloy. The proposed model provides a basis for the quantitative analysis of experimental $Q^{-1}(t)$ curves for NT-50.

Belko *et al.* [5] proposed a microscopic (atomic) mechanism of high-temperature internal friction in isothermally aged alloys. According to this, the formation of a new phase begins with thermofluctuational nucleation of the growth centers (nuclei) of critical dimensions, followed by their growth via a diffusion-controlled mechanism. The time-dependent external stress $\sigma(t)$ changes the nucleation activation energy from $U(0)$ to $U(\sigma) = U(0) - ve\sigma(t)$, where $ve\sigma$ is the work of the external harmonic stress spent for the formation of a nucleus, v is the effective volume of the critical nucleus, and e is the relative change in the lattice parameter at the phase transition point. Since the density of nuclei deviates from the equilibrium value, the equation for the low-frequency internal friction can be written as

$$2\pi Q^{-1} = \frac{G v e^2 V}{f\, kTV_0},\qquad(1)$$

where G is the elastic modulus of the given material, f is the frequency of forced oscillations, k is the Boltzmann constant, V_0 is the total volume of the material, and V is the converted volume for a given time. According to the thermofluctuational mechanism of internal friction, the straining stress in alloys is significantly lower than the conditional yield point ($\sigma \ll \sigma_{0.2}$) and, hence, the effect of measuring facilities on the phase decomposition kinetics is negligibly small.

The kinetics of polymorphous transitions, interrupted precipitation, and eutectic decomposition is usually described in terms of the Avrami equation [6, 7],

$$V = V_0[1 - \exp(-Kt^n)],\qquad(2)$$

where K and n are the parameters of the process under consideration. Equation (2) with $n = 1$ describes nucleation at the grain boundaries after exhaustion of the nucleation sites; $n = 2$ refers to the nucleation of grain edges after exhaustion of the previous nucleation sites; and $3 \leq n \leq 4$ corresponds to a decrease in the nucleation rate. The case of $n > 4$ refers to alloy decomposition with increasing phase nucleation rate. In the general case, a single-stage separation of one phase (e.g., of α-Ti) may correspond to various pairs of K and n values.

Taking into account the Avrami equation (2), formula (1) for the thermofluctuational internal friction mathematically reduces to

$$Q^{-1}(t) = cKnt^{n-1}\exp(-Kt^n),\qquad(3)$$

where $c = ve^2G/2\pi fkT = \text{const}$. According to this relation for $n = 1$ (first-order kinetics), the internal friction

monotonically decreases with time according to an exponential law: $Q^{-1}(t) \sim \exp(-Kt)$. For $n > 1$, the internal friction exhibits a maximum. Using the condition of extremum $dQ^{-1}/dt = 0$, we obtain

$$t_{\mathrm{p}} = \left(\frac{n-1}{nK}\right)^{1/n},$$

where t_{p} is the time to the internal friction peak. This value is uniquely determined by the decay constants K and n.

Since formulas (1) and (3) were obtained for the regime of forced oscillations, the question naturally arises as to whether these relations can be used for an analysis of the phase decomposition kinetics as studied by the method of decaying oscillations. Note that formula (1) contains the driving force frequency in the form $1/f$, which corresponds to a Maxwell solid described by the equation of viscoelasticity [8, 9],

$$\frac{d\gamma}{dt} = \frac{1}{G}\frac{d\sigma}{dt} + \frac{\sigma}{\eta},\qquad(4)$$

where G is the nonrelaxed elastic modulus of the medium; γ and η are the inelastic strain and viscosity of the material, respectively; and $\tau = \eta/G$ is the characteristic stress relaxation time according to Maxwell. The torsional pendulum, whose rheological properties are described by the Maxwell model (4), can perform decaying oscillation [10]. With neglect of the contribution of high-order modes to decaying oscillations of the torsional pendulum, the angle of torsion is given by the formula

$$\varphi = a\{1 + b[\exp(-\beta t)]\sin(2\pi ft - \vartheta)\},$$

where a, b, and ϑ are constant quantities (for a given experiment) and β is the damping coefficient. For a low damping level ($\beta \ll 1$), the internal friction obeys the relation

$$2\pi Q^{-1} = \frac{1}{f\tau} = \frac{G}{f}\frac{1}{\eta},\qquad(5)$$

where f is the natural frequency of free oscillations of the torsional pendulum. As can be seen, expressions (1) and (5) have mathematically equivalent structures. For this reason, formula (1) can be used for an analysis of phase variations in the regime of decaying oscillations (e.g., in ferroelectric ceramics [11, 12]), considering the decomposing alloy as a Maxwell medium with the effective viscosity $\eta = kTV_0/(ve^2\dot{V})$.

Figure 1 shows the experimental behavior of $Q^{-1}(t)$ for two samples of NT-50 alloy isothermally annealed at 375°C (curve *1*) and 300°C (curve *3*). The first sample (cast material) with a diameter of 3 mm was cut from an NT-50 alloy casting. The second sample (cold-deformed material) had the form of a 1.5-mm-diam wire obtained by drawing the initial cast alloy to 90% without preliminary and intermediate heat treatments. The internal friction in the wire was measured in the

regime of decaying torsional oscillations at a maximum amplitude of $\gamma_0 \leq 10^{-4}$ and a frequency of $f \approx 3$ Hz. On the temperature axis, the point $T = 300°C$ is close to the temperature of $Q^{-1}(t)$ maximum (Fig. 2) corresponding to the α-Ti phase precipitation in the cold-deformed NT-50 alloy [2].

The $Q^{-1}(t)$ curve of the cold-deformed alloy sample exhibits a maximum in the internal friction instead of the aforementioned "jump." Taking into account the shape of the experimental kinetic curves (Fig. 1, curves *1* and *3*), let us represent the contribution $\Delta Q^{-1}(t)$ due to precipitated phases to the total internal friction $Q^{-1}(t)$ as a sum

$$\Delta Q^{-1}(t) = cK_1 \exp(-K_1 t) + cK_2 n t^{n-1} \exp(-K_2 t^n), \quad (6)$$

where the first and second terms describe the monotonic decrease and the temporal maximum in the internal friction, respectively.

In the general case, the internal friction is not an additive quantity. Representation (6) is valid only for values of internal friction significantly smaller than unity [8]. This approximation implies that two different single-stage processes of the α-Ti phase separation proceed simultaneously and independently. Using Eq. (6), the ratio $\Delta Q^{-1}(t)/\Delta Q^{-1}(0)$ can be approximated by a three-parameter expression

$$\begin{aligned} \Delta Q^{-1}(t)/\Delta Q^{-1}(0) \\ = \exp(-K_1 t) + (K_2/K_1)n t^{n-1} \exp(-K_2 t^n), \end{aligned} \quad (7)$$

where K_1, K_2, and n are three decay parameters to be determined. The quantity n is most informative: the numerical values of this parameter have been tabulated and the corresponding mechanisms described by Cahn [7].

Using relation (7), the time variation of the internal friction can be presented as

$$\begin{aligned} Q^{-1}(t) = Q_0^{-1}(t) + \Delta Q^{-1}(t) = Q_0^{-1}(t) \\ + \Delta Q^{-1}(0)[\exp(-K_1 t) + (K_2/K_1)n t^{n-1} \exp(-K_2 t^n)], \end{aligned} \quad (8)$$

where $Q_0^{-1}(t)$ is the analytically undetermined background component varying with time at a slower rate than the second term in this equation. In the general case, the background $Q_0^{-1}(t)$ may change with time under the action of various factors, in particular, as a result of the precipitation hardening according to the Orowan mechanism or due to small microplasticity development (irrespective of the phase variations) for a strain amplitude of $\gamma_0 \leq 10^{-4}$.

To the first approximation, we can assume that the background does not change with time, $Q_0^{-1}(t) = const$. Then, according to formula (8), Q_0^{-1} is the value of
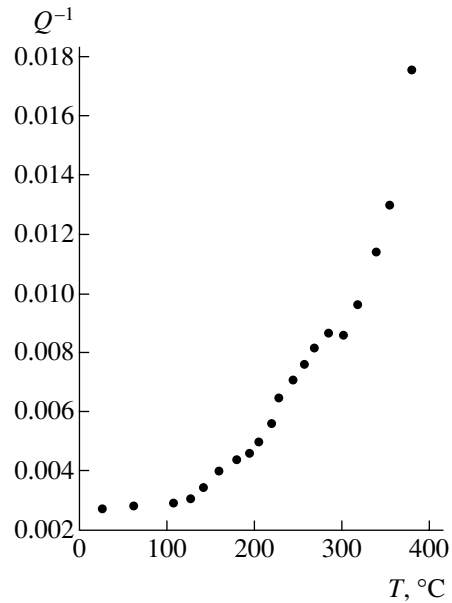

Fig. 2. Temperature dependence of the internal friction in cold-deformed NT-50 alloy.

internal friction for an infinitely large time ($t = \infty$) of isothermal annealing. The exact value of $Q^{-1}(\infty)$ cannot be unambiguously determined from experimental data (see Fig. 1). To an acceptable accuracy, we may assume that the decomposition process is mostly completed within $t \geq 90$ min and the corresponding experimental value of $Q^{-1}(t)$ approximately corresponds to Q_0^{-1}. The values of Q_0^{-1} and other aging constants for NT-50 alloy determined from the experimental internal friction curves $Q^{-1}(t)$ are given in the table.

The results of computer-aided processing of the experimental curves of internal friction (Fig. 1, curves *1* and *3*) in terms of formulas (7) and (8) are presented in Fig. 1 (curves *2* and *4*). As can be seen from these data, the dominating process of α-Ti phase separation obeys the first-order kinetics. Then, curve *4*, corresponding to the cold-deformed sample, exhibits an additional peak of internal friction at $t = 65$ min, for which $n = 4.4$ (see table). The approximating function for the cast alloy exhibits no extrema.

It should be noted that reliable values of the parameters K and n in the Avrami equation of aging kinetics

The parameters of internal friction kinetics in isothermally aged NT-50 alloy

T, °C	$Q_0^{-1} \times 10^3$	$K_1 \times 10^2$, 1/min	K_2, 1/(min)^n	n	t_p, min
300	4.85	4.10 ± 0.33	$(1.6 \pm 0.1) \times 10^{-5}$	4.4 ± 0.50	65
375	2.033	4.38 ± 0.18	$(6.9 \pm 0.2) \times 10^{-9}$	2.6 ± 0.75	–

can be obtained using mathematical model (8) only provided that the experimental data are sufficiently precise and the background level Q_0^{-1} of the internal friction remains constant during the entire period of observation of the phase separation process. Nevertheless, the thermofluctuational mechanism of internal friction [5], together with the Avrami approach to the phase separation kinetics [7] explain both the "jumps" (Fig. 1, curve *1*) and peaks (Fig. 1, curve *3*) observed in the internal friction kinetics in NT-50 within the framework of a single-stage model of α-Ti phase formation without recourse to the nonequilibrium α', α'', or ω phases.

REFERENCES

1. O. V. Chernyj, G. F. Tikhinsckij, G. E. Storozhilov, *et al.*, Supercond. Sci. Technol. **4**, 318 (1991).

2. B. I. Shapoval, G. F. Tikhinskiĭ, A. I. Somov, *et al.*, Vopr. At. Nauki Tekh., Ser.: Obshch. Yad. Fiz. **3** (13), 6 (1980).

3. J. D. Fast, *Interaction of Metals and Gases* (Centrex, Eindhoven, 1965; Metallurgiya, Moscow, 1975), pp. 262–265.

4. Yu. A. Bagaryatskiĭ, G. I. Nosova, and T. V. Tyagunova, Dokl. Akad. Nauk SSSR **122**, 593 (1958) [Sov. Phys. Dokl. **3**, 1014 (1958)].

5. V. N. Belko, B. M. Darinskiĭ, V. S. Postnikov, and I. M. Sharshakov, Fiz. Khim. Obrab. Mater., No. 2, 131 (1969).

6. R. W. Cahn, Acta Metall. **7**, 18 (1959).

7. *Physical Metallurgy,* Ed. by R. W. Cahn (North-Holland, Amsterdam, 1965; Mir, Moscow, 1968), Vol. 2, pp. 270–278.

8. V. O. Shestopal, *Rheological Properties of Pure Metals at High Temperatures* (Metallurgiya, Moscow, 1978), pp. 91–92.

9. V. V. Novikov and K. W. Wojtciechowski, Zh. Éksp. Teor. Fiz. **122**, 538 (2002) [JETP **95**, 462 (2002)].

10. V. S. Postnikov, *Internal Friction in Metals* (Metallurgiya, Moscow, 1974).

11. S. A. Gridnev, B. M. Darinskiĭ, and V. S. Postnikov, Izv. Akad. Nauk SSSR, Ser. Fiz. **33**, 1187 (1969).

12. S. A. Gridnev, V. S. Pavlov, V. S. Postnikov, and S. K. Turkov, *Analytical Capabilities of the Method of Internal Friction* (Nauka, Moscow, 1973), pp. 108–121.

Translated by P. Pozdeev

Accelerating Diffraction Structure of the π Type

S. V. Abramov, Yu. K. Alekseev, D. A. Zayarny, B. S. Ishkhanov, and V. I. Shvedunov*

Research Institute of Nuclear Physics, Moscow State University, Moscow, Russia
* e-mail: shved@depni.sinp.msu.ru
Received January 8, 2004

Abstract—We have numerically simulated a laser-excited symmetric periodic diffraction structure, comprising conducting plates deposited onto dielectric film substrates, intended for the high-gradient acceleration of charged particles. The parameters of this structure were optimized to provide that a relativistic particle is accelerated in the near field diffraction zone over the entire spatial period. The possibility of eliminating the parasitic perpendicular components of the electric and magnetic fields in the plane of symmetry by means of bilateral laser irradiation is considered. © 2004 MAIK "Nauka/Interperiodica".

Use of a laser beam in the free space or a resonance field of an electrodynamic system of the Fabry–Perot type in electron accelerators, amplifiers, or generators with longitudinal interaction is determined to a considerable extent by the possibility of formation of a structure ensuring sharply inhomogeneous (on a wavelength scale) distribution of the field amplitude. The interaction of charged particles with an unperturbed wave in the free space is ineffective because of adiabatically slow spatial variation of the field amplitude [1]. By arranging various metallic or dielectric perturbing bodies in the field of a laser beam, it is possible to provide for the acceleration of particles with a high rate of energy gain [2], the effective modulation of the longitudinal velocity, and the extraction of the energy of electron bunches. A promising method of increasing the efficiency of such energy exchange is based on the use of a diffraction grating arranged in a laser beam, ensuring the interaction between charged particles and the laser field in the near diffraction zone [3].

We have studied and optimized an accelerating diffraction structure with distributed electric field vector amplitude, in which a charged particle is accelerated by the electric field in both spatial half-periods. This accelerating system (π-type structure in terms of the accelerating systems operating in the classical wavelength range) is capable of providing for a greater increment of the particle energy per unit length (at a fixed amplitude of the laser radiation) than the system described in [2]. A possible radiation source for the proposed model is a CO_2 laser operating at $\lambda = 10.6$ μm.

The model structure (Fig. 1) comprises a conducting (copper) grating with elements of width L_{cond} and thickness h_{cond} deposited onto a dielectric film substrate (e.g., GaAs). The substrate is transparent at a selected radiation wavelength and is characterized by the thickness h_d and permittivity ε. The second identical grating is arranged symmetrically to the first so that the internal surfaces of the dielectric substrates are spaced by a dis-

tance of $2a$. The axis of a beam of charged particles lies in the symmetry plane of the structure at a distance of a from the internal surfaces of the dielectric films.

We have simulated the excitation of electromagnetic oscillations of the above electrodynamic system by a laser field representing a plane linearly polarized wave propagating along the y axis. For this purpose, we have numerically solved the Maxwell equations in the region of space within a distance of $2\lambda = 21.2$ μm from the structure along the y axis. The boundary conditions along the x and z axes represented the infinite periodic continuation of the structure. A solution of the system of Maxwell equations is represented by the set of complex vectors $\mathbf{E}_x$, $\mathbf{E}_y$, $\mathbf{E}_z$ and $\mathbf{H}_x$, $\mathbf{H}_y$, $\mathbf{H}_z$ describing spatiotemporal evolution of the electromagnetic field.

Analysis of the obtained numerical solution showed that the distribution of the accelerating field component $\mathbf{E}_z$ in the structure under consideration has the form of a sequence of field spots with alternating sign of this
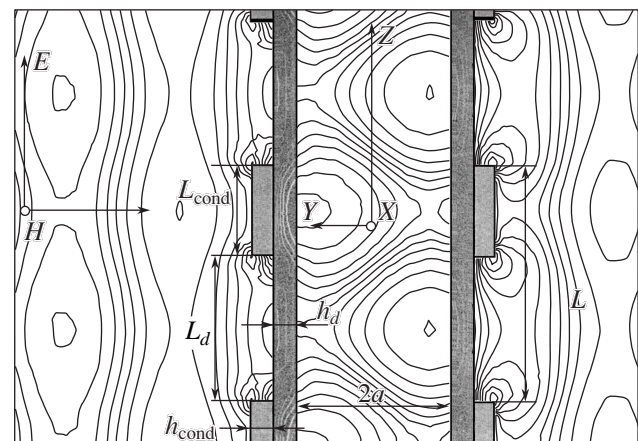

Fig. 1. Schematic diagram of the proposed accelerating structure irradiated with plane waves (see the text for explanations).
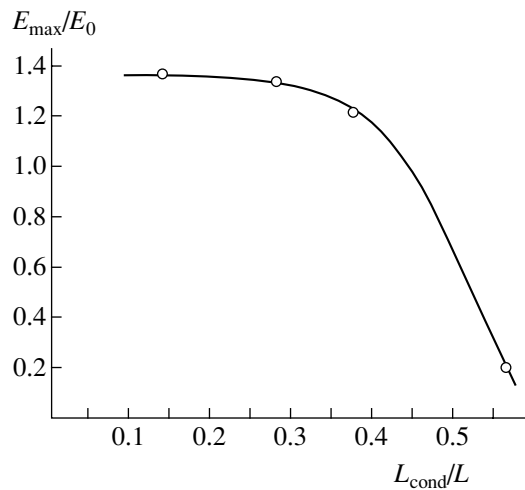
E_{max}/E_0

Fig. 2. A plot of the field strength in the accelerating structure versus the width of conducting elements in the diffraction grating.

component (Fig. 1). We optimized the resonator parameters (in particular, the distance between dielectric films, the thickness of these films, and the width of conducting elements) so as to provide that $\mathbf{E}_z$ would be described by a harmonic function oscillating relative to zero (from $-\mathbf{E}_{z0}$ to $\mathbf{E}_{z0}$) over a segment of length λ along the z axis. The corresponding parameters of the accelerating structure are as follows: $L_{cond} = 4$ μm, $h_{cond} = 1$ μm, $h_d = 0.93$ μm, $\varepsilon = 3.47$, and $a = 3.55$ μm. The resulting spatial distribution of the accelerating field component $\mathbf{E}_z$ ensures a gain in the energy of a relativistic particle in each half-period of the alternating field (for a correctly selected particle phase at the system entrance).

A serious obstacle to using such diffraction gratings for the acceleration of charged particles is related to the presence of electromagnetic field components differing from $\mathbf{E}_z$ on the beam axis. During a unilateral excitation of the field oscillations in the structure by laser radiation with the $\mathbf{E}_z$ vector oriented in the direction of particle flight, there also arise the electric field component $\mathbf{E}_y$ and the magnetic field component $\mathbf{H}_x$ on the beam axis. The values of these fields are sufficiently large, which can result in a significant transverse shift of the beam.

In order to solve this problem, we suggest to use a bilateral irradiation of the accelerating structure with two plane linearly polarized waves propagating in opposite directions. The electric vectors $\mathbf{E}$ in the incident waves are collinear and vary in time with the same phase; accordingly, the magnetic vectors $\mathbf{H}$ at each moment of time have equal magnitudes and opposite directions. As a result, the field components $\mathbf{E}_y$ and $\mathbf{H}_z$ for each of the two incident waves must have equal magnitudes and opposite directions at each moment of time to give zero on adding, which was confirmed by the model calculations. The accelerating components $\mathbf{E}_z$ of the electric vector of each wave in the plane of

symmetry of the structure have equal magnitudes and the same direction, so that the total $\mathbf{E}_z$ value is doubled.

In order to evaluate the efficiency of using the proposed periodic wave structure of the π type in a linear electron accelerator, we have estimated the main parameters of such a structure, including the energy gradient $T = \Delta W/L$ and the effective shunt resistance $Z_{sh} = \Delta W^2/2PL$, where $2P$ is the total power of bilateral irradiation, L is the structure length, and ΔW is the electron energy gain over length L. The distribution of the accelerating field component was approximated by the harmonic function $E_z(z, t) = E_1\sin(2\pi z/\lambda)\sin(\omega t + \varphi)$, where E_1 is the maximum field amplitude and φ is the initial phase. Solution of the equation of electron motion over one period of the accelerating structure showed that the energy gradient of an ultrarelativistic particle for the given field profile is $T(eV/m) = E_1(V/m)/2$.

For an incident wave amplitude of 1.5 GV/m, the field amplitude on the axis of the accelerating structure is $E_l = 3.6$ GV/m and the energy gradient is $T = 1.8$ GeV/m. For a field spot size of the laser beam on the order of $2 \times 20 \times \lambda^2$, the pulse power is 26.8 MW and the shunt resistance is $Z_{sh} = 12.8$ MΩ/m. The pulse duration (determined by time of flight through the structure) for a relativistic electron is 0.7 ns, the pulse energy is 19 μJ, and the energy density on the grating surface is 4.2 kJ/m² (which is less than half of the ablation limit for the given metal [4]). For comparison, the acceleration rate in the structure described in [2] for the same accelerating field strength was $T = E_l/\pi = 1.15$ GeV/m.

It should be noted that the proposed accelerating structure is not a resonance system: the optimum field distribution for the π-type structure is obtained far from the resonance in a system considered as an open resonator of the Fabry–Perot type. While the resonance in the structure takes place for $a = 6.4$ μm, the optimum field distribution in the π-type structure is achieved for $a = 3.55$ μm. This is evidence of the key role of the diffraction field of the grating in the process of charged particle acceleration.

Variation of the width of conducting elements of the structure leads to a rather smooth change in the field amplitude, as depicted in Fig. 2.

REFERENCES

1. A. V. Gaponov and M. A. Miller, Zh. Éksp. Teor. Fiz. **34**, 242 (1958) [Sov. Phys. JETP **7**, 168 (1958)].

2. Yu. K. Alekseev and V. I. Shvedunov, Preprint No. 99-25/583, NPI MSU (Nuclear Phys. Inst., Moscow, 1999).

3. P. V. Schoessow and J. B. Rosenzweig, in *Proceedings of the 18th Biannual Particle Accelerator Conference PAC-99, New York, 1999*, pp. 3624–3626.

4. Yu. V. Afanas'ev, N. N. Demchenko, and I. N. Zavetovskaya, Izv. Akad. Nauk, Ser. Fiz. **63**, 667 (1999).

Translated by P. Pozdeev

Field Evaporation of Tungsten
in the Presence of Adsorbed Water

N. M. Blashenkov, G. Ya. Lavrent'ev, and V. N. Shrednik

Ioffe Physicotechnical Institute, Russian Academy of Sciences, St. Petersburg, 194021 Russia
Received January 22, 2004

Abstract—The field evaporation of tungsten at $T = 300$ and 600 K in the presence of water vapor in the residual atmosphere was studied using a static mass spectrometer with a moderate resolution ($M/\Delta M = 200$). The room-temperature mass spectrum of field-evaporated particles displayed only the peaks of triply charged ions; an increase in the temperature to 600 K added the peaks of doubly charged ions of approximately the same intensity. The presence of adsorbed water reduced the evaporating field strength by a factor of 2–2.5. At 300 K, an increase in the water content in the residual atmosphere markedly enhanced the field etching. No singly or quadruply charged tungsten ions were observed. The results are indicative of the activation mechanism of field evaporation at the temperatures studied and show evidence of a substantial decrease in the magnitude of evaporating field caused by the presence of water. © *2004 MAIK "Nauka/Interperiodica".*

The field evaporation of refractory metals was most thoroughly studied in the case of atomically clean surfaces at cryogenic temperatures (usually for samples cooled by liquid nitrogen) [1]. Tungsten is characterized by the typical ions W^{2+}, W^{3+}, and W^{4+} and evaporating field strengths of about 5.5×10^8 V/cm. The presence of a chemically active impurity on the metal surface changes the character of interatomic bonds and substantially facilitates the field evaporation process. The so-called "field etching" was observed long ago for some active adsorbates such as water and nitrogen. However, no systematic investigations of this effect and the corresponding ion charge distribution were performed at room temperature.

This Letter reports on the results of investigation of the field evaporation of tungsten at room temperature and on heating in the presence of water vapor in the residual atmosphere. We have determined the charges of field-evaporated ions, the magnitudes of evaporating field, and the relative evaporation rates at various temperatures and residual gas pressures.

The investigation was performed using a static mass spectrometer with a moderate resolution ($M/\Delta M = 200$) capable of readily resolving the peaks of tungsten isotopes. The angle of ion collection from the tungsten point was 6°. The electron-optic system of the ion source allowed the accelerating voltage (and, hence, the field strength at the point tip) to be varied within two orders of magnitude while maintaining the focusing of ions with fixed energies on the exit slit of the ion source. This ensured constant sensitivity and high precision in the measurement of desorbed ion flux in a broad range of electric fields [3].

The residual gas pressure in the mass spectrometer chamber was 8×10^{-7} Torr. In the regime field etching, the pressure increased to $(2.5–3.5) \times 10^{-6}$ Torr, as determined from the mass spectrum measured with an additional electron-impact ionization source. The main component in the residual atmosphere was water vapor: protonated water ions $H_2O \cdot H^+$ (19 amu) and $2H_2O \cdot H^+$ (37 amu) were always present in the spectra. The appearance of $H_2O \cdot H^+$ ions (corresponding to a field strength about 7×10^7 V/cm) in the course of voltage increase was used for calibration of the electric field strength. Therefore, the field evaporation of tungsten took place under the conditions of field etching in the presence of water and required lower field strengths as compared to the case of pure field evaporation.

The tungsten points were prepared by electrolytic etching in a dilute NaOH solution. The point temperature in the range of optical emission was determined by pyrometry, and at lower temperature, by interpolation of the resistance of a point holder between the room temperature and the pyrometric value.

The field-evaporation mass spectra were measured at room temperature (about $T = 300$ K, Fig. 1) and on heating to about 600 K (Fig. 2). In both cases, the evaporating voltage was established on the same level corresponding to a field strength of 2×10^8 V/cm. The evaporating field strength slightly decreased with time as a result of the point blunting. Thus, the evaporating field was always 2–2.5 times lower than that (5×10^8 V/cm) corresponding to the intense field evaporation of tungsten under high vacuum conditions. It should be noted that the field evaporation under the conditions studied proceeded at a low rate and ions were detected by a secondary electron multiplier operating in the pulse count mode.

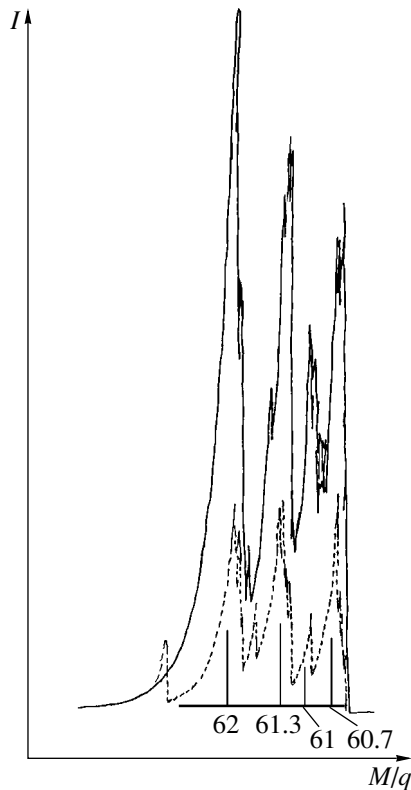The first experiment was devoted to the detection and investigation of the field evaporation of tungsten at

Fig. 1. Room-temperature field evaporation mass spectra of triply charged tungsten ions measured for two values of the residual gas pressure: 1.5×10^{-6} Torr (dashed curve) and 2.5×10^{-6} Torr (solid curve). The ordinate (evaporation rate I) is approximately proportional to the number of detected ions; the abscissa M/q is the ion mass-to-charge ratio. The reference bars in the bottom part correspond in both position (M/q) and height (I) to the published data for tungsten isotopes.

Fig. 2. The field evaporation mass spectrum of doubly charged tungsten ions measured at $T = 600$ K. The ordinate scale is the same as in Fig. 1. The reference bars in the bottom part correspond to the main tungsten isotopes.

room temperature. Figure 1 shows the mass spectra recorded at two residual pressures, each comprising four peaks due to triply charged ions of the main tungsten isotopes (the corresponding reference mass-to-charge ratios M/q are indicated by vertical bars in the bottom part of the figure, with the bar length corresponding to the relative fraction of each isotope). The peaks (with the width and shape determined by the parameters of measurements) coincide exactly with the reference in positions and approximately in magnitudes. The latter fact was caused by the statistical scatter of isotope fractions and related to fluctuations in the number of particular isotopes, since the number of detected ions was relatively small. The room-temperature measurements were performed for two values of the residual pressure, 1.5×10^{-6} and 2.5×10^{-6} Torr. The corresponding spectra of W^{3+} ions (depicted in Fig. 1 by the dashed and solid line, respectively) show that the field evaporation rate in the latter case was approximately three times that in the former.

An increase in the temperature to 600 K leads to a general growth of the intensities of all W^{3+} peaks in the
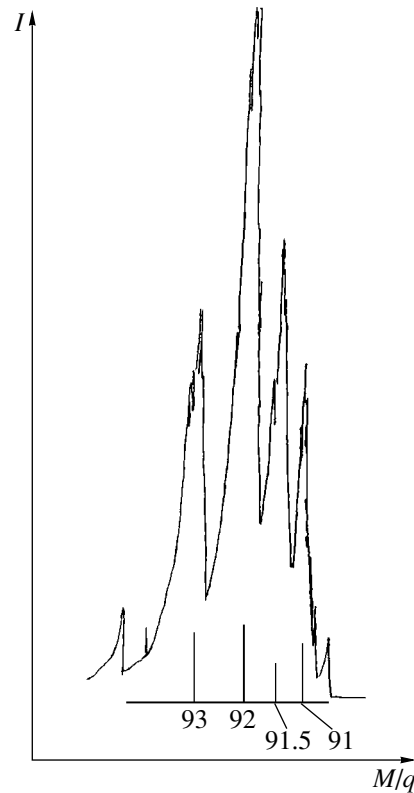
mass spectrum by a factor of 1.2–1.3. In addition, there appeared the peaks of W^{2+} ions (Fig. 2) showing a good correspondence with the M/q reference in positions and a large statistical scatter in isotope fractions. Note that the ordinate scale in Figs. 1 and 2 is the same, which implies that W^{2+} ions were quite clearly manifested at 600 K. Special search for singly charged ions W^{+} showed complete absence of the corresponding signals in the spectra recorded at both 300 and 600 K. In both cases, the W^{4+} ions with $M/q = 45$ were also not revealed in the spectra recorded with magnetic field sweep for the measurement of water ions. It should be noted that W^{4+} ions were practically always observed in the spectra measured at cryogenic temperatures and high field evaporation rates; the most intense peak always belonged to W^{3+} [4].

Thus, even a relatively small increase in the temperature (from 300 to 600 K) leads to a significant increase in the probability of double ionization of tungsten ions in the course of field evaporation. This result suggests two important conclusions. The role of activated overcoming of the potential barrier is still significant, despite considerable field strength (about 2×10^{8} V/cm). The content of water in the adlayer is sufficiently high, (probably due to a strong polarization of water molecules) even at 600 K, since the field of the intense evap-

oration of tungsten still remains low (rather than approaching the values typical of high vacuum).

As for the singly charged tungsten ions, they can be expected to appear at elevated temperatures inaccessible in our experiments. At such a high temperature, the field evaporation proceeds at a very high rate, the sample point exhibits rapid blunting, and the process terminates within a time shorter than that required for recording a mass spectrum.

The significant growth in the rate of field evaporation observed upon an increase in the water content in the residual atmosphere (Fig. 1) is evidence of a strong catalytic action of the polar molecules of water capable of weakening the internal W–W bonds. This effect can be used for increasing the intensity of the sources of refractory metal ions, the more so that such sources operate at much lower levels of the electric field strength.

REFERENCES

1. M. K. Miller and G. D. W. Smith, *Atom Probe Microanalysis: Principles and Applications to Material Problems* (Materials Research Society, Pittsburgh, 1989; Mir, Moscow, 1993).

2. H. D. Beckey, *Principles of Field Ionization and Field Desorption Mass Spectrometry* (Pergamon Press, Oxford, 1977).

3. N. M. Blashenkov, G. Ya. Lavrent'ev, and V. N. Shrednik, Pis'ma Zh. Tekh. Fiz. **17** (22), 30 (1991) [Sov. Tech. Phys. Lett. **17**, 796 (1991)].

4. M. V. Loginov and V. N. Shrednik, Pis'ma Zh. Tekh. Fiz. **24** (11), 45 (1998) [Tech. Phys. Lett. **24**, 432 (1998)].

Translated by P. Pozdeev

Silicon Passivated by Two-Layer Insulating Films of Ytterbium Oxide and Dysprosium Oxide

M. A. Rodionov[a], V. A. Rozhkov[a,*], and A. V. Pashin[b]

[a] Samara State University, Samara, Russia
[b] Samara State Academy of Building and Architecture, Samara, Russia
* e-mail: rozhkov@ssu.samara.ru
Received January 13, 2004

Abstract—We have studied the recombination properties of silicon passivated by two-layer insulating films of ytterbium oxide and dysprosium oxide. After deposition of such a two-layer coating of rare earth element (REE) oxides, the effective lifetime of nonequilibrium charge carriers, measured by the method of nonstationary photoconductivity relaxation, is two to three times the initial value. The rates of the surface recombination of charge carriers at the silicon–REE oxide interface have been determined. Two-layer insulating films of REE oxides are promising passivating coatings for semiconductor devices and integrations. © 2004 MAIK "Nauka/Interperiodica".

Modern microelectronics widely uses semiconductor devices and integrated circuits with elements based on the metal–insulator–semiconductor (MIS) type structures. This is related primarily to the simple design of MIS devices and a relatively high packing density of elements in the integrations. The insulating layer in MIS devices has to meet stringent requirements, the main of which are a high electric strength, small leak currents, stability to external factors, and the possibility of obtaining semiconductor–insulator interfaces with low recombination losses.

The group of promising dielectric materials suitable for the formation of insulating layers in MIS devices includes rare earth element (REE) oxides. These compounds are characterized by high chemical and thermal stability; large dielectric permittivities ($\varepsilon = 8$–20), resistivities ($\rho = 10^{13}$–$10^{16} \, \Omega$ cm), and breakdown voltages; and good adhesion to the silicon surface. In addition, REE oxides admit the formation of two-layer insulating films [1] ensuring improved electrical stability of devices. However, the recombination characteristics of silicon surfaces coated with two-layer REE oxide films still remain unstudied.

The aim of this study was to determine the effective lifetime and the surface recombination rate of nonequilibrium charge carriers in silicon plates passivated by two-layer insulating films made of ytterbium oxide and dysprosium oxide.

The substrates were cut from (100)-oriented polished single crystal silicon wafers (KEF-20 grade) and had the dimensions $10 \times 5 \times 0.36$ mm. Prior to REE oxide deposition, some of the silicon substrates were only rinsed for 10 min in acetone, while the other samples were deprived of natural oxide by etching in an aqueous solution of hydrofluoric acid (HF–H_2O, 1 : 10)

and some of these samples were then boiled in a hydrogen peroxide–ammonia–water (1 : 1 : 3) mixture. After each treatment, the substrates were repeatedly rinsed in doubly distilled water and dried on filter paper.

The two-layer films of rare earth metals were formed on both sides of silicon substrates by thermal deposition in vacuum. The metals were evaporated from a molybdenum crucible in a residual vacuum of $(2$–$3) \times 10^{-5}$ Torr (VUP-5 vacuum system). Each substrate surface was sequentially coated with ytterbium and dysprosium. Then, the two-layer films were oxidized in a tubular muffle furnace (SUOL-0.4.4) in air for 40 min at 620°C. Finally, the ohmic contacts were formed by vacuum deposition of dysprosium and aluminum pads via masks.

The effective lifetime τ_{ef} of charge carriers was determined by the conventional method of nonstationary pho-
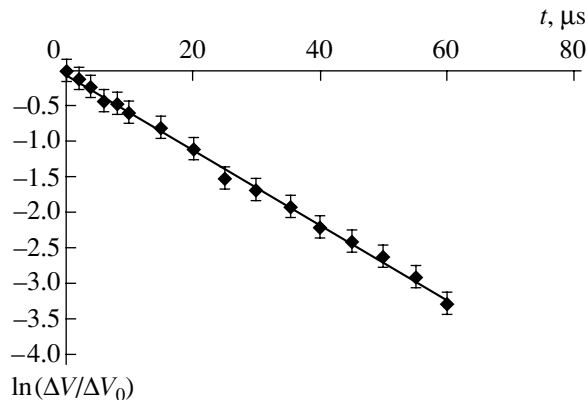

Fig. 1. Kinetics of the relative voltage drop across a sample after switching off the illumination.

toconductivity on samples illuminated by rectangular pulses of light. The method of measurements and the experimental setup were described elsewhere [2]. As is known, the effective carrier lifetime is determined by the joint action of recombination and trapping centers on the surface and in the bulk of semiconductor. The presence of additional charge carrier traps may significantly influence the measured characteristic time of photoconductivity decay. As a result, the effective carrier lifetimes determined using the nonstationary photoconductivity technique exceeds real values. In order to elucidate the role of surface trapping processes on the relaxation of photoconductivity, we studied the kinetics of voltage drop across the sample after switching off the light, which is determined by the recombination of nonequilibrium charge carriers. The results of these measurements were plotted as $\Delta V(t) = V_0 - V(t)$, where V_0 is the equilibrium voltage drop and $V(t)$ is that in the presence of nonequilibrium charge carriers.

Figure 1 shows the plot of $\ln\dfrac{\Delta V(t)}{\Delta V_0}$ versus time (ΔV_0 is the maximum value of ΔV) for a sample passivated by a two-layer insulating film of ytterbium oxide and dysprosium oxide. As can be seen, the plot is rectified in the semilogarithmic coordinates. This result indicates that the process of photoconductivity relaxation is described by a single exponent and determined by the carrier generation–relaxation processes, while the trapping of nonequilibrium carriers at the silicon–REE oxide interfaces can be ignored. The effective lifetime of nonequilibrium charge carriers in thin samples with a relatively low rate of the surface recombination is described by the relation [4]

$$\frac{1}{\tau_{\text{ef}}} = \frac{1}{\tau_0} + \frac{2S}{d},$$

where τ_0 is the lifetime of nonequilibrium charge carriers in the bulk of silicon, d is the sample thickness, and S is the surface recombination rate. Using this equation, the surface recombination rate can be evaluated from the photoconductivity kinetics if the bulk carrier lifetime is known.

For determining the bulk carrier lifetime, we used the dependence of the effective lifetime of nonequilibrium charge carriers on the sample thickness. Figure 2 shows such plots constructed using the τ_{ef} values measured for the samples of various thickness prepared by etching silicon substrates in a standard etchant (SR-8). As can be seen, the experimental data are well rectified in the $1/\tau_{\text{ef}}$ versus $1/d$ coordinates. This result is indicative of a constant rate of surface recombination in samples of various thicknesses. The bulk carrier lifetimes evaluated from these experimental data were $\tau_0 \geq 200\ \mu s$ for all samples studied.

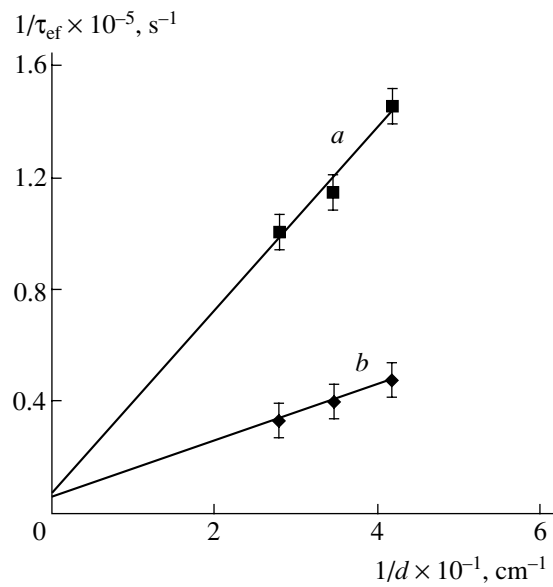The surface recombination rate was evaluated using measured values of the effective lifetime of nonequilib-

Fig. 2. Plots of the effective lifetime of nonequilibrium charge carriers versus thickness of silicon samples (*a*) with a real surface and (*b*) passivated with a two-layer Yb_2O_3–Dy_2O_3 film.

rium charge carriers. The measured values of τ_{ef} did not exceed 38 μs and obeyed the condition $1/\tau_{\text{ef}} \gg 1/\tau_0$, which allowed the term $1/\tau_0$ in relation (1) to be ignored. The values of the surface recombination rate S and effective lifetime τ_{ef} of nonequilibrium charge carriers determined for differently pretreated silicon samples measured before and after the REE oxide film deposition are presented in the table.

Analysis of the results shows that deposition of the REE oxide films increases the effective lifetime of nonequilibrium charge carriers and decreases the surface recombination rate. As can be seen from the comparative data, the S value in the Si–Yb_2O_3–Dy_2O_3 structure

Surface recombination rates S and effective lifetimes τ_{ef} of nonequilibrium charge carriers in silicon samples differently treated before and after passivation by two-layer REE oxide films

Coating material	Silicon surface pretreatment	τ_{ef}, μs	S, cm/s
Uncoated	HF:H$_2$O	8–10	2250–1800
"	HF:H$_2$O + H$_2$O$_2$:NH$_4$:H$_2$O	10–12	1800–1500
"	Ultrasonic rinsing	10–12	1800–1500
Yb$_2$O$_3$–Dy$_2$O$_3$	HF:H$_2$O	33–36	540–500
"	HF:H$_2$O + H$_2$O$_2$:NH$_4$:H$_2$O	35–38	510–470
"	Ultrasonic rinsing	28–30	640–600

is one to two orders of magnitude lower than the corresponding values in Si–SiO$_2$ and Si–SiO$_2$–Si$_3$N$_4$ structures, widely used in semiconductor electronics [5, 6].

Thus, the results of our investigation show the high efficiency and good prospects of using two-layer insulating films of REE oxides as passivating coatings for silicon-based devices and elements of integrated circuits.

REFERENCES

1. M. A. Rodionov, in *Proceedings of the 5th All-Russian Conference of Young Scientists on the Physics of Semiconductors and Semiconductor Opto- and Nanoelectronics, St. Petersburg, 2003*, p. 111.

2. V. A. Rozhkov and M. A. Rodionov, in *Proceedings of the 2nd International Scientific–Technological Conference "Physics and Engineering Applications of Wave Processes," Samara, 2003*, pp. 358–361.

3. A. L. Fahrenbruch and R. H. Bube, *Fundamentals of Solar Cells* (Academic Press, New York, 1987; Énergoatommash, Moscow, 1987).

4. A. V. Rzhanov, *Electronic Processes on Semiconductor Surfaces* (Nauka, Moscow, 1971).

5. V. G. Litovchenko and A. P. Gorban', *Fundamental Physics of Microelectronic MIS Systems* (Naukova Dumka, Kiev, 1978).

6. A. V. Sachenko, B. A. Novominskiĭ, and A. S. Kalshabekov, in *Proceedings of the 12th All-Union Scientific Conference on Microelectronics, Tbilisi, 1987*, Part 3, p. 143.

Translated by P. Pozdeev

Measuring the Polarization Characteristics
of Birefringent Optical Fibers Using an Interference Technique

O. I. Kotov*, L. B. Liokumovich, A. V. Medvedev,
S. I. Markov, and A. V. Khlybov

St. Petersburg State Technical University, St. Petersburg, 195251 Russia
* e-mail: kotov@radio.rphf.spbstu.ru*
Received January 20, 2004

Abstract—A simple method based on the interference of coherently excited modes is proposed for measuring the orientations of birefringence axes and determining the level of polarized mode excitation in single-mode birefringent fibers. The exact determination of these characteristics is achieved by introducing the dimensionless coefficients of modulation and transmission dependent on the analyzer rotation angle. The proposed technique, in contrast to the conventional methods, does not require the use of special excitation conditions at the fiber entrance. © 2004 MAIK "Nauka/Interperiodica".

Introduction. The use of single-mode birefringent fibers in optical systems requires exact control of the polarization parameters and angular matching of the optical axes of fiber elements. The most frequently used fibers of this type are characterized by linear birefringence, whereby the directions of optical axes correspond to the orientations of two orthogonal linearly polarized eigenmodes.

Relatively simple methods of the control and determination of the polarization parameters of fiber elements are based on the measurements of the intensity of light past the exit polarizer (analyzer) or the rotating polarizer [1–3]. Such measurements usually stipulate using special types of fiber excitation by a polarized light, need for control of the phase difference between the polarized modes, and require some other conditions. Since such conditions are difficult to meet, the application of these methods encounters problems and does not provide for the determination of parameters with desired accuracy. Takada *et al.* [4] proposed a high-precision system of angular matching for the joints of birefringent fibers based on an external Michelson interferometer and a low-coherent light source. These methods do not use the wide possibilities offered by interference techniques using coherent light sources.

This Letter presents a simple but highly precise method of determination of the polarization characteristics of optical fibers, which is based on the interference measurements. Physically analogous interference effects, known in crystal optics for anisotropic plates illuminated by a polarized light, are used in polariscopes [5].

The proposed method stipulates excitation of the fiber by an arbitrarily polarized coherent radiation, transmission of the output radiation through an analyzer to a photodetector, an auxiliary thermal action upon a certain region of the fiber, and an analysis of the dependence of the output signal on the analyzer angle.

Theoretical analysis. Let a polarized coherent radiation to enter a linearly birefringent optical fiber. In the general case, the elliptically polarized radiation can be expanded into a sum of two linearly polarized components (E_X, E_Y) oriented along the fiber birefringence axes X and Y and represented as the Jones vector [1, 6, 7],

$$\mathbf{E}_1 = \begin{pmatrix} \dot{E}_{mX} \\ \dot{E}_{mY} \end{pmatrix} = E_0 \begin{pmatrix} \cos(\alpha) e^{j\varphi} \\ \sin(\alpha) \end{pmatrix}, \qquad (1)$$

where E_0 is the wave amplitude. The parameters α and φ reflect the amplitude ratio and the phase difference of the components E_X and E_Y, thus determining the polarization state. For example, zero phase difference ($\varphi = 0$) corresponds to the case of linear polarization at an angle α relative to the X axis. The case of $\alpha = \pi/4$ and $\varphi = \pi/2$ corresponds to a circularly polarized light.

With neglect of the optical losses, excitation of the fiber by the incident radiation is described by the Jones matrix

$$\mathbf{T}_1 = \begin{pmatrix} e^{-\frac{i\gamma}{2}} & 0 \\ 0 & e^{\frac{i\gamma}{2}} \end{pmatrix}, \qquad (2)$$

where γ is the phase difference acquired by the polarized modes upon traveling through the fiber. The ratio of intensities P_X and P_Y of the polarized modes excited in the fiber depends on the α angle as

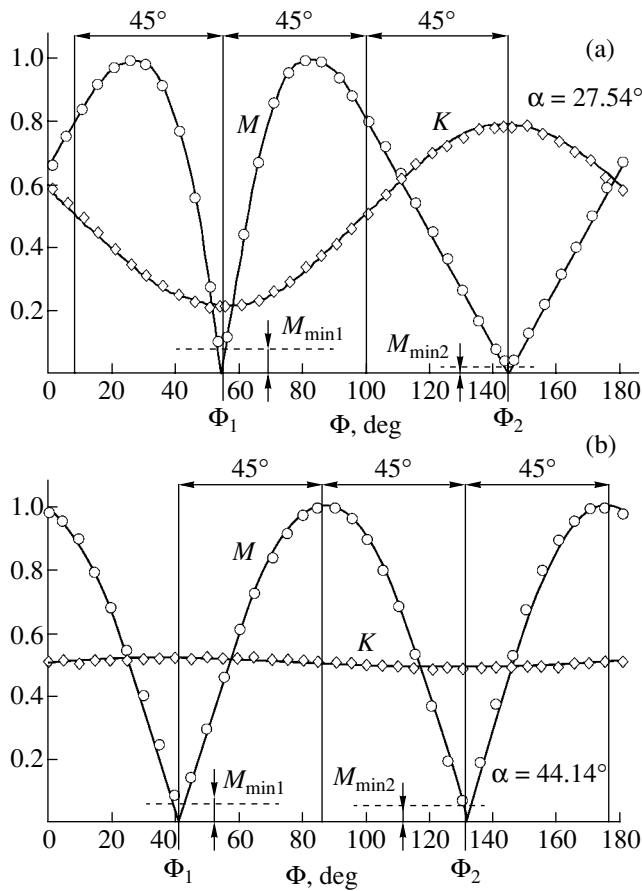$$k = \frac{P_X}{P_Y} = \tan^2(\alpha). \qquad (3)$$

Fig. 1. Experimentally measured (symbols) and calculated (solid curves) $K(\Phi)$ and $M(\Phi)$ functions.

The phase difference between modes at the fiber exit corresponds to the sum $\gamma + \varphi$.

Having traveled through the anisotropic fiber, the radiation enters the linear polarizer (analyzer) oriented at a certain angle Φ. The analyzer matrix has the following form:

$$\mathbf{T}_2 = \begin{pmatrix} \cos^2(\Phi) & \cos(\Phi)\sin(\Phi) \\ \cos(\Phi)\sin(\Phi) & \sin^2(\Phi) \end{pmatrix}. \qquad (4)$$

An expression for the radiation intensity at the fiber output can be obtained using the standard Jones formalism by multiplying matrices $\mathbf{T}_2$ and $\mathbf{T}_1$ by vector $\mathbf{E}_1$ and taking the square modulus of the resulting vector:

$$I = E_0^2\{\cos^2(\Phi)\sin^2(2\Phi) + \cos^2(\alpha)\cos^4(\Phi)$$
$$+ \sin^2(\alpha)\sin^4(\Phi) + 0.5\sin(2\alpha)\sin(2\Phi)\cos(\gamma + \varphi)\}. \qquad (5)$$

This expression shows that external factors (temperature, pressure, mechanical perturbations) acting upon the fiber modulate γ and, hence, the measured intensity I. As a result, the intensity varies from the minimum value $I_{\min}$ (for $\cos(\gamma + \varphi) = -1$) to the maxi-

mum $I_{\max}$ (for $\cos(\gamma + \varphi) = 1$). The angle Φ in expression (5) is measured relative to the X axis.

Let us introduce two coefficients independent of the light intensity and the phase difference γ (which is difficult to monitor and stabilize). The first is the transmission coefficient K defined as

$$K = \frac{I_{\max} + I_{\min}}{2I_{av}} = \sin^2(\Phi)\cos^2(\Phi)$$
$$+ \cos^2(\alpha)\cos^4(\Phi) + \sin^2(\alpha)\sin^4(\Phi), \qquad (6)$$

where $I_{av} = \langle(I_{\max} + I_{\min})\rangle$ is the average value of the sum $I_{\max} + I_{\min}$ determined for all angles Φ. The second coefficient, M, has the meaning of the depth of modulation of the output light intensity by an additional action upon the fiber:

$$M = \frac{I_{\max} - I_{\min}}{I_{\max} + I_{\min}}$$
$$= \left| \frac{\sin(2\alpha)\sin(2\Phi)}{2(\cos^2(\Phi)\sin^2(\Phi) + \cos^2(\alpha)\cos^4(\Phi) + \sin^2(\alpha)\sin^4(\Phi))} \right|. \qquad (7)$$

In contrast to K, the modulation coefficient M takes into account the result of interference of the polarized modes during their passage through the analyzer.

Figure 1 presents examples (solid curves) of the functions $K(\Phi)$ and $M(\Phi)$, where the axis Φ plots fixed values of the analyzer angle in the experiments described below. The function $M(\Phi)$ contains information about the polarization parameters and excitation of the fiber element. The minima of expression (7) where $M(\Phi) = 0$ correspond to the angles Φ_1 and Φ_2 corresponding to the directions of the birefringence axes at the fiber exit relative to the analyzer scale. In the general case, the shape of the $M(\Phi)$ curve is asymmetric and depends on the ratio of intensities of the polarized modes (k) and the angle α. When α deviates from $\pi/4$, the maxima of $M(\Phi)$ shift from the middle of the interval between Φ_1 and Φ_2 toward the axis corresponding to the mode of lower intensity. Using the function $K(\Phi)$, it is also possible to evaluate the above parameters. The positions of the extrema ($K_{\max}$ and $K_{\min}$) correspond to directions of the optical axes of the fiber, while the ratio of $K_{\max}$ and $K_{\min}$ determines the value of k.

Expressions (6) and (7) do not reflect the phenomenon of mode coupling accompanied by the pumping of power from one polarized mode to another [2, 8]. This factor can play a significant role and is described by the extinction coefficient η defined as

$$\eta = \frac{P_X}{P_{(X \to Y)}} = \frac{P_Y}{P_{(Y \to X)}}, \qquad (8)$$

where $P_{(X \to Y)}$ and $P_{(Y \to X)}$ are the values of power pumped from X to Y and vice versa. An analysis taking

into account the mode coupling shows that this effect is most clearly manifested in that the minima M_{min1} and M_{min2} of expression (7) differ from zero.

A more thorough analysis and comparison of the functions $K(\Phi)$ and $M(\Phi)$, including the possibility of determining the extinction coefficient η from the $M(\Phi)$ curve, will be considered in a separate paper.

Experimental results. The experiments were performed on a setup (Fig. 2) making it possible to measure the functions $K(\Phi)$ and $M(\Phi)$. A coherent radiation source excited the fiber entrance by completely polarized light in an arbitrary (but fixed) polarization state. Some experiments were performed with a linearly polarized radiation in order to control the ratio of intensities of the polarized modes in the fiber. The initial 5- to 10-cm-long part of the fiber was subjected to additional thermal action (heating by $\Delta T = 10$–15 K). The regime of heating was selected so as to provide for a change in the phase difference between the polarized modes by more than π, which allowed the observation of I_{max} and I_{min}. The analyzer mounted in a rotary device was set at a certain angle in the $[0, \pi]$ interval.

For a preset angle Φ of the analyzer, the thermal action induced oscillations of the light intensity between I_{min} and I_{max} at the photodetector input. The corresponding values of the minimum (U_{min}) and maximum (U_{max}) output voltage for the given value of Φ were measured by a voltmeter. Using these data, the coefficients M and K were calculated by the formulas

$$M = \frac{U_{max} - U_{min}}{U_{max} + U_{min}}, \quad K = \frac{U_{max} + U_{min}}{2U_{av}},$$

equivalent to expressions (6) and (7). The value of U_{av} was determined as the average of the sum $U_{max} + U_{min}$ for all angles Φ.

The results of experimental measurements of the functions $K(\Phi)$ and $M(\Phi)$ for two single-mode birefringent fibers with a length of $l \approx 1.5$ m excited in different regimes are presented by symbols (circles and rhombs) in Fig. 1. The parameters of calculated curves (α and the shift along the Φ axis) were obtained by approximating the experimental plots in terms of expression (7) with minimum rms deviation. As can be seen from Fig. 1, the
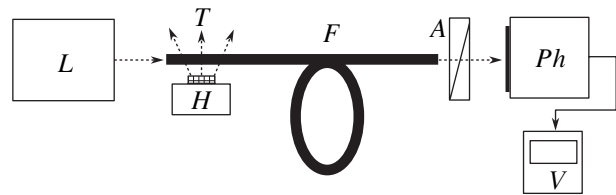

Fig. 2. Schematic diagram of the experimental setup: (*L*) laser; (*H*) heater; (*F*) fiber; (*A*) analyzer; (*Ph*) photodetector; (*V*) voltmeter.

experimental data are well described by the calculated curves.

Conclusions. The main features of the proposed approach to experimental determination of the polarization characteristics of birefringent optical fiber elements with the use of interference measurements are as follows:

(i) The measurements stipulate the use of a coherent radiation source.

(ii) These is no need to ensure excitation of one of the polarized modes at the fiber entrance.

(iii) The angular positions of optical axes of the fiber are determined by sharply varying portions of the experimental $M(\Phi)$ curve, which increases the accuracy of determination.

REFERENCES

1. R. M. Azzam and N. M. Bashara, *Ellipsometry and Polarized Light* (North-Holland, Amsterdam, 1977; Mir, Moscow, 1981).
2. O. Sezerman and G. Best, *Accurate Alignment Preserves Polarization*, Laser Focus World, 1997; http://www.ozoptics.com.
3. S. L. A. Carrara, Proc. SPIE **1267**, 24 (1990).
4. Kazumasa Takada, Kazunori Chida, and Juichi Noda, Appl. Opt. **26**, 2979 (1987).
5. M. Born and E. Wolf, *Principles of Optics*, 4th ed. (Pergamon Press, Oxford, 1969; Nauka, Moscow, 1973).
6. A. Yariv and P. Yeh, *Optical Waves in Crystals: Propagation and Control of Laser Radiation* (Wiley, New York, 1984; Mir, Moscow, 1987).
7. V. Ya. Molchanov and G. V. Skrotskiĭ, Kvantovaya Élektron. (Moscow), No. 4, 3 (1971).
8. S. C. Rashleigh, W. K. Burns, and R. P. Moeller, Opt. Lett. **7**, 40 (1982).

Translated by P. Pozdeev

The Effect of Optical Radiation on the Semiconductor Conductivity in a Thin-Film Ferroelectric–Semiconductor Structure

V. P. Afanas'ev[a,*], D. Yu. Bulat[a], E. Yu. Kaptelov[b], and I. P. Pronin[b]

[a] St. Petersburg State Electrotechnical University, St. Petersburg, 197376 Russia
[b] Ioffe Physicotechnical Institute, Russian Academy of Sciences, St. Petersburg, 194021 Russia
* e-mail: VPAfanaesiev@mail.eltech.ru
Received January 16, 2004

Abstract—We have studied the effect of optical radiation on the conductivity of a thin-film field-effect transistor based on a multilayer structure of the $Si–SiO_2–Pt–PZT–SnO_{2-x}–Pt$ type. Within the permissible radiation dose, the conducting channel exhibits a residual photoconductivity, with an optical data storage time of no less than 10^5 s. The effective quenching of the residual conductivity in the structure studied can be produced only by simultaneous action of an alternating electric field and the temperature. © *2004 MAIK "Nauka/Interperiodica".*

An approach based on physical integration principles opens new prospects in the development of elements and devices for functional electronics. Among the base materials ensuring the progress in this direction, an important role belongs to ferroelectrics—materials possessing a unique combination of insulating, pyroelectric, piezoelectric, and optical properties. By combining the properties of ferroelectrics and semiconductors in thin-film heterostructures, it is possible to create various functional elements whose characteristics can change under the action of a polarizing electric field or radiation.

Using such ferroelectric–semiconductor structures, it is possible to develop rewritable nonvolatile memory (NVFRAM) devices [1] as well as photo- and pyroelectric radiation detectors with adaptive characteristics [2]. Despite the obvious potential advantages of such structures, considerable technological difficulties encountered in their fabrication (related to the physicochemical compatibility of layers) still hinder the creation of thin-film ferroelectric–semiconductor systems admitting effective control and possessing stable reproducible characteristics [3–7]. Numerous variants of the transistor structures with ferroelectric gates obtained by depositing a ferroelectric film onto a silicon substrate [1, 3, 4] or by combining ferroelectric and semiconductor films [5, 6, 7] still do not provide the anticipated results. Analysis of the prior art showed that the main difficulties hindering the use of ferroelectric–semiconductor structures are related to the properties of interfaces.

We have determined the effect of optical radiation on the residual photoconductivity of a semiconducting resistor and studied the possibility of effective quenching of the residual conductivity in thin-film ferroelectric–semiconductor (lead zirconate titanate–tin dioxide) structures.

The choice of the ferroelectric–semiconductor pair capable of providing for the maximum response to optical and electrical factors was determined both by the physical properties of component materials and by their technological compatibility from the standpoint of thin-film structure fabrication. For operation under standard conditions, it is expedient to use wide-bandgap semiconductors. Among these, the maximum efficiency was exhibited by tin dioxide (SnO_{2-x}) [2], which is related to the fact that this material can be deposited in an oxygen-containing medium directly onto preliminarily formed lead zirconate titanate (PZT) layers. Other advantages of SnO_{2-x} films are good technological properties, stability, resistance to chemical and mechanical factors, and large value of the bandgap width (3.2–3.7 eV, depending on the charge carrier density) ensuring sensitivity in the UV spectral range. As is known, the charge carrier density in SnO_{2-x} can be controlled within broad limits by varying the degree of nonstoichiometry of the deposit formed in the course of ion-plasma sputtering of a tin target in an oxygen-containing atmosphere. In this way, SnO_{2-x} films with a surface resistance of 2–10 kΩ and a thickness of 100–120 nm were obtained, which provide for an effective control over thin-film ferroelectric–semiconductor structures [2].

The composition of PZT films ($PbZr_{0.54}Ti_{0.46}O_3$) corresponded to a morphotropic phase boundary separating the regions of tetragonal and rhombohedral ferroelectric phases. In this region, this ferroelectric is characterized by high residual polarizations and low coercive fields. The PZT films with thicknesses up to 1 μm were obtained by RF magnetron sputtering of the
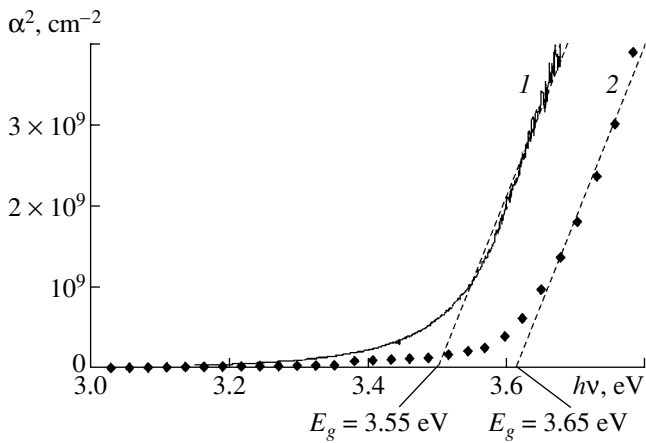
Fig. 1. Plots of the optical absorption coefficient α^2 versus incident photon energy for PZT films: (*1*) $PbZr_{0.54}Ti_{0.46}O_3$ (this study); (*2*) $PbZr_{0.6}Ti_{0.4}O_3$ [10].
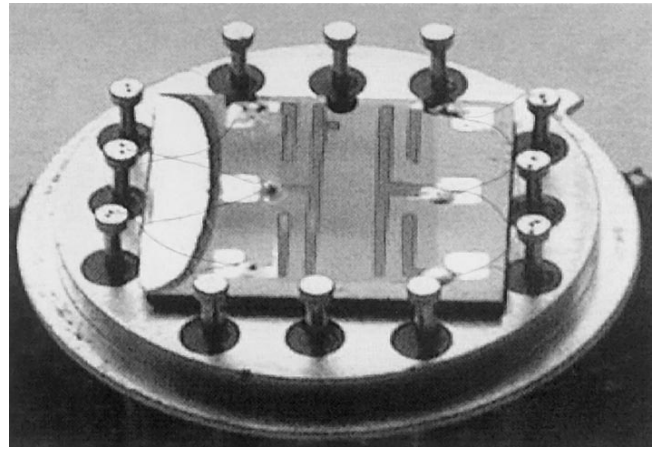

Fig. 2. The prototype package with a silicon substrate bearing four thin-film transistors based on a ferroelectric–semiconductor structure with a common gate electrode.

corresponding ceramic targets [7–9]. The sputtered material was deposited onto silicon substrates with preliminarily formed platinum control electrodes. The optical bandgap width of these PZT films determined from the transmission spectrum amounted to 3.55 eV (Fig. 1), which implies that the PZT and SnO_{2-x} films in the structures studied exhibit fundamental absorption in the same spectral range.

Films of platinum (Pt) with thicknesses within 80–120 nm, used as the bottom control (gate) electrode and the electrodes of a semiconducting resistor, were deposited by ion-plasma sputtering as described elsewhere [8]. Figure 2 shows the configuration of a silicon substrate bearing four thin-film transistors with a common gate electrode. The substrate with transistors was mounted on a base and covered with a lid having a transparent sapphire window.

The conductivity of the semiconducting resistor was controlled by varying the magnitude and direction of a residual polarization produced in the ferroelectric film by voltage pulses of alternating polarity. The field interaction between the surface charge of the ferroelectric and the charge carriers in the semiconductor film led to either depletion or enrichment of the near-surface region of the semiconductor (Fig. 3), with the corresponding change in conductivity of the resistor. According to published data [5–7], the effective operation of such structures is directly related to a partial screening of the polarization by charges localized on the surface states at the ferroelectric–semiconductor interface. As a result, the change in the conductivity is significantly lower than expected. In addition, the conductivity established after polarization exhibits a drift with time [3–6].

A variant of the sample structure (Fig. 2) with a SnO_{2-x} thin-film resistor formed on the surface of the PZT layer provided for a substantial increase in the efficiency of electric control. This is probably explained by

a significant decrease in the density of surface states at the ferroelectric–semiconductor interface. The results of measurements showed that the resistance exhibited a 20-fold variation in response to the electric-field switching of the PZT layer and the established levels of resistance were stable in time. Therefore, it was of interest to study the effect of optical radiation on the conductivity of the semiconducting resistor. Apparently, $PZT–SnO_{2-x}$ structures can be used for the development of UV dose meters operating in a wavelength range of 310–360 nm [2, 11].

The high sensitivity and residual photoconductivity of the thin-film transistor were observed only in the
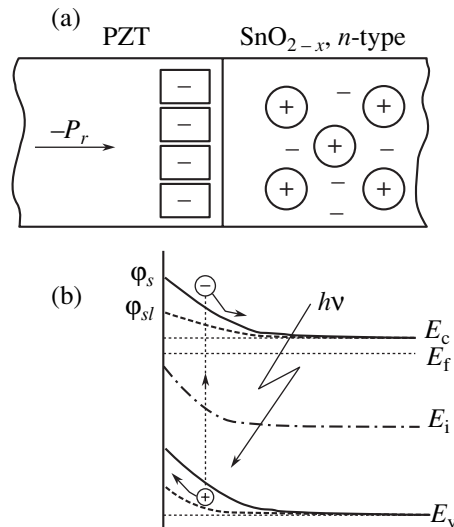

Fig. 3. Schematic diagrams of (a) a ferroelectric–semiconductor structure and (b) the energy band structure of a SnO_{2-x} film in the state of depletion before and after UV irradiation.
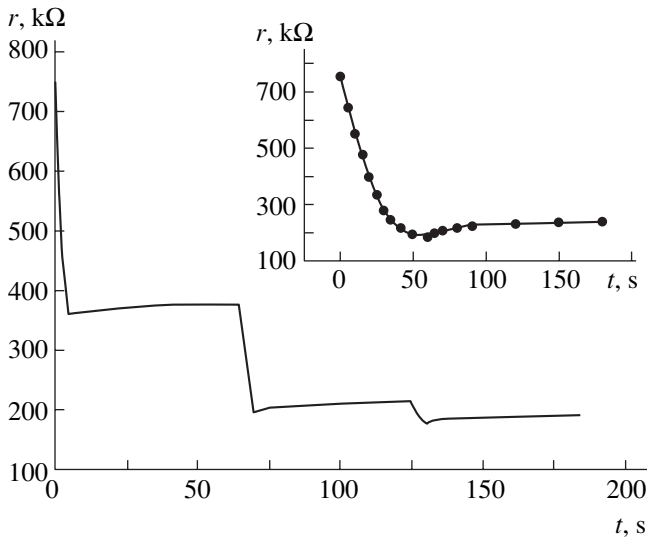
Fig. 4. Time variation of the resistance of a thin-film semiconducting resistor on the surface of a ferroelectric film under the action of three 5-s pulses of radiation. The inset shows variation of the resistance during a 60-s continuous exposure to the same source.

state of semiconductor depletion induced by applying a negative voltage to the transistor gate (Fig. 3). The principle of operation of a ferroelectric–semiconductor structure with photomemory is based upon the fact that the UV radiation absorbed in the SnO_{2-x} film generates charge carriers, which are separated in the field of the surface polarization charge of PZT. As the radiation dose increases, the density of holes at the ferroelectric–semiconductor interface grows, while the barrier height drops (Fig. 3). Obviously, the phenomenon of residual photoconductivity is observed when the radiation dose is restricted to a level admitting the existence of a recombination barrier ensuring separation of the non-equilibrium charge carriers and their anomalously long lifetime.

Residual conductivity quenching by DC and AC polarizing voltage (resistance after exposure, 250 kΩ)

AC voltage frequency, Hz	AC voltage amplitude, V	Quenching time, min	Dose meter resistance, kΩ
50	14	120	450
100	14	90	580
200	14	60	655
300	14	50	700
400	14	30	730
500		20	750
	DC voltage amplitude		
	10	150	380
	12	150	420

Figure 4 shows variation of the resistance of a thin-film resistor (i.e., the transistor channel) under the action of three 5-s pulses of radiation corresponding to a total dose of 30 J/m^2. As can be seen, the height of the recombination barrier within this dose range is retained on a sufficiently high level, ensuring optical data storage for a long time (the characteristic time of relaxation of the residual photoconductivity is 10^5 s). When the structure is exposed to radiation of a low-intensity source, the time variation of the resistance is close to linear. Accumulation of the dose leads to a deviation from linearity as a result of a decrease in the size of the space charge region featuring separation of the generated charge carriers. For large radiation doses (60-s exposure to the same source) the time variation of resistance becomes substantially nonlinear and the recombination barrier height decreases to such a low level that, after switching off the radiation source, the resistance established during the exposure (see the inset in Fig. 4) exhibits a certain relaxation (increase). It should be noted that a slight increase in the resistance after termination of the exposure is also observed for the permissible radiation doses. This is probably related to a small heating of the thin-film resistor by radiation of the mercury lamp and by recombination of the nonequilibrium charge carriers in the near-surface region of the semiconductor free of the electric field generated by the polarization charge of PZT.

A necessary condition for the dose meter operation is the possibility of performing multiply repeated measurements of the radiation dose, which implies the need for effective quenching of the residual photoconductivity in the ferroelectric–semiconductor structures under consideration. Previously [2], we erased the optical data by applying two polarizing voltage pulses of the opposite polarity. The first pulse switched a semiconductor to the state of enrichment and eliminated the recombination barrier, which led to recombination of the charge carriers. The second pulse restored the state of depletion, after which optical signals could be recorded once again.

In the thin-film structures under consideration, the residual photoconductivity could not be completely quenched in this way, especially after prolonged exposures. This is probably related to the partial pinning of charge carriers on deep traps. The residual photoconductivity can be quenched only by applying an alternating voltage producing heating of the structure (see table). This action favors escape of the charge carriers from the deep traps and return of the thin-film resistor to the initial high-ohmic state (~750 kΩ). As can be seen from the data in the table, the efficiency of quenching increases with the frequency of applied erasing voltage at a constant amplitude.

In conclusion, we have demonstrated that a thin-film transistor structure of the ferroelectric–semiconductor type exhibits a residual photoconductivity under irradiation within a permissible dose range. Integration of the

optical action allows this phenomenon to be used for measuring the radiation doses, counting laser pulses, and in some other applications. However, the effective quenching of the residual conductivity in the structure studied is possible only by simultaneous action of an alternating electric field and the temperature. In order to eliminate this disadvantage, it necessary to perform additional investigation of the behavior of a screening charge formed at the ferroelectric–semiconductor interface.

REFERENCES

1. K. Aizawa, T. Okamoto, E. Tokumitsu, *et al.*, Integr. Ferroelectr. **15**, 245 (1997).

2. V. P. Afanasjev and G. P. Kramar, Ferroelectrics **143**, 299 (1993).

3. E. Tokumitsu, T. Shimamura, and H. Ishiwara, Integr. Ferroelectr. **15**, 137 (1997).

4. M. Noda, Y. Sugiyama, and M. Okuyama, Jpn. J. Appl. Phys. **34**, 5254 (1995).

5. I. A. Veselovskiĭ, I. V. Grekhov, L. A. Delimova, and I. A. Linichuk, Pis'ma Zh. Tekh. Fiz. **27** (1), 39 (2001) [Tech. Phys. Lett. **27**, 17 (2001)].

6. C. H. Seager, D. C. McIntyre, W. L. Warren, *et al.*, Appl. Phys. Lett. **68**, 2660 (1996).

7. J. T. Evans, R. I. Suizu, and L. L. Boyer, Appl. Surf. Sci. **117**–**118**, 413 (1997).

8. V. P. Afanas'ev, S. V. Bogachev, N. V. Zaĭtseva, *et al.*, Zh. Tekh. Fiz. **66** (6), 160 (1996) [Tech. Phys. **41**, 607 (1996)].

9. I. P. Pronin, E. Yu. Kaptelov, E. A. Tarakanov, *et al.*, Integr. Ferroelectr. **49**, 285 (2002).

10. C. H. Peng, J.-F. Chang, and S. B. Desu, Mater. Res. Soc. Symp. Proc. **243**, 21 (1992).

11. V. P. Afanasjev, A. V. Pankrashkin, G. Suchaneck, *et al.*, in *Proceedings of the International Conference "Sensors and Systems," St. Petersburg, 2002*, Vol. 1, pp. 52–56.

Translated by P. Pozdeev

Frequency-Selective Josephson Detector: Power Dynamic Range at Subterahertz Frequencies

V. V. Shirotov* and Yu. Ya. Divin

Institute of Radio Engineering and Electronics, Russian Academy of Sciences, Moscow, Russia
* e-mail: votoriw@mail.ru
Received December 10, 2003

Abstract—The power dynamic range of an $YBa_2Cu_3O_{7-x}$ frequency-selective Josephson detector for the Hilbert-transform spectroscopy was experimentally studied in the subterahertz frequency range. At a temperature of 80 K, the dynamic range of 2×10^5 was achieved at a noise equivalent power of 8×10^{-15} W/Hz$^{1/2}$. © 2004 MAIK "Nauka/Interperiodica".

In recent years, high-power subterahertz and terahertz radiation sources operating in the pulse mode have appeared in various fields of physics [1–3]. In the analysis of radiation generated by such sources, Hilbert-transform spectroscopy [4] using an $YBa_2Cu_3O_{7-x}$ frequency-selective Josephson detector [5] possessing a small time constant, broad working frequency range, and high sensitivity may be advantageous to the use of traditional detectors and spectrometers. However, practical realization of these possibilities requires the knowledge of the dynamic range of this detector with respect to the input radiation power.

Previously, only qualitative estimations of the dynamic range were presented for Josephson detectors of various types [6, Ch. 23]. In this paper, we propose a new qualitative criterion for evaluation of the dynamic range of an $YBa_2Cu_3O_{7-x}$ frequency-selective Josephson detector, which takes into account special features of the use of such detectors in the Hilbert-transform spectroscopy. We also present the results of experimental investigations in the subterahertz frequency range at liquid nitrogen temperatures.

The dynamic range of a detector is defined as the ratio $\Delta = P_s/P_0$, where P_s is the top limit for which the detector response deviates from linearity and P_0 is the bottom limit determined by the noise equivalent power (*NEP*) and the frequency band ΔF of the detection system: $P_0 = NEP\Delta F^{1/2}$. Using expressions for the detector response and intrinsic noise obtained within the framework of the resistive shunted junction model [6], the *NEP* of a frequency-selective Josephson detector (normalized to the absorbed power) is given by the formula

$$NEP = 8\sqrt{2}\,\pi(2e/h)(kT)^{3/2}R_n^{1/2}\,[(3 + 2\omega^2)^{3/2}/\omega],$$

where T is the temperature; R_n is the normal state resistance of the junction; $\omega = hf/(2eI_cR_n)$ and f are the dimensionless and dimensional frequencies, respectively; and I_c is the critical current of the Josephson junction. The values of P_0 and the dynamic range depend on the frequency band ΔF and will be presented below for $\Delta F = 1$ Hz.

For a high-power signal with the frequency f, the response of the Josephson junction exhibits, in addition to the main resonance at $V_1 = hf/2e$, a resonance peculiarity at $V_2 = 2V_1$. In the spectrum restored using the Hilbert-transform spectroscopy, the latter peculiarity yields a parasitic line at a frequency of $2f$. Let us define the top limit of the dynamic range as the power at which the parasitic line intensity in the restored spectrum is one-tenth of the main line intensity. Taking into account special features of the Hilbert-transform spectroscopy, whereby the response in the restored spectrum is multiplied by the product of current and voltage [4], we infer that the ratio of amplitudes of the two resonance peculiarities in the response must be not less than 40. Approximating the behavior of resonance peculiarities in the spectra of high-power radiation by the Bessel functions J_1 and J_2 of the argument proportional to the amplitude of the current induced by the external radiation, we obtain expressions for estimation of the maximum current amplitude [6], $A_s = 0.1I_c\omega$, and the top limit of the dynamic range, $P_s = 5 \times 10^{-3}I_c^2 R_n\omega^2$. This approach takes into account special features of the Hilbert-transform spectroscopy and determines the final distortion of the result—in contrast to the estimations based on the qualitative comparison of powers of the Josephson generation and the interacting signal [6], according to which $P_s = 0.1 I_c^2 R_n$.

Figure 1 shows theoretical evaluations of the dynamic range of a frequency-selective Josephson detector as a function of the working temperature at various frequencies and junction resistances. The calculations were performed for the characteristic parameters of $YBa_2Cu_3O_{7-x}$ junctions on a bicrystal $NdGaO_3$

substrate [7] used in the experimental part of this study. As can be seen from Fig. 1, an increase in the dynamic range can be provided by decreasing the normal state resistance of the Josephson junction and by increasing the radiation frequency. The first factor is related to a decrease in the level of intrinsic noise of the Josephson junction, while the second factor is connected with a decrease in the intrinsic line width of the Josephson generation and the corresponding increase in its intensity in the region where ω is comparable with unity.

The experimental investigation of the dynamic range of the frequency-selective Josephson detector was performed in the X band, for which powerful sources of monochromatic radiation, high-precision power meters, and calibrated attenuators are available. The detector was based on bicrystal $YBa_2Cu_3O_{7-x}$ junctions [7] with the normal state resistance $R_n = 0.5–3$ Ω. The current–voltage characteristics and responses to a radiation with $f = 86$ GHz were measured in the voltage bias regime using an LNA-1618 cryogenic preamplifier with a noise level of 1.6×10^{-10} V/Hz$^{1/2}$ [8].

Figure 2 presents the typical results of measurements for one of the frequency-selective Josephson detectors studied. The absolute calibration of the power scale was performed using the theoretical value for which the response amplitude exhibits the first maximum [6]. The reference point determined by this method with an accuracy of about 25% was 6.6×10^{-8} W. The horizontal scale shows the radiation power absorbed in the junction, thus presenting the detector characteristic in the absence of coupling effects. The measurements in this series were performed with calibrated attenuators, including a device tunable within 0–60 dB and a two-level attenuator (0 and 20 dB). The experimental data were fitted in the region of normalized power 5×10^{-12} W.

As can be seen from Fig. 2, the amplitude of the frequency-selective response at $V_1 = hf/2e$ as a function of the absorbed radiation power is well approximated by a linear law at low P values, while the amplitude of the parasitic peculiarity at $V_2 = 2V_1$ is proportional to the squared power. In this experiment, the value of $NEP = (8 \pm 5) \times 10^{-15}$ W/Hz$^{1/2}$ was very close to the theoretical level (8×10^{-15} W/Hz$^{1/2}$) obtained assuming that the Josephson junction is characterized by the Johnson noise (in this case, amounting to 1.6×10^{-10} V/Hz$^{1/2}$). For comparison, previously reported experimental values of NEP were 2.7×10^{-14} V/Hz$^{1/2}$ at $T = 10$ K [9] and $10^{-13}–10^{-14}$ V/Hz$^{1/2}$ at $T = 4$ K [10].

The dynamic range determined using the same criterion as that used for theoretical estimations equals 2×10^5. It was found that the experimental values of the amplitude of the main selective peculiarity differed
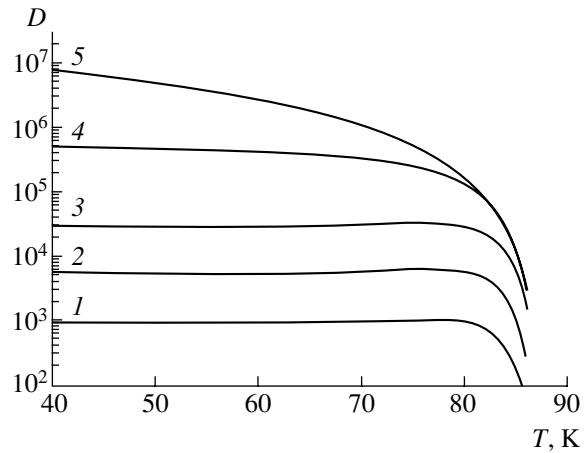

Fig. 1. Theoretical estimations of the dynamic range of a frequency-selective Josephson detector based on a bicrystal $YBa_2Cu_3O_{x-7}$ junction as a function of the working temperature, determined for the same values of the characteristic voltage $V_c = I_cR_n = 300$ μV (77 K) and $dV_c/dT \approx 25$ μV/K and various frequencies f and normal state resistances R_n: (1) $f = 100$ GHz, $R_n = 10$ Ω; (2) $f = 100$ GHz, $R_n = 3$ Ω; (3) $f = 100$ GHz, $R_n = 1$ Ω; (4) $f = 300$ GHz, $R_n = 1$ Ω; (5) $f = 1000$ GHz, $R_n = 1$ Ω.
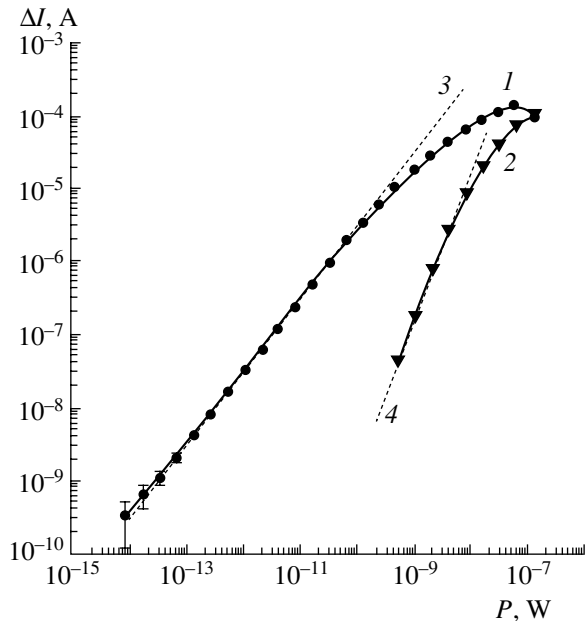

Fig. 2. Experimental plots of the amplitude of the frequency-selective response ΔI versus power P of the absorbed monochromatic radiation with $f = 86$ GHz for a Josephson junction with the parameters $R_n = 1.2$ Ω and $I_cR_n = 220$ μV at $T = 80$ K: (1) resonance peculiarity at $V_1 = hf/2e$; (2) resonance peculiarity at $V_2 = 2V_1$. Dashed lines show the asymptotic behavior of amplitudes for a small radiation power: (3) $\Delta I \propto P$ (for V_1); (4) $\Delta I \propto P^2$ (for V_2).

from the values determined using the linear law by a factor not exceeding two. The ampere–watt responsivity inside the determined dynamic range was $(3 \pm 1) \times 10^4$ A/W.

Analysis of Fig. 2 shows that the amplitude of the parasitic response at $V_2 = 2V_1$ at a power corresponding to the top limit of the dynamic range $(2 \times 10^{-9}$ W) is proportional to the squared power. Moreover, this point occurs in a transition region between the regimes of weak and strong signals related to the formation of the main peculiarity in the selective response. These circumstances explain why the theoretical estimation of the dynamic range is significantly lower than the experimental value.

According to the approximated formulas presented above, the dynamic range D at a constant value of $I_c R_n$ and a fixed frequency f should be proportional to $R_n^{3/2}$. This tendency is confirmed by the experimental value of the dynamic range (6×10^4) obtained for another $YBa_2Cu_3O_{7-x}$ Josephson junction with $R_n = 2.7 \ \Omega$.

The values of the dynamic range on the order of 10^5 obtained in this study exceed the results of our preliminarily experiments [11], where a value of 2×10^4 was obtained in the current bias regime. The new results provide for the possibility of fast measurements using the frequency-selective Josephson detector with a signal-to-noise ratio on the order of 10^2 for a frequency bandwidth $\Delta F = 10^6$ Hz.

In conclusion, we have studied the $YBa_2Cu_3O_{7-x}$ frequency-selective Josephson detector and experimentally reached a level of $NEP = 8 \times 10^{-15}$ W/Hz$^{1/2}$ (for the absorbed power) at a working temperature of 80 K and a dynamic range of 2×10^5 in the X band. According to the presented estimations, the dynamic range can be increased for Josephson junctions with lower normal state resistances and for higher radiation frequencies.

REFERENCES

1. R. Köhler, A. Tredicucci, F. Beltram, *et al.*, Nature **417**, 156 (2002).
2. G. L. Carr, M. C. Martin, W. R. McKinney, *et al.*, Nature **420**, 153 (2002).
3. C. Baker, I. S. Gregory, W. R. Tribe, *et al.*, Appl. Phys. Lett. **83**, 4113 (2003).
4. Yu. Ya. Divin, O. Yu. Polyanskiĭ, and A. Ya. Shul'man, Pis'ma Zh. Tekh. Fiz. **6**, 1056 (1980) [Sov. Tech. Phys. Lett. **6**, 454 (1980)].
5. Y. Divin, O. Volkov, V. Shirotov, *et al.*, Adv. Solid State Phys. **41**, 301 (2001).
6. K. K. Likharev and B. T. Ul'rikh, *Systems with Josephson Contact* (Mosk. Univ., Moscow, 1978).
7. Yu. Ya. Divin, I. M. Kotelyanskiĭ, and V. N. Gubankov, Radiotekh. Élektron. (Moscow) **48**, 1238 (2003).
8. N. N. Ukhansky, L. Dorrer, F. Schmidl, *et al.*, IEEE Trans. Appl. Supercond. **9**, 4416 (1999).
9. A. V. Andreev, Yu. Ya. Divin, V. N. Gubankov, *et al.*, Pis'ma Zh. Tekh. Fiz. **20** (13), 24 (1994) [Tech. Phys. Lett. **20**, 529 (1994)].
10. M. Tarasov, A. Shul'man, O. Polyansky, *et al.*, in *Proceedings of the International Conference on Millimeter and Submillimeter Waves and Applications, Denver, 1996*, pp. 89–90.
11. V. Shirotov, Y. Divin, and K. Urban, IEEE Trans. Appl. Supercond. **11**, 955 (2001).

Translated by P. Pozdeev

Conditions Preventing Thermal Breakdown in Semiconductor Devices

K. D. Tsendin and A. B. Shmelkin

Ioffe Physicotechnical Institute, Russian Academy of Sciences, St. Petersburg, 194021 Russia
e-mail: alibumbles@mail.ru
Received November 26, 2003

Abstract—We present results facilitating the prediction of the possibility of thermal breakdown in semiconductor devices and selection of the working parameters preventing such breakdowns. © *2004 MAIK "Nauka/Interperiodica".*

Introduction. Determination of the range of parameters ensuring safe operation of modern semiconductor devices is an important part of their development. Thermal breakdown is one of the universal factors of failure posing significant limitations on the possible range of working parameters [1–6]. By breakdown we imply a spontaneous avalanche growth in the temperature and current in response to a small increase in the applied voltage. As is known, devices possessing an S-shaped current–voltage characteristic feature the formation of current and temperature filaments [7] characterized by high current densities. This substantially inhomogeneous state frequently results in fracture of the material.

One of the universal mechanisms responsible for the S-shaped characteristics is the development of thermal instability. In such cases, the passage of electric current leads to heating, which, in turn, gives rise to the current. This positive feedback at a critical (threshold) applied voltage (V_{th}) leads to the phenomenon of thermal breakdown. It was demonstrated [5, 6] that thermal breakdown results in some irreversible changes in high-current electronic devices, which are caused by the passage of a high-density current.

In this study, we have determined the range of working parameters corresponding to the absence of an S-shaped region in the current–voltage characteristic, that is, preventing the development of thermal breakdown. In the calculations, we described the passage of current using the so-called drift approximation. The applicability of this approximation to the description of regimes with high current densities was justified in [8, 9].

Conditions eliminating the S-shaped current–voltage characteristic. Let us consider a semiconductor plate infinite in the (r, φ) plane, perpendicular to the z axis, and bounded by the planes $z = -L/2$ and $z = +L/2$. The plate bears metal contacts of thickness δ on both surfaces to which an external voltage V is applied (Fig. 1). We will neglect heat evolution and voltage drop in the contacts and assume a homogeneous heat exchange at the outer surfaces of contacts obeying Newton law. Owing to the symmetry, the consideration can be restricted to the half-space $z \geq 0$ with the corresponding boundary conditions.

The distribution of temperature in the semiconductor and contact is described by the following set of equations and boundary conditions [4]:

$$\kappa_s \Delta T + jF = 0, \quad 0 \leq z \leq \frac{L}{2}, \tag{1a}$$

$$\kappa_c \Delta T = 0, \quad \frac{L}{2} \leq z \leq \frac{L}{2} + \delta, \tag{1b}$$

$$\left.\frac{\partial T}{\partial z}\right|_{z=0} = 0, \tag{1c}$$

$$T|_{L/2-0} = T|_{L/2+0}, \tag{1d}$$

$$\kappa_s \left.\frac{\partial T}{\partial z}\right|_{L/2-0} = \kappa_c \left.\frac{\partial T}{\partial z}\right|_{L/2+0}, \tag{1e}$$

$$\kappa_c \frac{\partial T}{\partial z} = -\lambda(T - T_0), \quad z = \frac{L}{2} + \delta, \tag{1f}$$

$$j = \sigma F = \sigma_0 F \exp\left(-\frac{\Delta E}{kT}\right); \tag{1g}$$

where κ_c is the thermal conductivity of the semiconductor, κ_s is the thermal conductivity of the contact, j is the current density, λ is the coefficient of heat exchange with ambient medium, and T_0 is the ambient temperature.

Since the heat transfer along the semiconductor layer is absent, stationary solutions of Eqs. (1) must be independent of the polar coordinates r and φ. There-
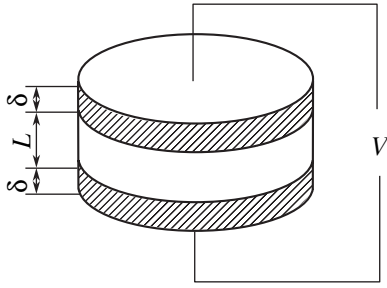
Fig. 1. Schematic diagram of the system studied (see the text for explanations).
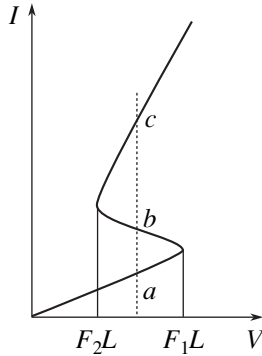

Fig. 2. Typical S-shaped current–voltage characteristic.

fore, the temperature distribution in the semiconductor layer is described by the system of equations

$$\kappa_s \frac{d^2 T}{dz^2} + jF = 0, \tag{2a}$$

$$\kappa_s \frac{\partial T}{\partial z} = -\frac{\lambda(T - T_0)}{1 + \lambda \delta / \kappa_c}, \quad z = \frac{L}{2}, \tag{2b}$$

$$j = \sigma_0 F \exp\left(-\frac{\Delta E}{kT}\right), \tag{2c}$$

$$\left. \frac{\partial T}{\partial z} \right|_{z=0} = 0. \tag{2d}$$

The voltage drop across the sample can be calculated by integrating the field:

$$V = 2 \int_0^{L/2} F(z) dz. \tag{3}$$

Explicitly solving system of equations (2), we can obtain the current–voltage characteristic under the conditions of Joule heating. However, in the context of this study, it was more interesting to determine the conditions of disappearance of the S-shaped region in this characteristic.

By analogy with Eq. (3), let us introduce the function $\tilde{v}(z)$ by integrating the field expressed using Eq. (2a) from $z = 0$ to the current coordinate z. The physical meaning of this quantity is the voltage drop in the given part of the semiconductor layer:

$$\tilde{v}(z) = -\frac{\kappa_s}{j} \frac{dT}{dz}. \tag{4}$$

Since we are not interested in determining the coordinate dependence of physical quantities, let us pass from the variables (T, z) to the dimensionless values $(t, \tilde{v})$ defined as

$$v = \tilde{v} \left[\frac{\sigma_0 k}{\kappa_s \Delta E} \right]^{1/2}, \tag{5a}$$

$$t = \frac{kT}{\Delta E}. \tag{5b}$$

In these terms, the problem of determining the stationary states of the system can be formulated as follows:

$$v_c^2 - v^2(t_c) \equiv \Phi_1 = 0, \tag{6a}$$

$$\gamma(t_c - t_0) - v_c \int_0^{v_c} \exp(-1/t) dv \equiv \Phi_2 = 0, \tag{6b}$$

$$v^2 = 2 \int_t^{t_m} \exp(1/t) dt; \tag{6c}$$

where $\gamma = \lambda L [2\kappa_s(1 + \delta\lambda/\kappa_c)]^{-1}$ is the parameter of heat removal; t_m and t_c are the dimensionless temperatures at the center and at the boundary of the semiconductor layer, respectively; and v_c is the dimensionless voltage drop across the half-thickness of the layer. Using the definition of v given by formula (5a), the voltage drop across the semiconductor layer is calculated as

$$V = 2v_c \left[\frac{\kappa_s \Delta E}{\sigma_0 k} \right]^{1/2}. \tag{7}$$

For certain sets of parameters γ, t_0, and v_c, system of equations (6) may have solutions representing three pairs of the temperatures t_c and t_m, that is, three stationary states, which corresponds to the S-shaped current–voltage characteristic (Fig. 2, points a, b, and c). The values of voltages $(v_c)_{1,2}$ corresponding to switching from the high-ohmic to low-ohmic state and vice versa are determined by the coincidence of two solutions. Mathematically, this corresponds to zero of the functional determinant,

$$\frac{\partial(\Phi_1, \Phi_2)}{\partial(t_c, t_m)} = 0. \tag{8}$$

This condition is equivalent to the equation

$$\gamma - v_c \exp(1/t_c) \int_0^{v_c} \frac{\exp(-2/t)}{t^2} dv \equiv \Phi_3 = 0, \qquad (9)$$

determining (in combination with Eqs. (6)) two sets of the variables t_c, t_m, v_c for the given external parameters t_0 and γ, which correspond to the boundaries of the region of three-valued current–voltage characteristic.

The S-shaped region disappears when the two sets determined above coincide. This condition adds one more relation between the parameters, which corresponds to zero of the functional determinant

$$\frac{\partial(\Phi_1, \Phi_2, \Phi_3)}{\partial(t_c, t_m, v_c)} = 0. \qquad (10)$$

As a result, we obtain a system of equations determining, for a preset coefficient of heat removal γ, the values of parameters t_0, t_c, t_m, and v_c corresponding to disappearance of the S-shaped region in the current voltage characteristic. Accomplishing some transformations and passing to the integration with respect to temperature t, we can write this system of equations as

$$v_c = v(t_c), \qquad (11a)$$

$$t_0 = t_c - \frac{v_c}{\gamma} \int_{t_c}^{t_m} \frac{dt}{v}, \qquad (11b)$$

$$\gamma = v_c \exp(1/t_c) \int_{t_c}^{t_m} \frac{\exp(-1/t)}{v t^2} dt, \qquad (11c)$$

$$\int_{t_c}^{t_m} \left\{ \exp(-1/t) \frac{1-t}{t^2} - \exp(-1/t_c) \frac{1}{t_c^2} \right\} \frac{\exp(-1/t)}{v t^2} dt = 0, \qquad (11d)$$

$$v = \left[2 \int_t^{t_m} \exp(1/t') dt' \right]^{1/2}. \qquad (11e)$$

System (11) was solved numerically, and the results of calculations are presented in Fig. 3. Note that, in the region of small heat transfer coefficients, our results (see the inset in Fig. 3) significantly refine the published data [10]. The results for high values of γ are obtained for the first time.

As can be seen, there are two possible ways to eliminate the S-shaped region in the current–voltage characteristic: (i) by increasing the heat removal so as to suppress the Joule heating and (ii) by increasing the ambient temperature so as to decrease the temperature dependence of the conductivity. It should be noted that the problem was solved in the approximation of electroneutrality, that is, assuming that the space charge related to inhomogeneity of the electric field is negligi-
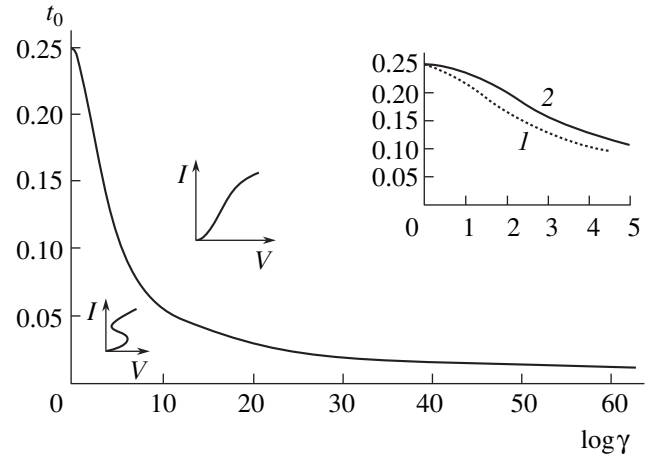

Fig. 3. The plot of conditions corresponding to the existence of an S-shaped region in the current–voltage characteristic. The inset shows a difference between (*1*) published data [10] and (*2*) our results for small γ.

bly small. However, an increase in the coefficient of heat removal leads to a growth in inhomogeneity of both temperature and field, so that this assumption may fail to be valid.

Estimates based on the obtained results. Using an analytical solution of the above problem in the case of a homogeneous temperature, it is possible to obtain expressions for the temperature and field of the direct and reverse transitions. Based on these relations, we made some estimates illustrating the order of characteristic values. The values of the conductivity activation energy, semiconductor melting temperature (T_3), and the direct (T_1) and reverse (T_2) switching are presented in the table.

As can be seen from data in the table, the breakdown of intrinsic semiconductors is irreversible and difficult to predict. Indeed, the temperature increment to breakdown amounts to 15–30 K, and the characteristic tem-

Characteristic temperatures of silicon and germanium*

Semiconductor	ΔE, eV	$\Delta E/4k$, K	T_1, K	T_2, K	T_3, K
Si	0.56	1620	315	6180	1690
Ge	0.33	960	328	3500	1210
Si (As-doped, $T_0 = 150$ K)	0.054	157	250	380	–
Si (In)	0.155	450	380	1420	–
Ge (Te)	0.11	319	480	790	–
Ge (Be, $T_0 = 200$ K)	0.07	203	357	455	–

Note: * The values of constants for the calculations were taken from [11]; the ambient temperature was taken equal to 300 K.

perature of the low-ohmic state (T_2) is higher than the melting temperature. On the other hand, the "impurity" breakdown does not necessarily lead to degradation of the sample (this makes possible the creation of thin-film switching devices).

Let us evaluate the ratio of field strengths necessary for the breakdown of like films made of pure (sample A) and tellurium-doped (sample B) germanium:

$$\frac{F_A}{F_B} \propto \sqrt{\frac{\Delta E_B}{\Delta E_A}} \exp\left(\frac{\Delta E_A - \Delta E_B}{2kT_0}\right) \approx 40. \qquad (12)$$

This result shows that the "impurity" breakdown takes place much "earlier" than that in the intrinsic semiconductor.

Now, let us consider the case of indium-doped silicon with silver contacts and find the conditions of disappearance of the S-shaped region in the current–voltage characteristic of this system. Since $t_0 \approx 0.17$ ($T_0 = 300$ K), the necessary value of the coefficient of heat removal is $\gamma \approx 500$ (Fig. 3). Assuming the ideal heat removal from contacts ($\lambda = \infty$), we obtain the condition of absence of the S-shaped region: $L/\delta \approx 300$. As expected, the breakdown is eliminated for a sufficiently thick film. In the case of a tellurium-doped germanium film ($\gamma \approx 10$), the S-shaped region is eliminated if the semiconductor layer thickness is three times that of the contact layer.

Conclusions. We have determined the region of parameters corresponding to the S-shaped current–voltage characteristic of a system possessing conductivity of the activation type in the range of temperatures from 0 to $\Delta E/4k$ and arbitrary conditions of heat removal.

Using the obtained results, it is possible to predict the conditions favoring breakdown in semiconductors and insulators in strong electric fields.

In the region of small values of the coefficient of heat removal γ, our results qualitatively agree with the published data. For large γ values, the region of parameters corresponding to the S-shaped current-voltage characteristic was determined for the first time.

REFERENCES

1. S. M. Bragin, A. F. Val'ter, and N. N. Semenov, *Theory and Applications of the Breakdown of Insulators* (Gosizdat, Moscow, 1929), p. 383.

2. Zh. I. Alferov and A. I. Uvarov, Élektrichestvo, No. 5, 53 (1964).

3. A. I. Uvarov, *Some Problems on the Development, Investigation and Application of Semiconductor Devices* (Nauka, Leningrad, 1965).

4. V. A. Fok, Tr. Leningr. Fiz.-Tekh. Inst. **5**, 52 (1928).

5. A. V. Gorbatyuk, I. A. Liniĭchuk, and A. V. Svirin, Pis'ma Zh. Tekh. Fiz. **15** (6), 42 (1989) [Sov. Tech. Phys. Lett. **15**, 224 (1989)].

6. A. V. Gorbatyuk and P. B. Rodin, Pis'ma Zh. Tekh. Fiz. **16** (13), 89 (1990) [Sov. Tech. Phys. Lett. **16**, 519 (1990)].

7. B. K. Ridley, Proc. Phys. Soc. London **82**, 954 (1963).

8. A. V. Gorbatyuk and I. E. Panaotti, Pis'ma Zh. Tekh. Fiz. **29** (9), 35 (2003) [Tech. Phys. Lett. **29**, 370 (2003)].

9. T. T. Mnatsakanov, I. L. Rostovtsev, and N. I. Filatov, Solid-State Electron. **30**, 579 (1987).

10. É. A. Lebedev and K. D. Tsendin, *Electronic Phenomena in Chalcogenide Glassy Semiconductors*, Ed. by K. D. Tsendin (Nauka, St. Petersburg, 1996).

11. *Handbook of Physical Quantities,* Ed. by I. S. Grigoriev and E. Z. Meilikhov (Énergoatomizdat, Moscow, 1991; CRC Press, Boca Raton, 1997).

Translated by P. Pozdeev